SMIP23

SMIP23 SEMINAR ON
UTILIZATION OF STRONG-MOTION DATA

October 19, 2023

PROCEEDINGS

Sponsored by

California Strong Motion Instrumentation Program
California Geological Survey
California Department of Conservation

Co-Sponsors

California Seismic Safety Commission
California Governor's Office of Emergency Services
California Department of Health Care Access and Information
California Department of Transportation

California
Department of
Conservation
California Geological Survey

The California Strong Motion Instrumentation Program (CSMIP), a program within the California Geological Survey (CGS) of the California Department of Conservation, records the strong shaking of the ground and structures during earthquakes for analysis and utilization by the engineering and seismology communities, through a statewide network of strong motion instruments (www.conservation.ca.gov/CGS/smip). CSMIP is advised by the Strong Motion Instrumentation Advisory Committee (SMIAC), a committee of the California Seismic Safety Commission. Major program funding is provided by an assessment on construction costs for building permits issued by cities and counties in California, with additional funding from the California Governor's Office of Emergency Services (Cal OES), the California Department of Health Care Access and Information (HCAI) and the California Department of Transportation (Caltrans).

In July 2001, Cal OES began funding for the California Integrated Seismic Network (CISN), a newly formed consortium of institutions engaged in statewide earthquake monitoring that grew out of TriNet, funded by FEMA, and included CGS, USGS, Caltech and UC Berkeley. The goals of CISN are to record and rapidly communicate ground shaking information in California, and to analyze the data for the improvement of seismic codes and standards (www.cisn.org). CISN produces ShakeMaps of ground shaking, based on shaking recorded by stations in the network, within minutes following an earthquake. The ShakeMap identifies areas of greatest ground shaking for use by Cal OES and other emergency response agencies in the event of a damaging earthquake.

The Center for Engineering Strong Motion Data (CESMD) is operated by the CSMIP in cooperation with the National Strong-Motion Project (NSMP), a part of the Advanced National Seismic System (ANSS) of the U.S. Geological Survey (USGS). The CESMD builds on and incorporates the CISN Engineering Data Center and will continue to serve the California region while expanding to serve other ANSS regions. The Data Center provides strong-motion data rapidly after a significant earthquake in the United States. Users also have direct access to data from previous earthquakes and detailed information about the instrumented structures and sites. The CESMD also provides access to the U.S. and international strong ground motion records through its Virtual Data Center (VDC). The Data Center is co-hosted by CGS and USGS at www.strongmotioncenter.org

DISCLAIMER

Neither the sponsoring nor supporting agencies assume responsibility for the accuracy of the information presented in this report or for the opinions expressed herein. The material presented in this publication should not be used or relied upon for any specific application without competent examination and verification of its accuracy, suitability, and applicability by qualified professionals. Users of information from this publication assume all liability arising from such use.

SMIP23

SMIP23 SEMINAR ON
UTILIZATION OF STRONG-MOTION DATA

October 19, 2023

<u>PROCEEDINGS</u>

Edited by

Daniel Swensen

Sponsored by

California Strong Motion Instrumentation Program
California Geological Survey
California Department of Conservation

Co-Sponsors

California Seismic Safety Commission
California Governor's Office of Emergency Services
California Department of Health Care Access and Information
California Department of Transportation

PREFACE

The California Strong Motion Instrumentation Program (CSMIP) in the California Geological Survey of the California Department of Conservation established a Data Interpretation Project in 1989. Each year CSMIP funds several data interpretation contracts for the analysis and utilization of strong-motion data. The primary objectives of the Data Interpretation Project are to further the understanding of strong ground shaking and the response of structures, and to increase the utilization of strong-motion data in improving post-earthquake response, seismic code provisions and design practices.

As part of the Data Interpretation Project, CSMIP holds annual seminars to transfer recent research findings on strong-motion data to practicing seismic design professionals, earth scientists and post-earthquake response personnel. The purpose of the annual seminar is to provide information that will be useful immediately in seismic design practice and post-earthquake response, and in the longer term, useful in the improvement of seismic design codes and practices. Proceedings and individual papers for each of the previous annual seminars are available at http://www.conservation.ca.gov/cgs/smip/seminar in PDF format. Due to State budget constraints, CSMIP did not hold an annual seminar in 2010 or 2011. The SMIP23 Seminar is the thirty-second in this series of annual seminars.

The SMIP23 Seminar is divided into two sessions in the morning and two sessions in the afternoon. There are seven presentations in total; six are on the results of CSMIP-funded projects. The sessions in the morning include four presentations. The first session will focus on structural response topics. Professor Mosalam of UC Berkeley will present on the use of neural networks in structural response prediction. He will be followed by a presentation from Professor Bernal of Northeastern University on inherent damping of structures during nonlinear seismic response. The second session will include presentations on both structural and lifeline response topics. Professor Tsampras of UC San Diego will present on diaphragm seismic design provisions and higher-mode responses of buildings. He will be followed by a presentation from Professor Athanasopoulos-Zekkos of UC Berkeley on dynamic response parameters of earth dams.

The sessions in the afternoon include three presentations. The third session will focus on ground response topics. Professor Olsen of San Diego State University will present on the near-surface seismic structure of the SCEC Community Velocity Model. He will be followed by a presentation from Professor Stewart of UC Los Angeles on the useability of ground motions recorded by the Community Seismic Network. The last session will focus on the 2023 Turkey earthquake sequence. Professor Akciz of Cal State Fullerton, Professor Moss of Cal Poly San Luis Obispo, Dr. Hortacsu of the Applied Technology Council and Dr. Buckreis of UC Los Angeles will present on the seismological and faulting, geotechnical engineering, structural engineering, and strong motion data aspects of the earthquake sequence, respectively. Individual papers and the proceedings are available for download by the SMIP23 participants at the provided link and will be available at the CSMIP website in the future.

Daniel Swensen
CSMIP Data Interpretation Project Manager

Appreciation to Members of the
Strong Motion Instrumentation Advisory Committee

Main Committee
Farzad Naeim, Chair, Farzad Naeim, Inc.
Norman Abrahamson, UC Berkeley
Bruce Clark, Leighton & Associates
Martin Eskijian, California State Lands Commission
David Gutierrez, GEI Consultants
Marshall Lew, Wood
Bret Lizundia, Rutherford + Chekene
Carlos Ventura, University of British Columbia
Chris Tokas, California Department of Health Care Access and Information
Chris Traina, California Department of Transportation
Jia Wang-Connelly (ex-officio), Seismic Safety Commission

Ground Response Subcommittee
Marshall Lew, Chair, Wood
Zia Zafir, Kleinfelder
Martin Hudson, Turner

Buildings Subcommittee
Bret Lizundia, Chair, Rutherford + Chekene
Lucie Fougner, Degenkolb Engineers
Ifa Kashefi, City of Los Angeles (retired)
Michelle Yu, City of San Francisco
Eduardo Miranda, Stanford University
Roy Lobo, California Department of Health Care Access and Information
Chia-Ming Uang, UC San Diego

Lifelines Subcommittee
Martin Eskijian, Chair, California State Lands Commission
David Gutierrez, GEI Consultants
Faiz Makdisi, Gannett Fleming
Chris Traina, California Department of Transportation

Data Utilization Subcommittee
Representatives from each Subcommittee

TABLE OF CONTENTS

<div style="border: 2px solid black; text-align: center;">

SMIP23 SEMINAR ON
UTILIZATION OF STRONG-MOTION DATA

</div>

October 19, 2023

FINAL PROGRAM

9:15 am　**WELCOMING REMARKS**
　　　　Farzad Naeim, Chair, Strong Motion Instrumentation Advisory Committee (SMIAC)
　　　　Jeremy Lancaster, State Geologist and Director, California Geological Survey

9:25 am　**INTRODUCTION**
　　　　Hamid Haddadi, Program Manager, California Strong Motion Instrumentation Program
　　　　Dan Swensen, Senior Civil Engineer, California Strong Motion Instrumentation Program

---

Session I

Moderator:　*Bret Lizundia*, Rutherford + Chekene and SMIAC

9:30 am　**Structural Response Prediction using Deep Neural Networks**
　　　　Issac Kwok-Tai Pang, Selim Gunay and *Khalid M. Mosalam*, UC Berkeley

10:00 am　**Inherent Damping During Nonlinear Seismic Response**
　　　　Dennis Bernal, Northeastern University

10:30 am　**Break**

Session II

Moderator:　*Martin Eskijian*, California State Lands Commission and SMIAC

11:00 am　**Validation of Seismic Design Provisions for Diaphragms and Assessment of Higher-Mode Responses on Earthquake-Resistant Buildings**
　　　　C. Franco Mayorga and *Georgios Tsampras*, UC San Diego

11:30 am　**Using CSMIP Data to Derive Reliable Values of Dynamic Response Parameters for Earth Dams in California**
　　　　Makbule Ilgac and *Adda Athanasopoulos-Zekkos*, UC Berkeley

12:00 pm　**Lunch Break**

Session III

Moderator: *Zia Zafir*, Kleinfelder and SMIAC

1:00 pm **Calibration of the Near-surface Seismic Structure in the SCEC Community Velocity Model Version S**
Kim Olsen and Te-Yang Yeh, San Diego State University

1:30 pm **Usability of Ground Motions Recorded by Community Seismic Network**
Shako Ahmed, Tristan Buckreis, Yousef Bozorgnia and *Jonathan P. Stewart*, UC Los Angeles

Rashid Shams and Chukwuebuka Nweke, University of Southern California

Monica Kohler, Caltech

2:00 pm **Break**

Session IV

Moderator: *Eduardo Miranda*, Stanford and SMIAC

2:30 pm **2023 Turkey Earthquake Sequence**
Seismology and Faulting: *Sinan Akciz*, Cal State Fullerton

Geotechnical Engineering: *Robb Moss*, Cal Poly San Luis Obispo

Structural Engineering: *Ayse Hortacsu*, Applied Technology Council

Strong Motion Data: *Tristan Buckreis*, UC Los Angeles

3:30 pm **Adjourn**

STRUCTURAL RESPONSE PREDICTION USING DEEP NEURAL NETWORKS

Selim Günay[1], Issac Kwok-Tai Pang[2], and Khalid M. Mosalam[3]

University of California, Berkeley

Abstract

This paper presents a methodology to obtain the time history of the structural response using the Temporal Convolutional Network, a deep learning method. The presented methodology, in conjunction with sensor data from instrumented buildings, facilitates the prediction of the response in future earthquakes without the need for a structural analysis model. In this way, a computationally effective complement, or even alternative, to standard nonlinear time history analysis is possible. The applications of the developed method for different cases, including available number of records, buildings with higher mode effects, and linear and nonlinear response, are explored using accelerometer data from buildings instrumented by the California Strong Motion Instrumentation Program. Fundamental concepts of structural response and structural dynamics are used to guide the development of the training datasets and to explain the predictions. Furthermore, interpretation of the results is presented using earthquake engineering concepts.

Introduction

There are three fundamental methods used to determine the dynamic response of structures, namely, (a) installing sensors on real structures, (b) testing physical models of the structures in the laboratory, and (c) analyzing the numerical models of structures using computational methods. Among these methods, the first is the most realistic as it is based on the measurements from the real structures. However, there is scarcity of instrumented real structures. Laboratory testing also provides realistic information when the tests are conducted on accurate physical models of the entire structure or its components. Drawbacks of this method are time, cost, and laboratory space constraints. Based on the accuracy of the employed mathematical assumptions, the third method is relatively less realistic compared to the first two. However, it is the most common and convenient approach because of the availability of the many computational platforms to conduct the analysis.

This paper aims at developing a methodology to obtain the time history of the structural response using a deep learning approach, namely the Temporal Convolutional Network (TCN). When the developed methodology is adopted in conjunction with sensor data from instrumented buildings, it can facilitate the prediction of the response in future earthquakes without the need

---

[1]Researcher, selimgunay@berkeley.edu.

[2]PhD Student, issac.pang@berkeley.edu.

[3]Taisei Professor of Civil Engineering & PEER Director, corresponding author, mosalam@berkeley.edu.

for a structural analysis model. In this way, the proposed methodology can complement or even provide a computationally effective alternative to nonlinear time history analysis. The applications of the developed method are presented to assess the minimum number of records for accurate training, and to study buildings with linear and nonlinear response and higher mode effects. In all applications, accelerometer data from buildings instrumented by the California Strong Motion Instrumentation Program (CSMIP) are used.

There has been a limited number of studies in the literature to predict the structural response using deep learning. Some of these studies focused on predicting only the peak response (Zhong et al., 2023). Although the peak response is important in design, assessment, and Performance-Based Earthquake Engineering (PBEE), the entire response history provides a more complete description of the structural behavior. One particular use of the entire response history is detection of the existence, severity, and location of damage in Structural Health Monitoring (SHM), where the peak response is generally insufficient for this purpose (Muin and Mosalam, 2017, 2018; Park and Ang, 1985, Park et al., 1985). Considering the importance of predicting the entire response history, there has been a few studies focused on predicting the entire response using machine learning (e.g., Chen et al., 2023; Zhang et al., 2019; Kundu and Chakraborty, 2020; Li and Spence, 2020). These studies focused on either a structural component or a single instrumented building and have not provided detailed physical explanations of the data-driven predictions. This paper applies the developed methodology to several instrumented buildings with different characteristics and attempts to explain the results using concepts of structural dynamics. Furthermore, interpretation of the results is presented using earthquake engineering concepts.

Following this introduction, the paper provides a brief overview of the adopted TCN, followed by an explanation of the metrics used to assess the accuracy of the predictions. Subsequently, the paper discusses the linear response predictions of instrumented mid-rise buildings governed by the fundamental mode of response and a tall building with higher mode effects. This is followed by investigating the nonlinear response predictions. Finally, conclusions and future studies are discussed.

Temporal Convolutional Network

The TCN was proposed by Lea et al. (2017) and is a powerful and innovative deep learning architecture designed for processing sequential data, particularly for time-series analysis and natural language processing tasks. TCNs are built upon the Convolutional Neural Networks (CNNs) but they can be adapted to model temporal dependencies in sequential data, making them suitable for tasks which require understanding patterns and trends over time. TCNs employ a stack of one-dimensional convolutional layers to efficiently learn dependencies across different time steps. This design allows TCNs to utilize parallel computing, which makes them efficient and fast to train. TCNs have gained popularity due to their ability to capture long-range dependencies in sequential data without suffering from the vanishing gradient problem often encountered by other deep learning methods, like Recurrent Neural Networks (RNNs). They have been successfully applied in various domains, such as natural language processing, speech recognition, and sensor data analysis.

Accuracy Evaluation Metrics

The metrics used for evaluating the accuracy of the predictions of the adopted TCN are: 1) correlation coefficient, 2) probability distribution of the errors, 3) errors in the peak response, 4) frequency contents of the response (obtained from the response spectrum or the Fourier amplitude spectrum), and 5) Cumulative Absolute Velocity (CAV). The first two metrics are statistical parameters, where the correlation coefficient and the error at time step i are defined with Equations 1 and 2, respectively. As discussed earlier, the peak response is commonly used in design, assessment, and PBEE. Therefore, it needs to be predicted accurately. The third metric focuses on the accuracy of the prediction of the peak response (Equation 3). Comparisons of the frequency contents of the true and predicted responses provide fundamental insights into how the predictions can be improved, e.g., if the dominant frequency in the response is not captured properly, this indicates that the natural frequencies of the building are not "learned" properly by the TCN providing guidance on how to improve the predictions, as discussed later. Finally, CAV (Equation 4) is shown to be a reliable indicator of damage (Muin and Mosalam, 2017), which needs to be predicted accurately for any consequent detection of damage from the predicted response using SHM.

$$\rho = \frac{\sum_{i=1}^{i=n}\left(y_i^{real} - \bar{y}^{real}\right)\left(y_i^{predicted} - \bar{y}^{predicted}\right)}{\sqrt{\sum_{i=1}^{i=n}(y_i^{real} - \bar{y}^{real})^2\left(y_i^{predicted} - \bar{y}^{predicted}\right)^2}} \tag{1}$$

$$err_i = \frac{y_i^{real} - y_i^{predicted}}{\max\left(y_i^{real}\right)} \tag{2}$$

$$err\_peak_i = \frac{\max\left(y_i^{predicted}\right) - \max\left(y_i^{real}\right)}{\max\left(y_i^{real}\right)} \tag{3}$$

where, y_i^{real} and $y_i^{predicted}$ are respectively the true and predicted responses at time step i, $\bar{y}^{real}$ and $\bar{y}^{predicted}$ are the mean values of the true and predicted responses, respectively, n is the number of time steps, and max indicates the peak response.

$$CAV(T) = \int_{t=0}^{t=T} |\ddot{u}(t)| dt \tag{4}$$

where T is the current time at which CAV is computed (typically it is the entire duration of the time series) and $\ddot{u}(t)$ is the response acceleration at a given time t.

Linear Elastic Response Prediction of Low and Mid-Rise Buildings

Single Degree of Freedom (SDOF) Numerical Model

For verification of the developed TCN model and its implementation, the displacement and acceleration responses of a linear elastic SDOF system are predicted and compared with the actual computed results. For this purpose, a SDOF system is considered with a period of 0.41 sec and damping ratio of 2.35% and is trained using 11 motions and tested using 7 motions. The

chosen period and damping ratio are those identified for the San Bernardino 6-story hotel in the NS direction, which is discussed next. The motions used for training and testing are the recorded ground and response accelerations of the same hotel building. Using the metrics discussed earlier, both displacement and acceleration predictions are very accurate with a correlation coefficient of 99.99% over the 7 tested motions, verifying the implementation of the TCN method. The predicted acceleration and displacement time histories are compared with the computed ones (referred to as real) for one of the test motions (Fontana Earthquake of 25 July 2015) in Figure 1, along with the comparison of the frequency contents, showing a very close match.
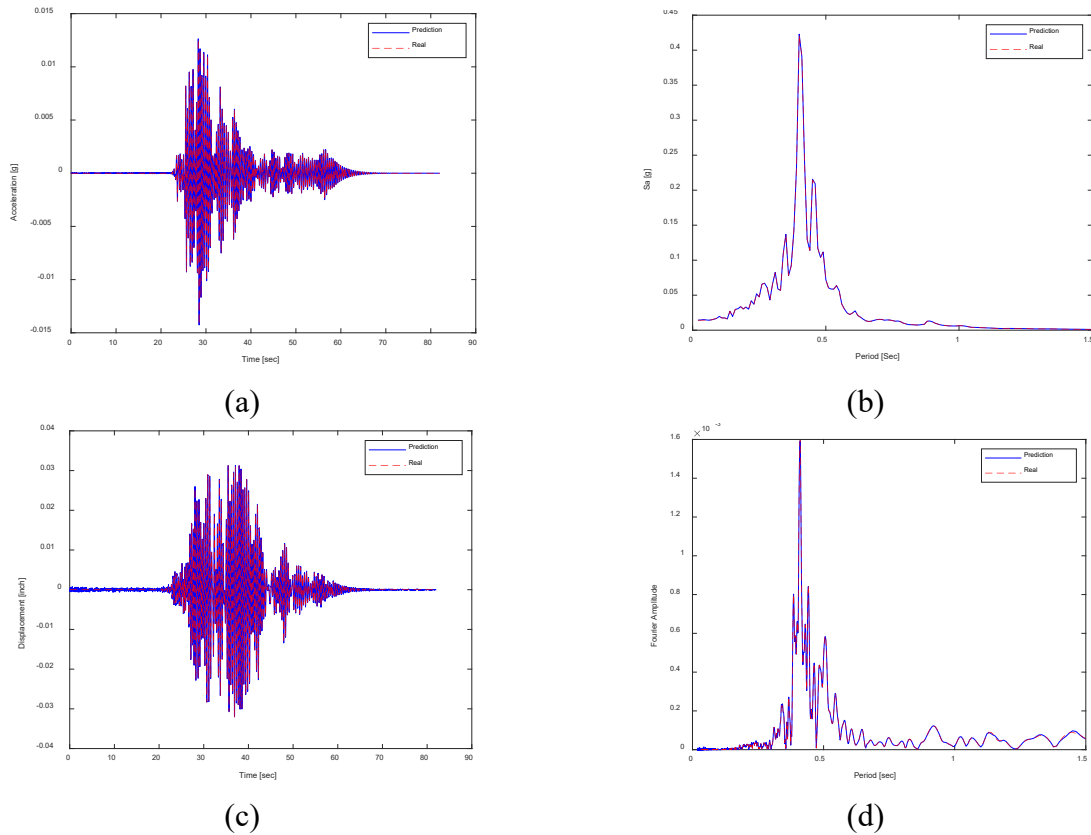

(a)

(b)

(c)

(d)

Figure 1. Comparison of predicted and computed (a) acceleration time history, (b) frequency content from acceleration, (c) displacement time history, and (d) frequency content from displacement, for the linear elastic SDOF system in one of the test motions (Fontana Earthquake of 25 July 2015).

The response of an elastic SDOF system subjected to ground motions depends only on: (a) the natural period of the SDOF system, (b) the damping ratio of the SDOF system, and (c) the applied ground motion, which are considered as the three features to be learned by the TCN for subsequent predictions (Table 1). The highly accurate predictions of the SDOF system indicate that the TCN model is successful in learning the period and the damping ratio (Features 1 and 2, respectively, in Table 1) and the training model has enough variety of the ground motions for the

model to learn the response of this system when subjected to different excitations (Feature 3 in Table 1).

Table 1. Features that characterize the earthquake response of different structural systems.

System	Feature 1	Feature 2	Feature 3
Linear Elastic SDOF	Natural period	Damping ratio	Ground motion
Low and Mid-rise Buildings Linear Elastic	First mode period	Varying first mode damping ratios	
Tall Buildings Linear Elastic	Multiple modes periods	Multiple modes damping ratios	
Low and Mid-rise Buildings Nonlinear	First mode period elongation	Varying first mode damping ratios	

6-Story Reinforced Concrete (RC) Hotel Building in San Bernardino

After this fundamental step of demonstrating that the implemented TCN model is successful in predicting the response history of an elastic SDOF system numerical model, predictions are performed for the linear elastic response of two instrumented CSMIP buildings (Figure 2). The first is a 6-story RC Shear Wall (RCSW) hotel building in San Bernardino, California, designed in 1970. This building is instrumented with 9 accelerometers, three on each of the 1st, 3rd, and 6th (roof) floors, and has recorded multiple seismic events from 1987 to 2018. The EW and NS direction responses of this building are studied in this section for the linear response and in a later section for the nonlinear response. In the EW direction, Channel 1 on the 1st floor is used as input, and Channels 4 and 7, on the 3rd floor and roof, respectively, are used as outputs. It is noted that the 1st floor boundary conditions are fixed. Therefore, Channel 1 directly represents the ground motion input to the structure. There are a total of 26 events recorded by this station, where records 1 to 11 and records 12 to 18 are respectively used for training and testing, Table 2, which lists the Peak Ground Acceleration (PGA) and Peak Floor Acceleration (PFA) for the EW and NS directions. As shown in Figure 3, the motions used in the training set cover the entire range of shaking levels recorded on this building. It is possible to use another Intensity Measure (IM) to define the horizontal axis of this figure, however the PGA is used for simplicity as the objective is not to use the IM for quantitative damage detection or other purposes, but it is rather to characterize the training and testing set motions on a plot with experienced shaking levels. As discussed later, 11 motions were sufficient for predicting accurate results for the linear elastic response in the EW direction, and more motions were utilized for capturing the nonlinear response in the NS direction.
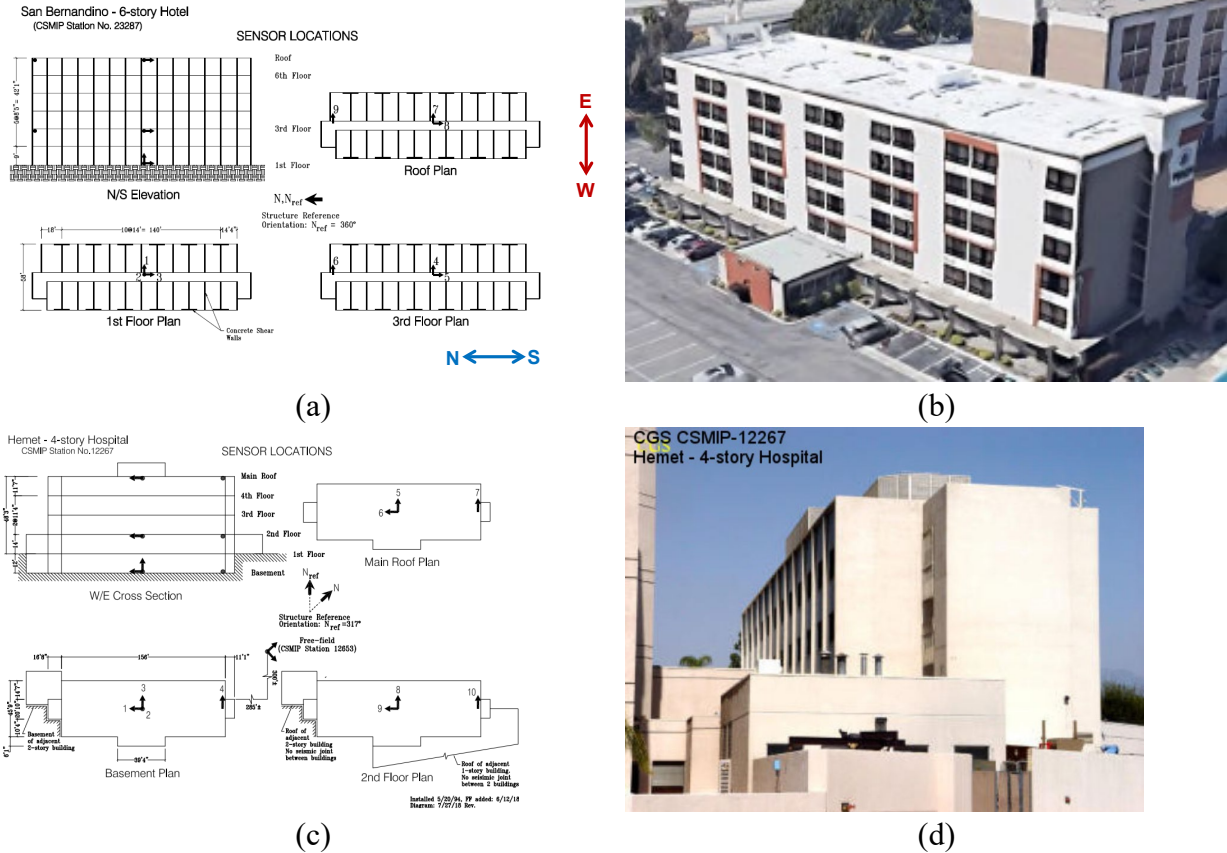
(a)   (b)

(c)   (d)

Figure 2. Sensor locations and photographs of (a, b) 6-story building at San Bernardino and (c, d) 4-story building in Hemet.
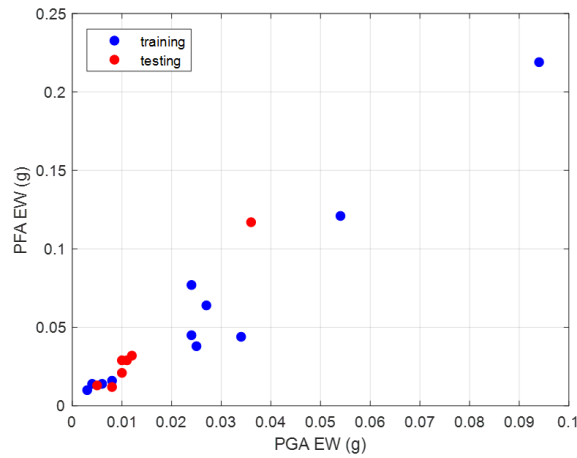

Figure 3. The training and testing sets used for the San Bernardino 6-story building EW direction.

For the input-output pairs, two cases are used: (i) the unprocessed accelerations, and (ii) CSMIP processed accelerations that use bandpass filters and baseline correction. Accuracy of the training and testing sets for both cases, computed using the correlation coefficient (Equation 1), are reported in Table 3. The training accuracy of 0.97 for both the unprocessed and processed

data shows that there are no major outliers in the set. From the testing set accuracies, it is observed that training of both unprocessed and processed data result in successful predictions. However, using the unprocessed data results in more accurate predictions, although the difference is small. This observation is not specific to this building and has been observed for the other two studied instrumented buildings. The explanation of this observation is that the processed output is not necessarily the direct result of the processed ground motion input. Therefore, the relationship between the input and output deviates slightly from true physics when processed data is used for input and output. Considering the higher accuracy using the unprocessed data, the rest of the paper reports the results that use unprocessed data.

Table 2. San Bernadino 6-story hotel training and testing records.

#	Earthquake Name	PGA NS (g)	PFA NS (g)	PGA EW (g)	PFA EW (g)
1	Borrego Springs Area Earthquake of 07 Jul 2010	0.053	0.2	0.024	0.045
2	Devore Earthquake of 29 Dec 2015	0.049	0.106	0.054	0.121
3	Fontana Earthquake of 15 Jan 2014	0.04	0.089	0.034	0.044
4	Inglewood Area Earthquake of 17 May 2009	0.008	0.027	0.008	0.016
5	Ocotillo Area Earthquake of 14 Jun 2010	0.006	0.022	0.006	0.014
6	San Bernardino Earthquake of 08 Jan 2009	0.058	0.168	0.094	0.219
7	Beaumont Earthquake of 14 Sep 2011	0.02	0.041	0.027	0.064
8	La Habra Earthquake of 28 Mar 2014	0.021	0.033	0.024	0.077
9	Loma Linda Earthquake of 13 Mar 2017	0.022	0.05	0.025	0.038
10	Ontario Earthquake of 20 Dec 2011	0.004	0.009	0.004	0.014
11	Yorba Linda Earthquake of 07 Aug 2012	0.009	0.016	0.003	0.01
12	Beaumont Area Earthquake of 16 Jan 2010	0.006	0.013	0.005	0.013
13	Big Bear Lake Earthquake of 05 Jul 2014	0.01	0.03	0.011	0.029
14	Fontana Earthquake of 25 Jul 2015	0.011	0.025	0.01	0.021
15	Loma Linda Earthquake of 08 Oct 2016	0.01	0.017	0.008	0.012
16	Devore Earthquake of 28 Apr 2012	0.017	0.043	0.01	0.029
17	Loma Linda Earthquake of 04 Mar 2013	0.007	0.017	0.012	0.032
18	Chino Hills Earthquake of 29 July 2008	0.05	0.113	0.036	0.117

Table 3. Accuracy of the San Bernardino 6-story building acceleration predictions in the E-W direction.

Data	Correlation Coefficient	
	Training Set	Testing Set
Unprocessed	0.97	0.91
Processed	0.97	0.88

The high accuracy indicated by the correlation coefficient is also supported by the narrow probability distribution of the normalized error (Equation 2) with the mean close to zero (Figure 4). The predicted acceleration time histories at the 3rd and 6th (roof) floors are compared with the recorded time histories for one of the test motions (Fontana Earthquake of 25 July 2015) in Figure 5, along with the comparison of the frequency contents, showing a close match at both floors in the time and frequency domains. Comparison of peak values indicated an error of -4.80% and -4.94% according to Equation 3.
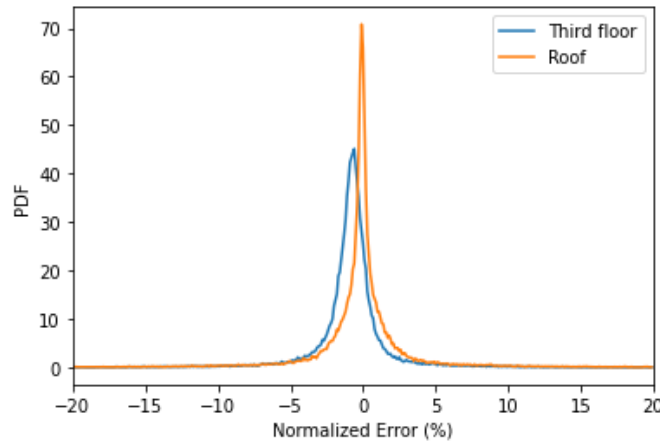

Figure 4. Narrow probability distributions of the normalized prediction errors in the EW direction at the 3rd and 6th (roof) floors of the San Bernardino 6-story building.

It is inevitable in real instrumented buildings to prevent the peak prediction errors completely. Therefore, the errors in the peak predictions can be interpreted from the following two perspectives related to their use in earthquake engineering:

(1) Epistemic uncertainty is due to errors in mathematical modeling, where the error due to the TCN model is an example. Therefore, in design and assessment of buildings, the results of a single ground motion are not used. ASCE7-22 (2022) requires 11 motions for nonlinear dynamic analysis and a varying number of ground motions (e.g., 20) is essential for probabilistic PBEE (Günay and Mosalam, 2013). Accordingly, in addition to the individual motion results, comparison of the probability distributions of the true and predicted responses are helpful for evaluating the accuracy of the predictions. The PFA at the 3rd and 6th floors are assumed to follow a lognormal probability distribution, which are computed using the peak values of all test motions and plotted for the true and predicted accelerations in Figure 6. It is observed that the resulting probability distributions are close to each other at both floors, illustrating the accuracy of the predictions from this perspective.

(2) The relationship between estimated peak response and damage is obtained using fragility functions. Another way of evaluating the peak prediction is the comparison of damage probability corresponding to the predicted and real results. As an example, the fragility function of a cooling tower, assumed to be located at the roof of the San Bernardino 6-story hotel building, is shown in Figure 7. The damage state that this fragility function represents is that the cooling tower and attached piping are damaged. It is defined by a mean of 0.5g and a

dispersion of 0.4 (FEMA-P58, 2018a, b). The probability of exceedance (POE) of this damage state, using the predicted and true 6th floor PFA for the Chino Hills Earthquake of 07 Aug 2012 (Figure 5), are 5.9% and 6.8%, respectively. In addition to the damage prediction for this single event, the POE in the fragility function [$(POE(DM|PFA)$, Figure 7] can be integrated with the probability of true and predicted PFA [$p(PFA)$, Figure 6b] using the total probability theorem, resulting in the POE of the damage state considering all the test motions [$POE(DM)$, Equation 5]. It is noted that the probability of the damage state is equal to POE here because only one damage state is used herein. Therefore, the resulting probability of damage to a cooling tower located at the roof of the 6-story San Bernardino hotel building, considering all 7 test motions, is 0.33% and 0.30%, respectively, when the true and predicted peaks are used.

$$POE(DM) = POE(DM|PFA)p(PFA) \tag{5}$$

The above discussion presented the results from a probabilistic PBEE perspective based on peak predictions. As discussed earlier, the entire response history is important to characterize the full structural behavior, and in this context the *CAV* (Equation 4) is a parameter that is closely related to damage and is a suitable metric to evaluate the predictions. Figure 8 shows the *CAV* of the predicted and true accelerations for one of the test motions (Chino Hills Earthquake of 07 Aug 2012). From this figure, similar to the acceleration time histories, it is observed that the *CAV* time histories of the predicted and true accelerations are very close to each other, showing that the predicted response can be used reliably to identify damage.
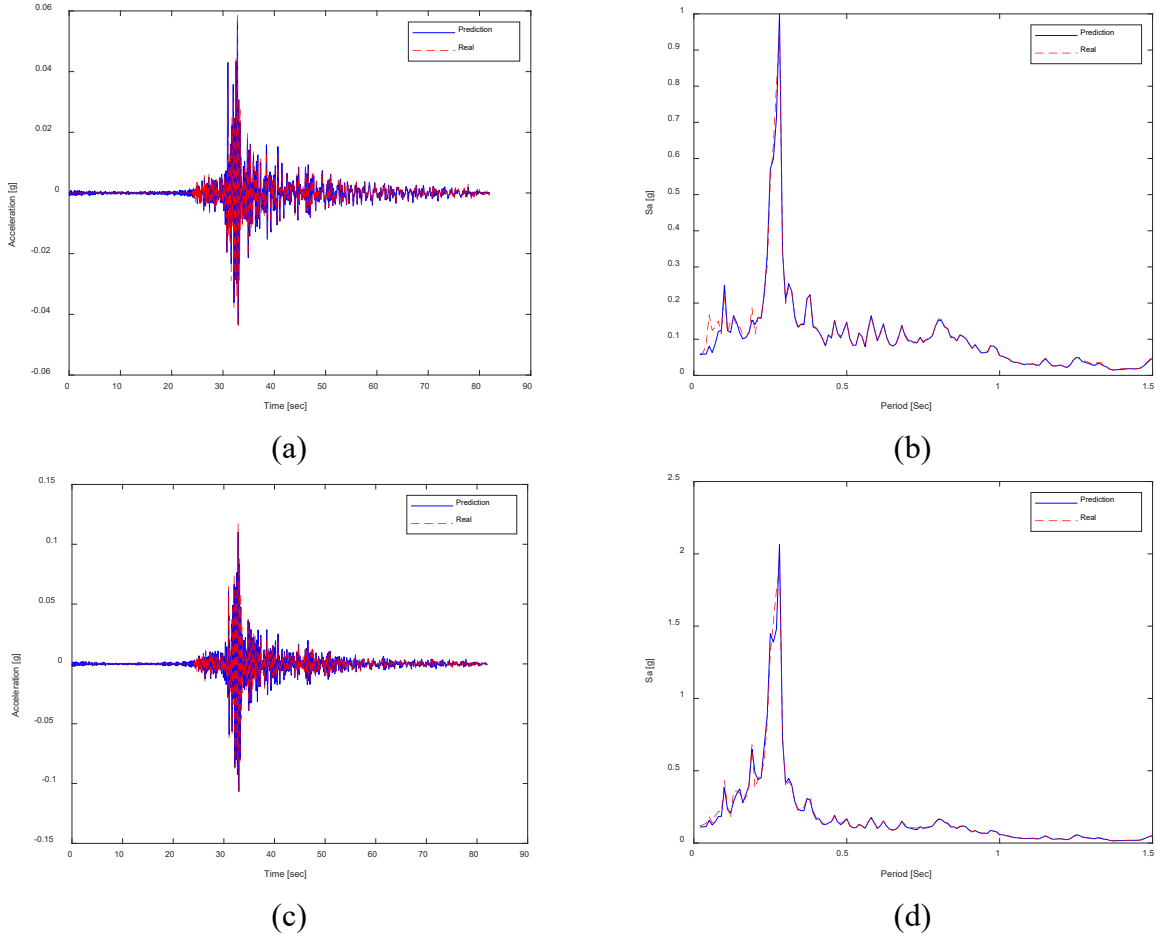
Figure 5. Comparison of predicted and recorded acceleration time history and the corresponding frequency contents in the EW direction of the San Bernardino 6-story building at (a, b) 3rd floor, (c, d) 6th floor (Chino Hills Earthquake of 07 Aug 2012).
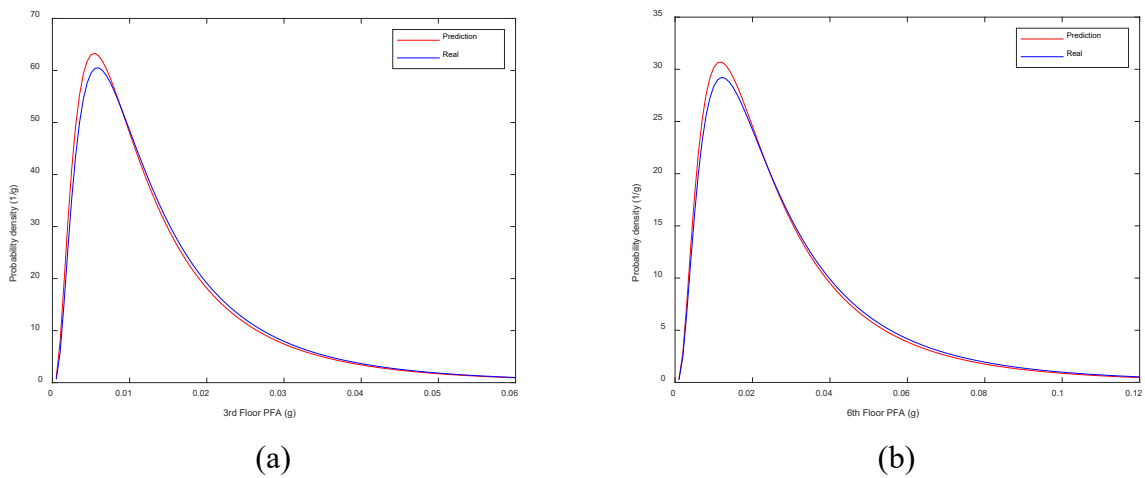

Figure 6. Probability distributions of predicted and recorded PFA of the San Bernardino 6-story building at the (a) 3rd and (b) 6th floors.
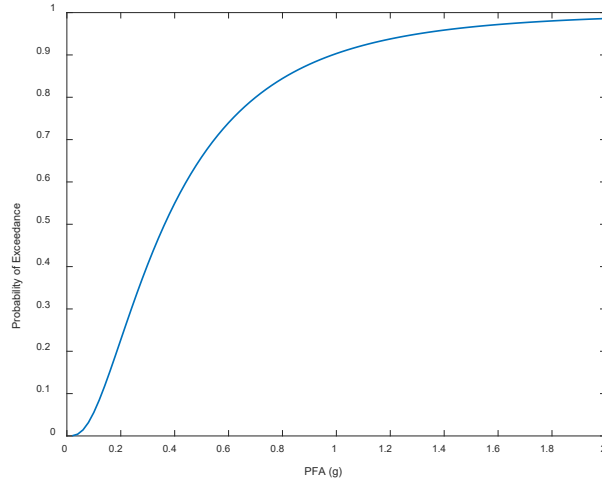
Figure 7. Fragility function for a cooling tower assumed to be located at the 6th floor (roof) of the San Bernardino 6-story building.
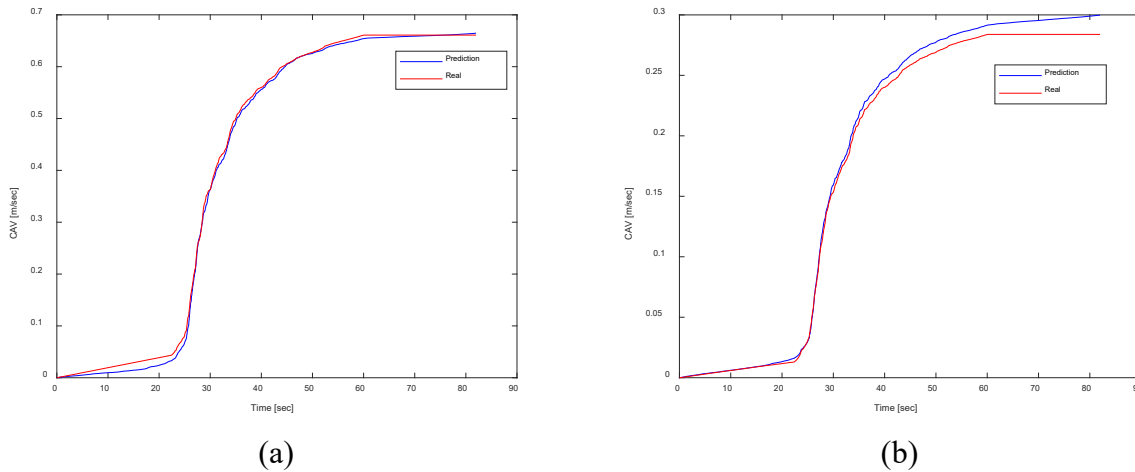

| (a) | (b) |

Figure 8. *CAV* of the true and predicted PFA at the (a) 3rd and (b) 6th floors of the San Bernardino 6-story building (Chino Hills Earthquake of 07 Aug 2012).

Considering these accurate predictions with an 11-motion training set, a parametric study is performed for exploring the minimum number of records needed for acceptable accuracy of the trained model. The number of records used in training is accordingly varied between 1 and 11 and the 3rd and 6th floor accelerations are predicted for each case (Figure 9). Time histories, peak responses, and correlation coefficients are used as parameters for the evaluation of the trained model accuracy. The time history predictions for the Chino Hills Earthquake of 07 Aug 2012 in Figure 9 are similar in general, indicating that the TCN model is capable of accurately learning the entire time history pattern even with 1 or 2 motions. The correct prediction of the time history pattern indicates that the model successfully learns the dominating first mode in this case. This similarity of the predicted time history patterns is also supported by the correlation coefficients in Figure 10(a), which remain unchanged around 0.95 from a training set size of 11 down to 4. However, the error in the peak response, Figure 10(b), increases more dramatically

from 5% for a training set size of 11 to 15% for a training set size of 8. This is attributed to lack of the ability of the TCN model to successfully learn the varying damping ratios over the different levels of motions when the number of motions in the training set is reduced.

From a structural dynamics perspective, the linear elastic response of a Multi-Degree of Freedom (MDOF) system depends on the natural periods, damping ratios, and mode shapes. The response of low and mid-rise buildings is generally governed by the first mode, which is also the case for the San Bernardino 6-story hotel building. Therefore, similar to the SDOF system previously discussed, the features that define the response are the period and damping ratio of the first mode and the ground motion itself (Table 1). It is noted that the response also depends on the mode shape, however the first mode shape and the modal participation factor can be considered as a constant scale factor for all motions and therefore the mode shape is not listed as a feature in Table 1 for this system.

Although all motions are in the linear elastic range as observed by the identified natural periods, damping ratios vary because of the contribution and complexity of different mechanisms to damping at different intensities (Figure 11). The phenomenon of varying damping levels in linear elastic response is well-known (e.g., Chopra, 2012; Cruz and Miranda, 2017). Even for the same motion in forced vibrations or ambient conditions, the damping ratio varies from segment to segment of the motion (Brownjohn et al., 2018). For proper training, the number of motions in the training set should be sufficient to capture different levels of damping ratios. The selected motions should have different intensities to capture these different damping ratios. Therefore, a few motions are not sufficient for learning the damping ratio feature as opposed to the case for the period feature and more motions are needed in the training set for accuracy in predicting the damping. From the results of this case study, 10 ground motions are clearly sufficient for learning these features (period and damping) and for consequent accurate predictions.
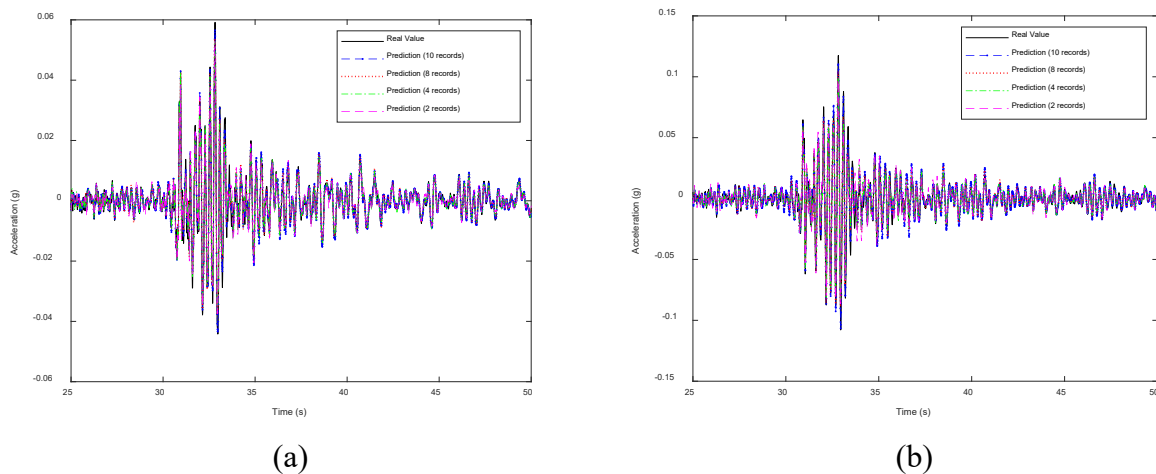

(a)   (b)

Figure 9. Comparison of predicted acceleration time histories for the San Bernardino 6-story building using different number of records in training: (a) 3rd floor, and (b) Roof.
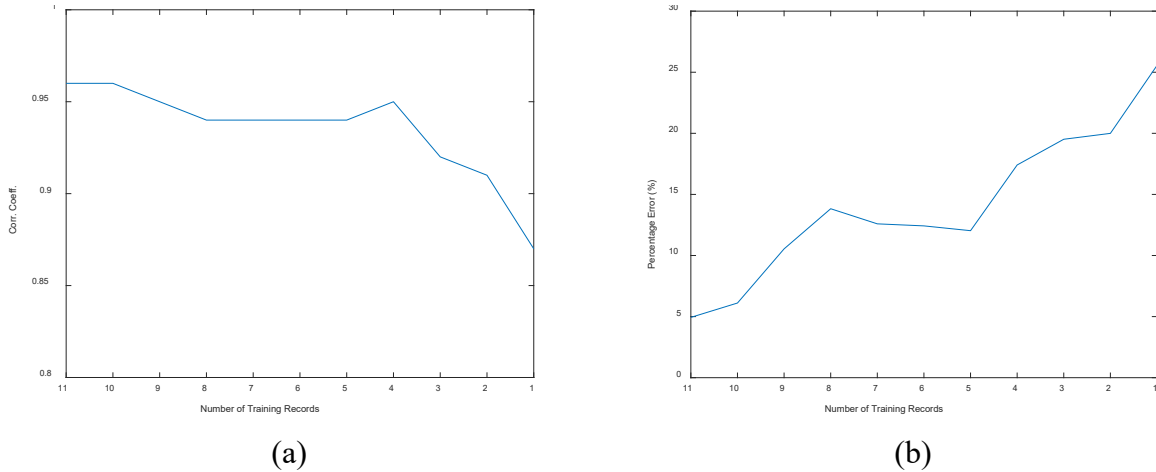
(a)   (b)

Figure 10. Effect of number of records used in the training set for the San Bernardino 6-story building in terms of (a) correlation coefficient of the predictions, and (b) peak error.
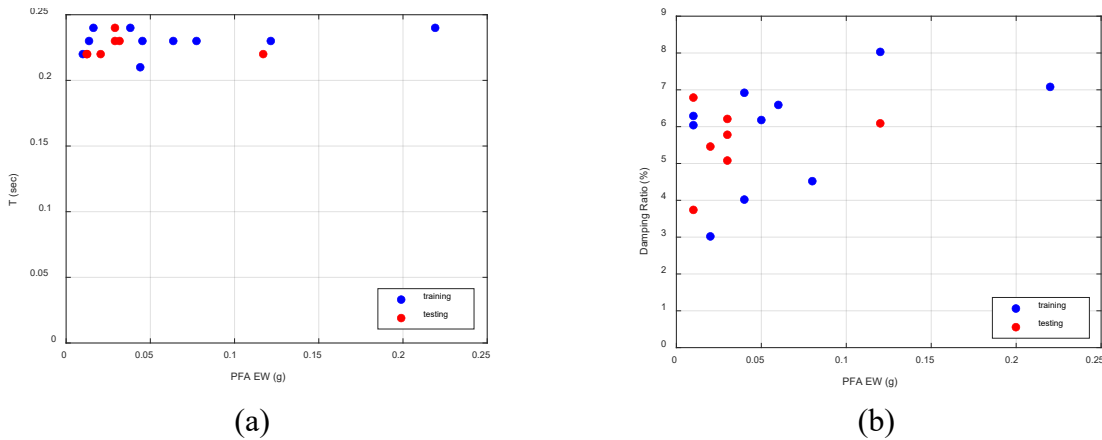

(a)   (b)

Figure 11. Identified (a) fundamental mode periods, and (b) damping ratios of the San Bernardino 6-story building.

4-Story RC Hospital Building in Hemet

To demonstrate that accurate predictions are obtained for similar buildings with similar number of records in the training set, a 4-story hospital building with RCSW structural system (similar to San Bernadino Hotel) is tested using the TCN model. This hospital building was designed and constructed in 1965 and instrumented with 10 accelerometers on three levels in 1976 (Figure 2). Channel 1 at the basement and Channels 9 (2nd floor) & 6 (4th floor, i.e., roof) are respectively used as input and output in the EW direction. In the NS direction, Channel 3 at the basement and Channels 8 (2nd floor) & 5 (4th floor, i.e., roof) are respectively used as input and output. All these sensors are at the center of floors. From the recorded 13 events, refer to Figure 12, 10 are used for training (based on the study of the effect of the training set size for the San Bernardino 6-story building linear elastic response) and 3 are used for testing. As observed in Figure 12, the motions used in the training set cover the entire range of shaking levels recorded on this building and the 3 tested motions are those that lie at the middle of this range.
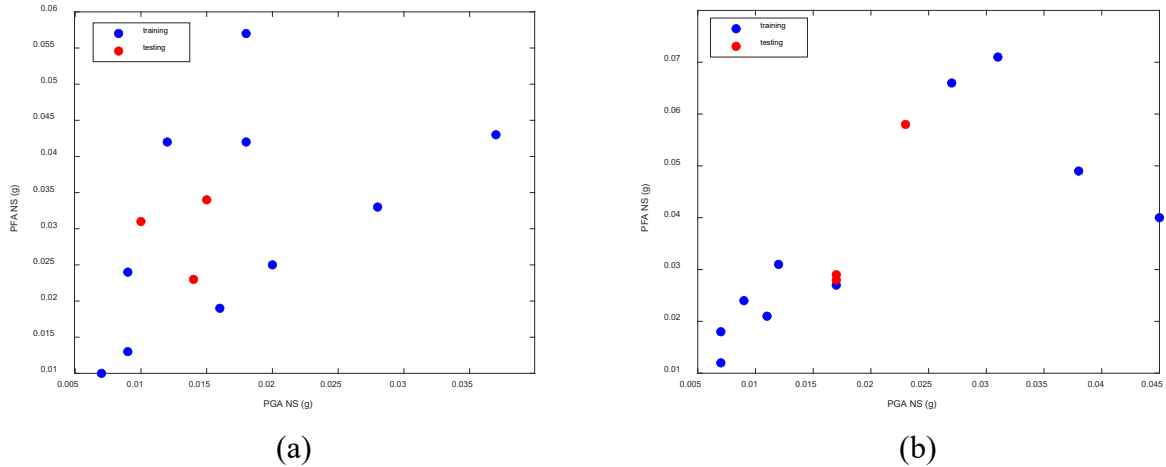
<table>
<tr><td>(a)</td><td>(b)</td></tr>
</table>

Figure 12. The training and testing sets used in the Hemet 4-story building (a) EW, and (b) NS directions.

Similar to the San Bernardino building, high correlation coefficients are obtained for the training and testing sets and unprocessed data provided slightly more accurate predictions (Table 4). Sample predictions are shown for one of the motions in Figure 13, showing the accuracy of the predictions in the NS and EW directions. Similar to the San Bernardino building, the TCN model was successful in learning the entire time history of the response of the building, including its natural period and the varying damping ratios, using 10 motions in the training set.

Table 4. Accuracy of the Hemet 4-story building acceleration predictions in the EW and NS directions.

Data	Correlation Coefficient			
	Training Set EW	Testing Set EW	Training Set NS	Testing Set NS
Unprocessed	97.0%	91.0%	97.0%	90.0%
Processed	97.5%	90.0%	97.5%	90.0%

Linear Elastic Response Prediction of a Tall Building with Higher Modes

Different from low-rise and mid-rise buildings, a tall building seismic response includes higher mode effects. From a structural dynamics perspective, and the corresponding physics-based explanation of the learning process and the predictions, the features that are required to be learned for a tall building are the periods and the damping ratios of several modes contributing to the response (Table 1). The response also depends on the mode shapes, however, as discussed earlier, the mode shape and the modal participation factor can be considered as a constant scale factor in the linear elastic dynamic response of each mode for each motion and accordingly is not considered as an explicit feature. Considering the increased number of features, the presence of multiple modes in the response may introduce additional challenges to the process of learning and accordingly can impact the accuracy of the predictions. Therefore, a 54-story instrumented building is selected to explore the TCN predictions for a case when there are clearly higher

modes present in the response. This 54-story building is a Steel Moment Resisting Frame (SMRF) building with composite slabs of 2.5 inches thick concrete over 3 inches steel deck located at Los Angeles (LA), Figure 14. As shown in this figure, the building is instrumented with 20 accelerometers at the basement (4 levels below ground), ground level, and the 20th, 36th, 46th and penthouse floors. There are Virendeel trusses and 48-inch deep transfer girders at the 36th and 46th floors where vertical setbacks occur. Because there is a sudden change of stiffness at these locations, increased accelerations are expected, and sensors are placed at these floors for monitoring this expected increase of the accelerations.
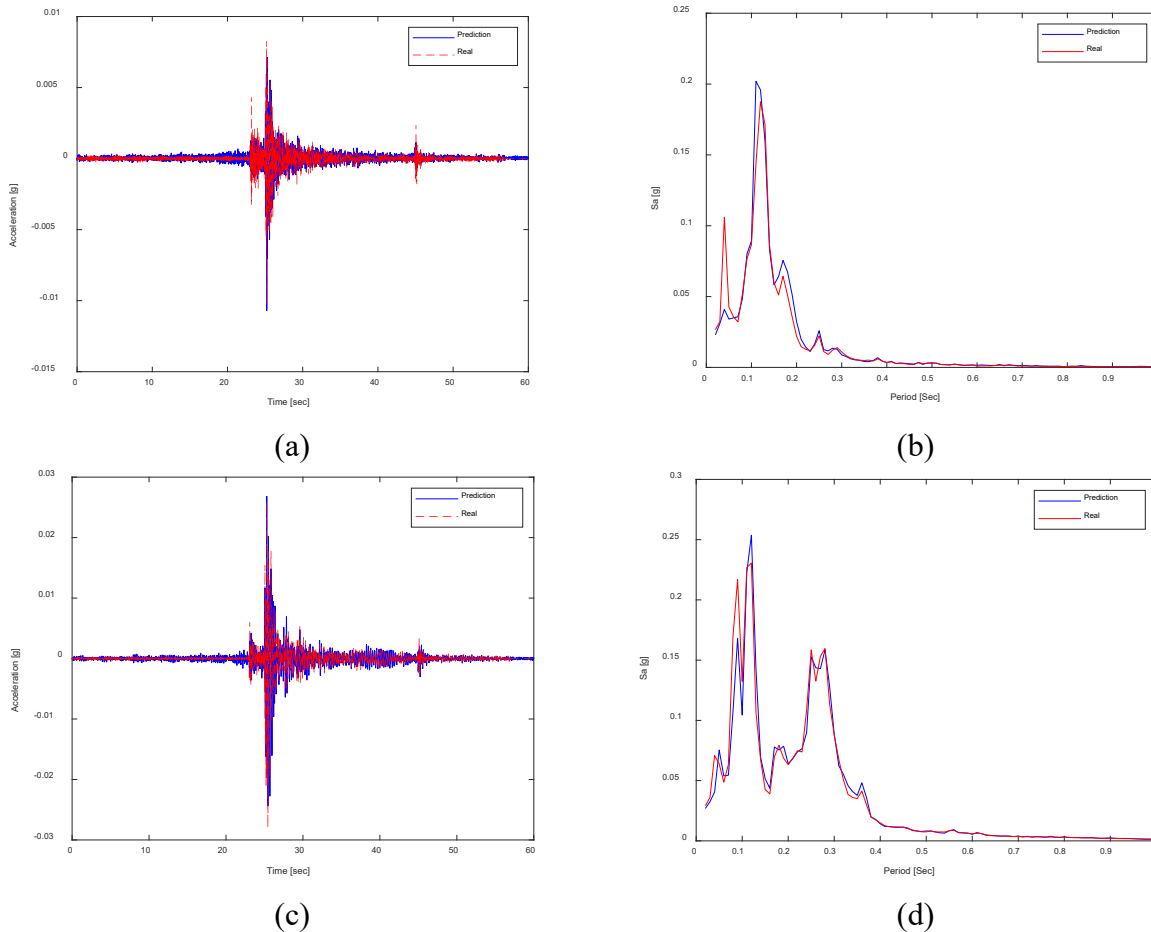

(a)   (b)

(c)   (d)

Figure 13. Comparison of predicted and recorded acceleration time history and the corresponding frequency contents in the (a, b) EW and (c, d) NS directions of the Hemet 4-story building (Banning Earthquake of 06 Jan 2016).
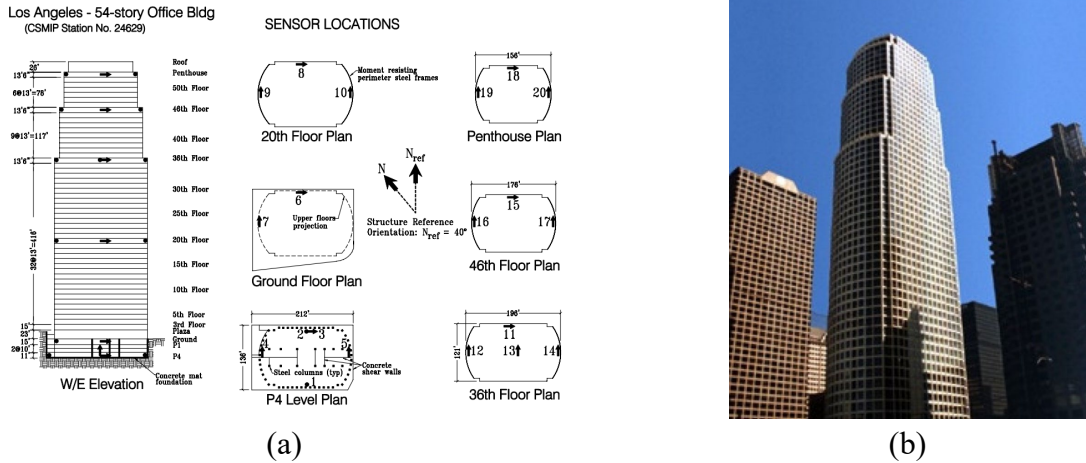
(a)   (b)

Figure 14. Sensor locations and photograph of the 54-story building at Los Angeles.

In this case study, which has 11 recorded motions, 10 motions, same as the number recommended and used, respectively, for the San Bernardino and Hemet buildings, are used for training and the remaining one motion is used for testing (Figure 15). The testing motion in the EW direction is particularly interesting as the PFA is smaller than the corresponding PGA. This can be due to multiple reasons, including (a) the shape of the response spectrum for this motion, where the response acceleration at the first mode period of the building is smaller than the PGA, and (b) multiple modes counteracting and reducing the accelerations. The successful predictions in the EW and NS directions at the 46th floor for the considered test motion are shown in Figure 16. This figure demonstrates that the trained TCN model is successful in learning more complex responses obtained as a superposition of multiple modes and the 10-motion training set results in accurate responses as in the cases of San Bernardino and Hemet buildings.
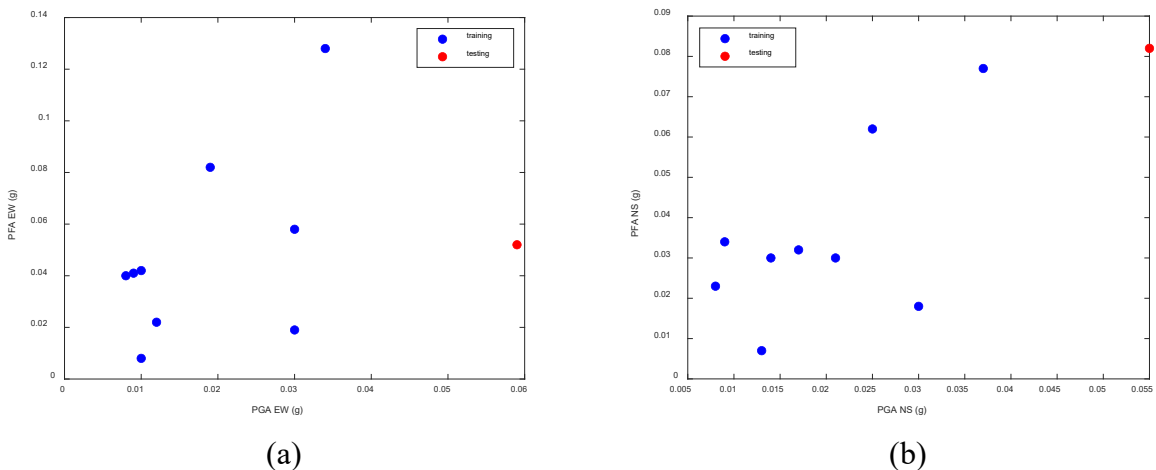

(a)   (b)

Figure 15. The training and testing sets used for the LA 54 story building (a) EW, and (b) NS directions.

16

<div align="center">(a)</div>
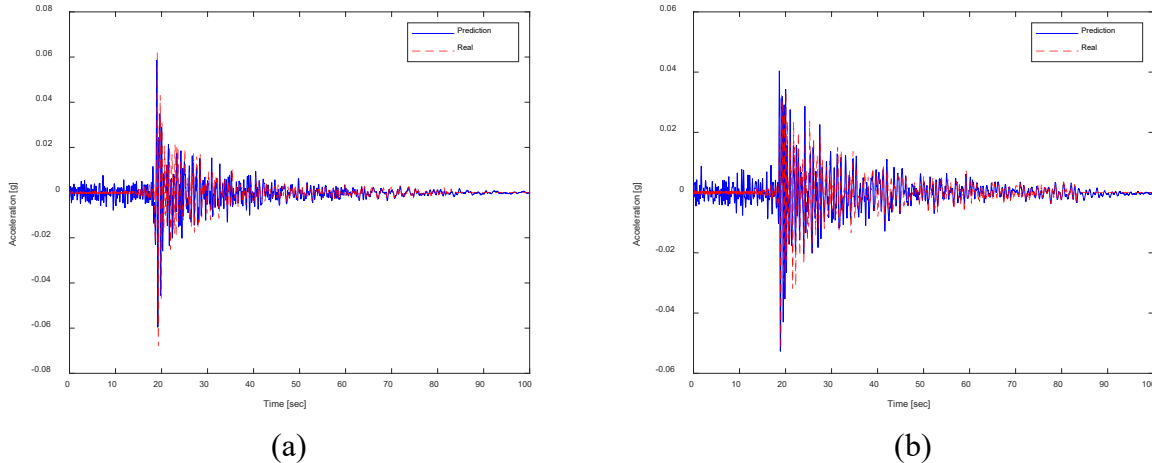

<div align="center">(b)</div>

Figure 16. The 46th story acceleration predictions for the 56-story building in LA: (a) EW, and (b) NS directions (Chino Hills Earthquake of 29 July 2008).

Nonlinear Response Prediction

The periods of the San Bernardino 6-story building in the EW and NS directions are identified in Figure 17. The identified periods in the EW direction are almost constant in the tight range of 0.21 to 0.24 sec, independent of the level of shaking, which is indicative of linear elastic response. On the other hand, the periods in the NS direction clearly increase with the level of shaking, indicating nonlinear response. Although it is not entirely clear why this period elongation motion occurs because all ground motions in the training set are relatively low-level motions, potential reasons are minor cracking, foundation rocking, disengagement of partition walls that could provide stiffness, or the loss of contributions from any other nonstructural components.

Although this nonlinear response is not extensive, it presents a more challenging case for prediction compared to the linear elastic response and is therefore discussed here. To predict the response in the NS direction, the first attempt used the same 11 motions that were used in the EW direction. Because of the mentioned nonlinear response, the obtained predictions were not accurate. An example of inaccurate prediction is shown in Figure 18 for the Loma Linda Earthquake of 08 Oct 20126. One clear reason for the mismatch in the prediction is the difference in the dominant frequency of the motion indicating that the TCN model was not able to capture well the period elongation as a function of the ground shaking intensity, which is a relevant feature needed to characterize the nonlinear response (Table 1). As mentioned earlier, the total number of events recorded for this building is 26. To explore if increasing the number of motions used for training facilitates capturing the period elongation and improves the accuracy, 23 of the 26 motions, covering the entire range of shaking levels, are used for training as shown in Figure 19 and three events laying in the middle of the range are used for testing. The results show the increased accuracy of the predictions as demonstrated in Figure 20 for one of the motions in the testing set. Particularly, the time history, the peaks, and the frequency contents are well matched, indicating that increasing the number of motions in the training set from 11 to 23

<div align="center">17</div>

led to successful learning of the increase of the period elongation with increased shaking intensity.
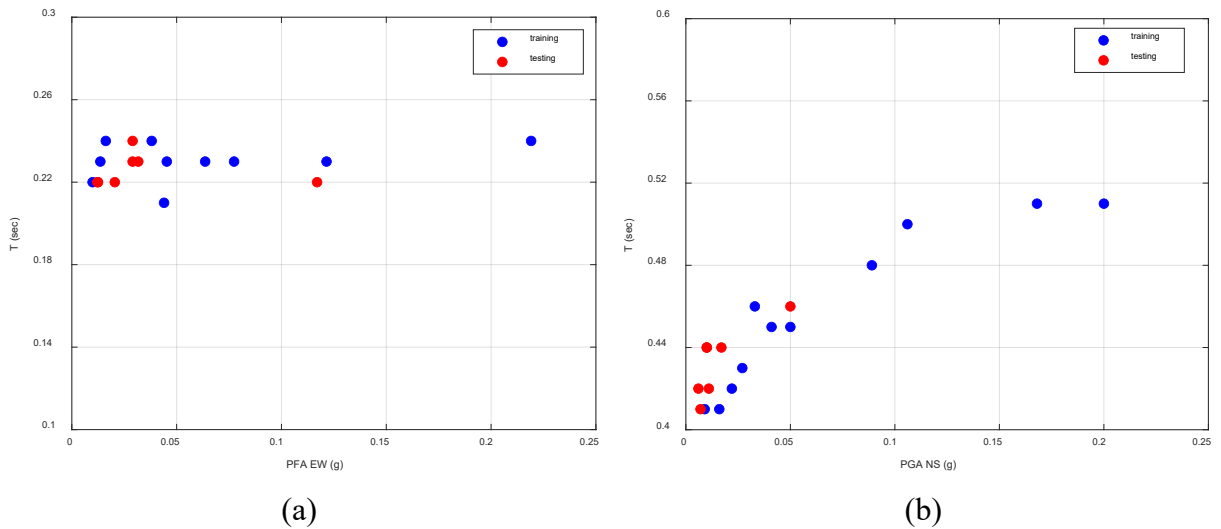

(a)   (b)

Figure 17. Identified periods of the San Bernardino 6-story hotel building in (a) EW, and (b) NS directions in different earthquakes.

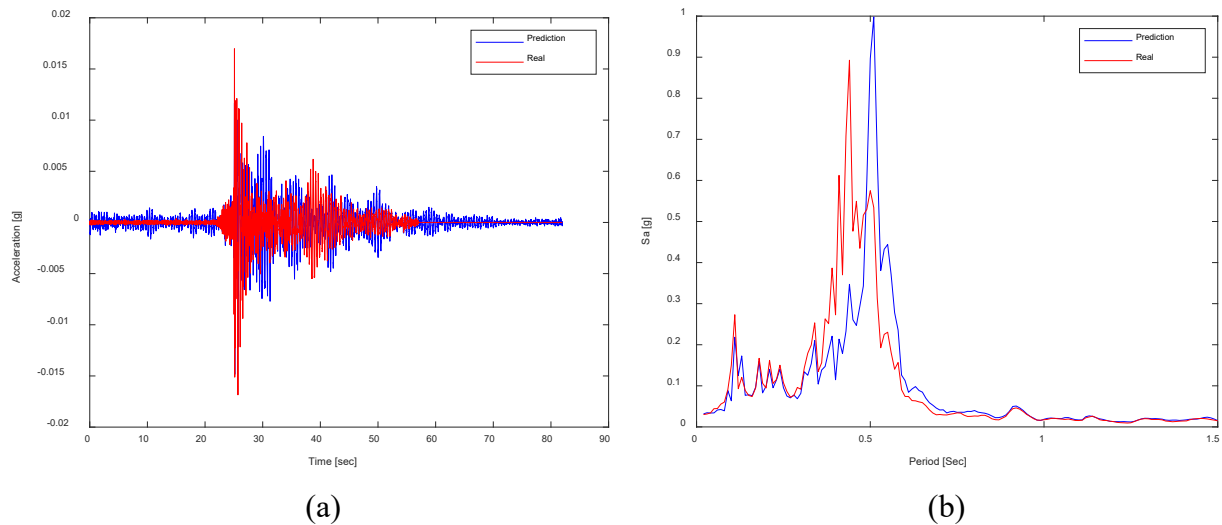(a)   (b)

Figure 18. Comparison of inaccurately predicted and true (a) acceleration time history, and (b) the corresponding frequency content, in the NS direction of the 6-story building in San Bernardino (Fontana Earthquake of 25 July 2015).
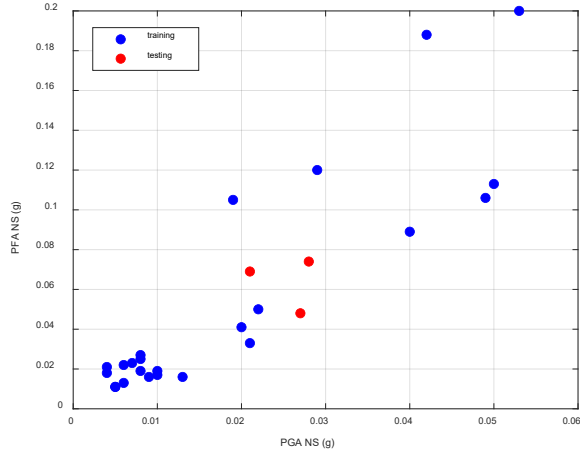
Figure 19. The set used in the San Bernardino 6-story building NS direction to improve accuracy (Testing data includes three moderate events and all others used for Training data).

(a)	(b)
(c)	(d)

Figure 20. Comparison of (improved) predicted and recorded acceleration time history and the corresponding frequency contents in the NS direction of the San Bernardino 6-story building at (a, b) 3rd floor, (c, d) 6th floor (Chino Hills Earthquake of 07 Aug 2012).
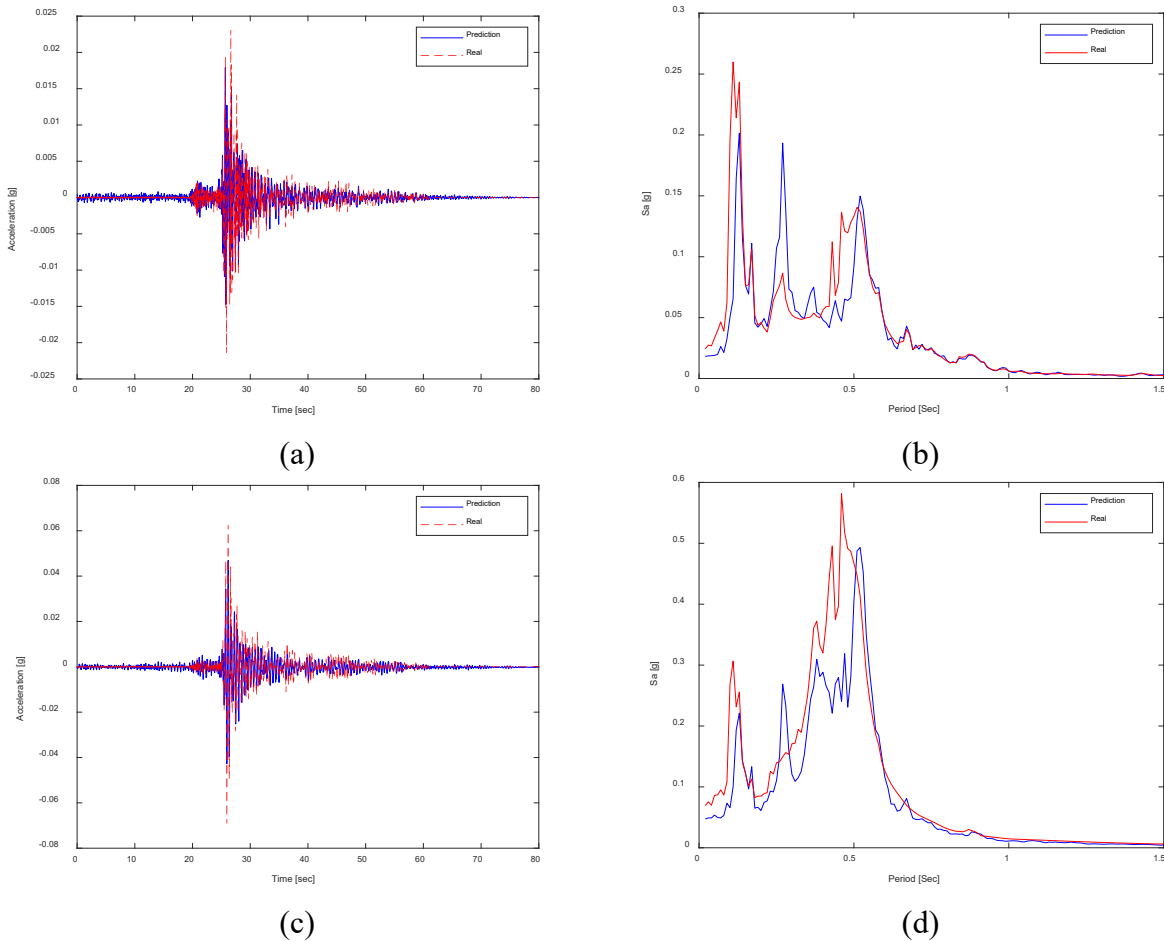
These successful predictions highlight an important and unique characteristic of obtaining the response using a machine learning approach. As discussed earlier, the potential reasons for the observed period elongation with increased intensity of shaking are concrete cracking, foundation rocking, and disengagement of partition walls or the loss of contributions from any other nonstructural components. None of these aspects are considered explicitly in the common physics-based computational models developed for dynamic analysis. Even if they are modeled, there is a large epistemic uncertainty associated with this type of modeling. Therefore, the obtained data-driven TCN model results show that the adopted machine learning approach fills this gap very well and results in accurate structural response prediction that would not be possible using conventional means. This case study also highlights two important aspects worthy of future investigation, namely, the effect of increased training dataset (justifying need for more instrumented systems) and use of physics-based and data-driven models hand in hand in a digital twin setting of the different structural systems where the digital twin complements and helps interpreting findings from the physical twin.

Conclusions and Future Directions

This paper focused on the use of Temporal Convolutional Network (TCN) models for obtaining the structural response in the form of time histories. Models were trained using the data from several instrumented buildings with different characteristics to predict the response. The results were explained using concepts of structural dynamics and applications in earthquake engineering. The conclusions of the study are summarized as follows:

1. The developed TCN Model was verified by training and testing on a linear elastic Single Degree of Freedom (SDOF) system.
2. The use of raw data results in more accurate predictions as compared to the use of California Strong Motion Instrumentation Program (CSMIP) processed data. This is because the processed output is not necessarily the direct result of the processed ground motion input. Therefore, the relationship between the input and output deviates slightly from true physics when processed data is used for input and output.
3. The TCN model was successful for systems that are characterized by not only relatively simple features, such as a numerical SDOF system characterized by a single natural period and damping ratio, but also those with more complex response such as a tall building with multiple modes of vibration contributing to the overall response.
4. A training set size of 10 motions was sufficient for predicting the response of low-, mid-, and high-rise buildings in the linear elastic range.
5. The correlation coefficient and error in peak response resulted in different conclusions about the minimum number of records needed for accuracy. The error in peak response should be used as the preferred parameter for evaluating the accuracy, as the peak response is commonly used for design, assessment, and Performance-Based Earthquake Engineering (PBEE) and needs to be predicted accurately.
6. The training dataset should include enough motions with varying intensities, frequency contents, and other characteristics for the TCN model to learn the dynamic

characteristics of the buildings (denoted as features) as well as the relationship between the ground motion frequency contents and intensities and these dynamic characteristics.

7. The probability distributions of the predicted and true peak responses were observed to be quite similar. This demonstrated that the TCN model predictions can be confidently used for characterizing the response to multiple ground motions, which is required by building standards and PBEE.

8. The predicted and true responses from multiple test motions, along with relevant fragility functions, were used to compute the probability of damage of a cooling tower assumed to be located at the roof of one of the instrumented buildings. The resulting probability of damage was very close using the true and precited responses. This preliminary exercise provides confidence in the model predicted responses to detect nonstructural (and structural) damage.

9. To demonstrate the importance of predicting the entire time history, Cumulative Absolute Velocity (*CAV*), a parameter closely correlated to damage, was computed using the predicted and true responses and the resulting *CAV* time histories were very close to each other.

10. The slight nonlinear response of the San Bernardino 6-story building in the NS direction, as indicated by the period elongation with increasing shaking intensity, was successfully predicted by the TCN model using a 23-motion training set. As expected, the required number of motions in the training set was larger than that needed for the elastic response, but it was a manageable number, given the available records of this case study. The number of recorded motions required for accurate training is expected to increase with the increased level of the nonlinear response.

11. The successful predictions of the nonlinear response highlighted that a machine learning approach can be a viable solution to predict this response accurately, as the potential sources of the specific nonlinearity observed here are very rarely considered with confidence in conventional physics-based computational models in common engineering practice.

Several planned near-future studies include: (1) application of the TCN models to buildings with (a) irregularities (such as torsion), (b) larger levels of nonlinear response, and (c) potential soil-structure interaction, (2) prediction of displacements, and (3) predicting the responses of selected instrumented buildings in future earthquakes, among others.

Acknowledgements

References

Applied Technology Council (ATC, 2018). Seismic Performance Assessment of Buildings Volume 1 – Methodology. Report No. FEMA-P58, Redwood City, California.

Applied Technology Council (ATC, 2018). Seismic Performance Assessment of Buildings Volume 2 – Implementation. Report No. FEMA-P58, Redwood City, California.

ASCE. 2022. Minimum design loads for buildings and other structures. ASCE/SEI 7-22. Reston, VA: ASCE.

Brownjohn, J.M.W., Au, S.K., Zhu, Y., Sun, Z., Li, B., Bassitt, J., Hudson, E. and Sun, H., 2018. Bayesian operational modal analysis of Jiangyin Yangtze River bridge. *Mechanical Systems and Signal Processing*, 110, pp.210-230.

Chen, Y., Sun, Z., Zhang, R., Yao, L. and Wu, G., 2023. Attention mechanism based neural networks for structural post-earthquake damage state prediction and rapid fragility analysis. *Computers & Structures*, 281, p.107038.

Chopra A.K. 2017. Dynamics of Structures, Theory and Applications to Earthquake Engineering, 5th Edition. Hoboken, NJ, Pearson Education, 960

Cruz, C. and Miranda, E., 2017. Evaluation of damping ratios for the seismic analysis of tall buildings. Journal of Structural Engineering, 143(1), p.04016144.

Günay, S. and Mosalam, K.M., 2013. PEER performance-based earthquake engineering methodology, revisited. *Journal of Earthquake Engineering*, 17(6), pp.829-858.

Kundu, A. and Chakraborty, S., 2020, September. Deep learning-based metamodeling technique for nonlinear seismic response quantification. In *IOP Conference Series: Materials Science and Engineering* (Vol. 936, No. 1, p. 012042). IOP Publishing.

Lea, C., Flynn, M.D., Vidal, R., Reiter, A. and Hager, G.D., 2017. Temporal convolutional networks for action segmentation and detection. In proceedings of the *IEEE Conference on Computer Vision and Pattern Recognition* (pp. 156-165).

Li, B. and Spence, S.M., 2022. Metamodeling through deep learning of high-dimensional dynamic nonlinear systems driven by general stochastic excitation. *Journal of Structural Engineering*, 148(11), p.04022186.

Muin, S. and Mosalam, K.M., 2018, October. Localized Damage Detection of CSMIP Instrumented Buildings using Cumulative Absolute Velocity: A Machine Learning Approach. In Proceedings of the SMIP18 Seminar on Utilization of Strong-Motion Data, Sacramento, CA, USA (Vol. 25).

Muin, S. and Mosalam, K.M., 2017. Cumulative absolute velocity as a local damage indicator of instrumented structures. *Earthquake Spectra*, 33(2), pp.641-664.

Park, Y.J. and Ang, A.H.S., 1985. Mechanistic seismic damage model for reinforced concrete. *Journal of Structural Engineering*, 111(4), pp.722-739.

Park, Y.J., Ang, A.H.S. and Wen, Y.K., 1985. Seismic damage analysis of reinforced concrete buildings. *Journal of Structural Engineering*, 111(4), pp.740-757.

Zhang, R., Chen, Z., Chen, S., Zheng, J., Büyüköztürk, O. and Sun, H., 2019. Deep long short-term memory networks for nonlinear structural seismic response prediction. *Computers & Structures*, 220, pp.55-68.

Zhong, K., Navarro, J.G., Govindjee, S. and Deierlein, G.G., 2023. Surrogate modeling of structural seismic response using probabilistic learning on manifolds. *Earthquake Engineering & Structural Dynamics*, 52(8): 2407-2428.

INHERENT DAMPING DURING NONLINEAR SEISMIC RESPONSE

Dionisio Bernal

Civil and Environmental Engineering Department, Center for Digital Signal Processing,
Northeastern University, Boston MA 02115

Abstract

An approach to interrogate measured response on the behavior of inherent damping during nonlinear excursions is presented. The scheme computes a signal that approximates the base shear (to within a scalar) and decides on the inherent damping during nonlinear excursions on the premise that the derivative of this signal, with respect to time, is small within these segments. Preliminary results suggest that the inherent damping model should include a reduction in effectiveness when hysteretic dissipation is activated.

Introduction

A long-standing open question in evaluating the response of buildings to strong earthquakes is whether the model used to capture energy dissipation not associated with damage should be modified, or remain unchanged, when hysteretic behavior is activated [1-6]. This question has been difficult to resolve because the inherent damping model is a surrogate for the aggregate of a number of unspecified mechanisms, calibrated to match decay rates observed for small vibrations, but for which there is no mechanistic support. We note in passing that use of mass and stiffness matrices to specify the classical damping model (wherein damped and undamped eigenvectors coincide, as is the case in the Rayleigh model or in the more general Caughey series [7,8]) is justified by the simplicity that it brings but is not mechanistically supported.

Lack of a mechanistic model for inherent damping indicates that (apart from consistency from an energy perspective) the only way to decide on the merit of any postulated model is from seismic response observations. On the question of coupling between hysteresis and pseudo-viscosity the main obstacle to a data-supported resolution comes from the fact that the stiffness restoring forces cannot be directly measured and cannot be estimated with sufficient accuracy from a model to allow computation of the damping forces from equilibrium. We attempt to make some headway by shifting the focus from dynamic equilibrium to the rate of change of the terms in the equilibrium equations and by simplifying the spatial distribution of the damping forces (to be described). The information infused to arrive at a workable scheme is the contention that the rate of change of a scalar measure of the unknown stiffness contribution, not always, but in many cases, is small enough to be discarded. We designate the interrogation scheme that results from the previous ideas as the "Inherent Damping Nonlinear Behavior" (IDNB) extractor. This paper

presents the theoretical support of IDNB, reports on the current progress in its validation and limitations and includes some initial results from application to data recorded during strong shaking in buildings from the CSMIP database.

The Basic Ideas

Let $I(t), D(t), R(t)$ represent the vectors of inertia, damping and restoring forces during a generally nonlinear response. Equilibrium for base excitation requires that

$$I(t) + D(t) + R(t) = 0 \tag{1}$$

our goal is to determine if something can be said, primarily from data, about what happens to the mechanism that generates $D(t)$ during intervals when $R(t)$ reflects significant nonlinearity. To move forward we pre-multiply by the transpose of the column vector of ones (r when used subsequently) and introducing obvious notation write

$$V_R(t) = -\big(V_I(t) + V_D(t)\big) \tag{2}$$

To make things tractable we take the damping forces at any time as those that would have existed if the damping matrix was invariant, times a modulation that is to be determined, namely, we take them as

$$D(t) = \rho(t)C_0\dot{u}(t) \tag{3}$$

where $\dot{u}(t)$ =vector or relative velocities and $\rho(t)$ is a scalar. Differentiating Eq.3 with respect to time and substituting the result into the derivative of Eq.2 writes

$$\dot{V}_R(t) = -\Big(\dot{V}_I(t) + \rho(t)r^T C_0\ddot{u}(t) + \dot{\rho}(t)r^T C_0\dot{u}(t)\Big) \tag{4}$$

Results of numerical simulations suggest that the third term on the right-hand side of Eq.4 is small compared to the other two, so we simplify by taking $\dot{\rho}(t) = 0$ and get

$$\dot{V}_R(t) = -\Big(\dot{V}_I(t) + \rho(t)r^T C_0\ddot{u}(t)\Big) \tag{5}$$

Assume, temporarily, that the disjointed time intervals when inelasticity is extensive have been determined and have been aggregated into the time segment $\tilde{t}$. Restricting evaluation of Eq.5 to these times one has

$$\dot{V}_R(\tilde{t}) = -\Big(\dot{V}_I(\tilde{t}) + \rho(\tilde{t})r^T C_0\ddot{u}(\tilde{t})\Big) \tag{6}$$

At this point we replace $\rho(\tilde{t})$ with a constant $\bar{\rho}$ and while the equality cannot hold at all times after this replacement, it can be preserved at the level of norms, so we take the 2-norm and get

$$\left\|\dot{V}_R(\tilde{t})\right\| = \left\|\left(\dot{V}_I(\tilde{t}) + \bar{\rho}r^T C_0 \ddot{u}(\tilde{t})\right)\right\| \tag{7}$$

where it's a simple matter to show that

$$\dot{V}_R(\tilde{t}) = r^T K_T(\tilde{t})\dot{u}(\tilde{t}) \tag{8}$$

with K_T=structure's tangent stiffness. Substituting Eq.8 into Eq.7 writes

$$r^T K_T(\tilde{t})\dot{u}(\tilde{t}) = -\left(\dot{V}_I(\tilde{t}) + \rho(\tilde{t})r^T C_0 \ddot{u}(\tilde{t})\right) \tag{9}$$

Since $K_T(\tilde{t})$ is not known the *lhs* of Eq.9 cannot be explicitly evaluated, but if the term is small, relative to $\|r^T C_0 \ddot{u}(\tilde{t})\|$, it appears reasonable to decide on $\bar{\rho}$ as the value that minimizes the *rhs* of the Eq.7. We can summarize as follows:

- The IDNB scheme computes a value, $\bar{\rho}$, such that the inherent damping during nonlinear excursions is estimated as $\xi_{non} = \bar{\rho}\xi$, where ξ is the damping ratio that holds if the structure behaved linearly. The value of $\bar{\rho}$ is taken as that which minimizes the rhs of Eq.7

Is the Discarded Term Small Enough?

A necessary condition for minimization of the *rhs* Eq.7 to give meaningful results for $\bar{\rho}$ is that

$$\left\|r^T K_T(\tilde{t})\dot{u}(\tilde{t})\right\| \ll \left\|\left(r^T C_0 \ddot{u}(\tilde{t})\right)\right\| \tag{10}$$

In a shear building where first story yielding dominates the *lhs* of Eq.10 is exactly zero (in the absence of strain hardening) and the inequality is guaranteed satisfied. In general, however, one does not know if this is so, and it seems that all that can be said is that if it's not satisfied $\bar{\rho}$ will be overestimated. It is not unreasonable to wonder whether the constraint in Eq.10 is ever satisfied when real data is considered so we tried to see if a relation that shed some light on the question could be derived. A useful expression obtained using approximations with bounded errors could not be found but a very rough result is as follows: assume the damping matrix C_0 is stiffness proportional with a fundamental mode damping ξ, so that $C_0 = 2\xi\omega^{-1}K$ and express the tangent stiffness as a fraction of the initial matrix, namely $K_T = \eta K$. With these replacements and taking $b = r^T K$ one finds that Eq.10 translates to $\eta\|b\dot{u}(\tilde{t})\| \ll 2\xi\omega^{-1}\|b\ddot{u}(\tilde{t})\|$ which, taking $\|b\ddot{u}(\tilde{t})\| \cong \omega\|b\dot{u}(\tilde{t})\|$ gives $\eta \ll 2\xi$. The foregoing states that satisfaction of the constraint hinges on the tangent stiffness scaling being small compared to twice the critical damping ratio of the fundamental mode. This examination is too rough to allow

solid assertions, but it appears to leave open the possibility that the constraint may be satisfied, which would not be the case if the result had been $\eta \ll 0.02\xi$.

On the selection of $\tilde{t}$

The signal in Eq.9 is a reordered version of the signal of Eq.5, subsequently truncated to a length $\tilde{t}$. The reordering is done with the goal of making the early values have a high probability of being points when inelasticity is extensive, with the approach used thus far being to order the points in increasing absolute value. The truncating length $\tilde{t}$ is in principle the aggregate length of all the yielding segments (although a fraction should also work) and in the numerical section we've taken it to be within 1 to 2% of the strong motion.

Inherent Damping Models

Since the inherent damping behavior is unknown, validation of IDNB must be carried out in simulations. Specifically, one postulates various inherent damping models that are coupled with the hysteresis response as well as constant damping one and the goal is to determine whether or not IDNB can discriminate between them using signals from a limited number of floors (plus information on the location of the sensors and the relative values of the story weights). For this purpose, we selected 3 previously proposed inherent damping models plus a new one introduced here designated as the $CSMIP\kappa$ model. Nonlinear damping models that require that the eigenvalue problem be solved each time the tangent stiffness changes have also been proposed but we decided not to include them since they are computationally expensive and have not been put forth with compelling theoretical support.

Rayleigh Damping with Tangent Stiffness

A generalization of the widely used Rayleigh damping model, introduced to realize a loss of effectiveness during plasticity takes the damping matrix, C, as

$$C = \alpha M + \beta K_T \tag{11}$$

where M = mass matrix, K_T = tangent stiffness matrix and α, β are constants. The complexity with which the tangent stiffness is formed can vary from the simple elasto-plastic hinges to the much more computationally intensive distributed plasticity models that are widely used in research but less so in conventional seismic engineering practice. Since the model of Eq.11 is the same as the standard Rayleigh model during elastic response, computation of the constants α, β is not affected by the anticipated nonlinearity. The model in Eq.11 has been around for a long time and is sometimes viewed with reservation because of the abrupt changes in the damping that accompany the changes in stiffness in lumped plasticity models and because it can reach

conditions where the damping can add energy to the system because some eigenvalues turn negative. The first item leads to unbalances that are highly localized in time and have little effect in the global response and the second, except perhaps in studies where the focus is dynamic instability, is seldom active. We take the opportunity to note, however, that a potentially important issue in modeling damping, albeit not restricted to the Rayleigh model, is the appearance of unbalanced forces at massless coordinates [9,10].

Luco and Lanzi (2017)

Luco and Lanzi [6] introduced a model where the damping matrix is taken as

$$C = C_0 K^{-1} K_T \tag{12}$$

where C_0 is any arbitrary damping matrix and K is the initial stiffness. One issue that is worth noting in the model of Eq.12 is that the matrix C is not necessarily symmetrical.

Lanzi and Luco (2018)

Shortly after the appearance of the model in Eq.12 the same authors propose a model for the damping that writes [10]

$$C = K_T K^{-1} C_0 K^{-1} K_T \tag{13}$$

which removes the noted lack of symmetry and eliminates the possibility of negative eigenvalues. The reason for the last observation being that the damping matrix in Eq.13 is a congruent transformation of C_0, and congruent transformations do not change the number of positive, negative and zero eigenvalues of a matrix. A curious byproduct of the same property is the fact that as an eigenvalue of the tangent stiffness approaches zero the dissipation in a particular velocity pattern does the same but if the inelasticity continues and some eigenvalue of the second order tangent stiffness is rendered negative the dissipation increases again.

CSMIPκ

A feature common to all the previous models is that they cannot be modified in the plastic range without changing behavior when the response is linear. The model introduced in this project, which takes the damping matrix as

$$C = \left(\frac{\|K_T\|}{\|K\|}\right)^\kappa C_0 \tag{14}$$

where C_0 is arbitrary, κ is a free parameter and $\|.\|$ stands for the 2-norm, has this tunning ability. As can be seen, when $\kappa = 0$ the model reverts to a constant damping matrix and as κ increases the magnitude of the inherent damping during the inelastic response decreases.

On the Damping Matrix for Small Amplitude Response

Evaluation of the *rhs* of Eq.9 requires that a damping matrix for the initial elastic response, C_0 be established; some possibilities are discussed next.

Classical Damping

Any classical damping matrix can be written as

$$C = M\left(\sum_{j=1}^{n} \vartheta_j \phi_j \phi_j^T\right)M \tag{15}$$

where $\vartheta_j = 2\omega_j \xi_j$ and ϕ_j, ω_j and ξ_j are the mass normalized mode shape, frequency and the damping ratio of the jth mode, respectively. In an experimental setting the rank of the matrix in Eq.15 will equal the number of identified modes and there is, of course, the issue of having only a limited number of monitored levels, which requires that the mode shapes be expanded. The rank issue is not expected to have practical relevance but the need for a significant identification effort followed by modal expansion does not make Eq.15 attractive.

Identification Free Extraction

If the response is measured at all coordinates the damping matrix can be extracted from the data without requiring system identification. The scheme shares with Eq.15 the fact that the mass matrix must be known but no modal truncation is incurred. To illustrate let the seismic response prior to the development of inelastic action be gathered in matrices $\ddot{Y}, \dot{U}, U \in \mathfrak{R}^{n \times N}$ containing, as columns, vectors of absolute acceleration, relative velocities and relative displacements, with *n*=number of levels in the building and N =the total number of time steps used. Since we've assumed that the response is linear during the data collection one can write

$$M\ddot{Y} + C\dot{U} + KU = 0 \tag{16}$$

Selecting $N > n$ guarantees there are right null spaces and taking

$$U\Gamma = 0 \tag{17}$$

one has (from Eq.16)

$$C\dot{U}\Gamma = -M\ddot{Y}\Gamma \qquad (18)$$

so the damping matrix is given by

$$C = -M\ddot{Y}\Gamma(\dot{U}\Gamma)^{+} \qquad (19)$$

where the superscript + stands for pseudo inversion. If the mass matrix is known and all the levels are measured Eq.19 would be the method of choice but in the common scenario where only some levels are measured the reconstruction of the response may introduce significant error, so we do not opt for this alternative either.

Mass Proportional Damping

A simple and very convenient approach for our purposes is to take the initial damping matrix as mass proportional. The reason being that in this case both the first and the second terms on the *rhs* of Eq.9 are proportional to M and this eliminates dependence on the actual values of the mass, leaving only the much simpler demand of estimating the relative values. Another attractive feature being that sensor density has no effect on the estimation of C_0 and that all that is required from system identification is an estimate of the frequency and damping of the fundamental mode. There is, in fact, not even a need to separate these two quantities since their product is the real part of the pole of the fundamental mode, which is what is actually computed in the identification. It is true, of course, that the mass proportional model allows control over one mode only, but one suspects that this is not a significant issue in this case.

Response Reconstruction

The large majority of instrumented structures for which records are available have sensors in a subset of all the floors so to apply IDNB it is necessary to reconstruct the response in some levels. Much has been done in this area and there are techniques with various levels of refinement [11,12]. Interpolation schemes are projections of the measurements on a basis that covers the full building height. These bases can be defined using estimated mode shapes or determined by functions that depend on the position of the sensors, as is the case in the widely used Cubic Spline (CS) or can be interpolations of the left side singular vectors of the data matrix (in which case the response can be segmented, and different basis formulated for different time intervals). In all cases, however, if inelasticity produces localized distortions, the results can degrade notably. Consider, for example, a two-story structure where the second floor and the ground are measured, and one is interested in estimating the drift in both levels. In the linear case reasonable results are expected but in the nonlinear case the true response (but not the prediction) will be strongly dependent on the distribution of the inelasticity.

To illustrate quantitatively consider an 8-story shear structure with sensors only on the even number floors and assume one is to reconstruct the unmeasured floors using a cubic spline.

Fig.1 plots the reconstructed absolute acceleration in the 7th level and compares it with the exact result for two conditions, one where the earthquake is scaled so that the response is linear and the other where inelasticity is significant. As can be seen, the accuracy in the case of the linear response is good but in the case with nonlinearity the error is important.
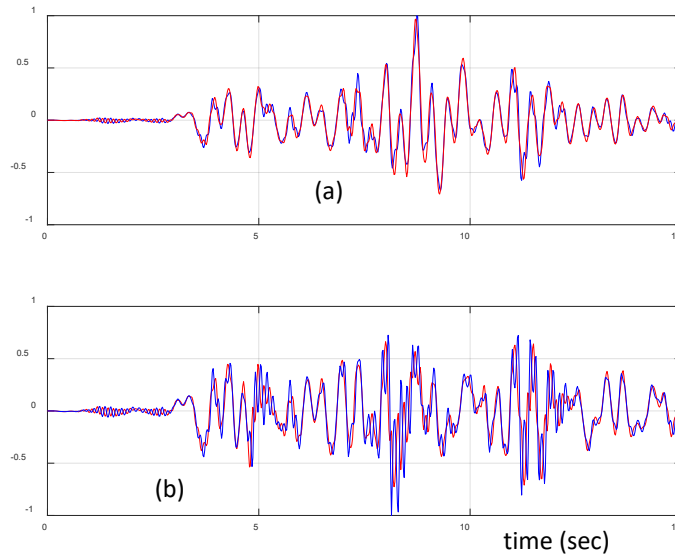

Figure 1. Normalized acceleration on the 7th level of an 8-story structure; reconstructed (in red) and exact result (in blue) for two conditions a) linear response and b) nonlinear response (max story ductility around 3)

Summary of IDNB

- Use a part of the data where (quasi) linear response can be anticipated and some system identification approach to estimate the frequency and damping of the first mode (real part of the first pole) (see *Technical Note*)
- Define the mass proportional damping matrix for small response amplitudes using the above results.
- Select an interpolation scheme and reconstruct the response at unmeasured levels.
- Use the pattern of story weights (actual values not needed) to compute an estimate for the history of the inertial base shear, $V_I(t)$
- Use the mass proportional damping matrix to compute the derivative of the constant damping base shear $\dot{V}_D(t)$ as $r^T C_o \ddot{u}$, where $\ddot{u}$ are the relative accelerations
- Differentiate $V_I(t)$ numerically.
- Compute $\dot{V}_R(t) = \dot{V}_I(t) + \bar{\rho}\dot{V}_D(t)$ for values of $\bar{\rho}$ covering some selected range, e.g., $-0.1 \leq \bar{\rho} \leq 1.5$
- Sort $|\dot{V}_R(t)|$ in ascending and decide on $\tilde{t}$.

- Plot the norm of the signal of the previous bullet vs $\bar{\rho}$ and identify the minimum. If the minimum occurs at values of $\bar{\rho}$ that are notably larger than 1 the constraint of Eq.10 is not satisfied and the information on inherent damping during nonlinearity cannot be extracted using IDNB.

Technical Note: Although the response before the strong motion has the damping of the reference state, this segment is just a few seconds long and thus too short to perform a reliable identification. One can use the segment that follows the strong motion, which is typically much longer but must then keep in mind that in this case the $\bar{\rho}$ from IDNB refers to a scaling of the damping that prevails after the strong motion. Although the "late response" linear damping is the same as the one at the outset in common nonlinear models, this is unlikely to be the case in real buildings, especially in the case of concrete. What we've done on this account when IDNB is applied is to take the reference damping as that obtained using the shortest signal (starting at t = 0) for which the first pole appears in the identification, provided this signal does not have a significant fraction in the strong motion region. When the signal that starts at the origin proves too long, we compute the reference damping using the linear response that follows the strong motion.

Validation

To get a sense of what is the best attainable performance we consider the situation where accelerations are available at every level and the damping matrix for small amplitude response is known. For conciseness we limit the examination to an 8-story shear building with a symmetrical plan and consider two ground motions, both recorded during the Northridge earthquake. The masses, story stiffness, and the yield levels are: m=14(1,1,1,1,1,1,1,1), k=1.91e4{1,1,1,0.7,0.7,0.7,0.5,0.5} and V_y =800{1,1,1,0.9,0.9,0.7,0.7} in units of kips, ft and secs, with the periods of the first 3 modes = {1.0, 0.368,0.232} secs. The simulations are carried out for 4 alternative inherent damping models, namely: a) Constant b) CSMIPκ ($\kappa = 4$) c) Lanzi and Luco and d) Rayleigh with tangent stiffness. The goal is to determine if application of the scheme allows correct identification of models with hysteretic coupling and constant damping.

Ground Motion #1

Ground motion #1 is the record from channel #3 of CSMIP station 24436 during the 17 June 1994, Northridge Earthquake, a station that is located at the Tarzana Cedar Hill Nursery. The record itself, and the shear force vs drift relation for the first story of the model, computed under the premise that the damping is 5% in every mode and uncoupled from hysteresis, are depicted in Fig.2.
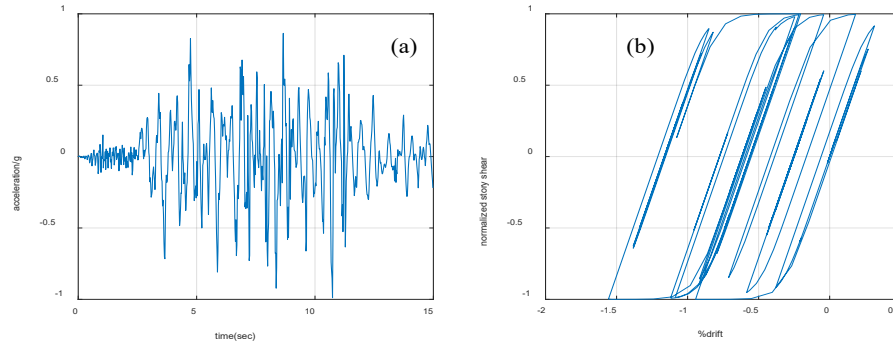
Figure 2. a) ground motion #1 b) first floor shear force drift response.

As can be seen, the inelasticity is significant, with a displacement ductility in the first level slightly larger than 3. The shear force vs drift relationship, as shown in (b), follows a Bouc-Wen model. Fig 3 shows the results from application of IDNB.
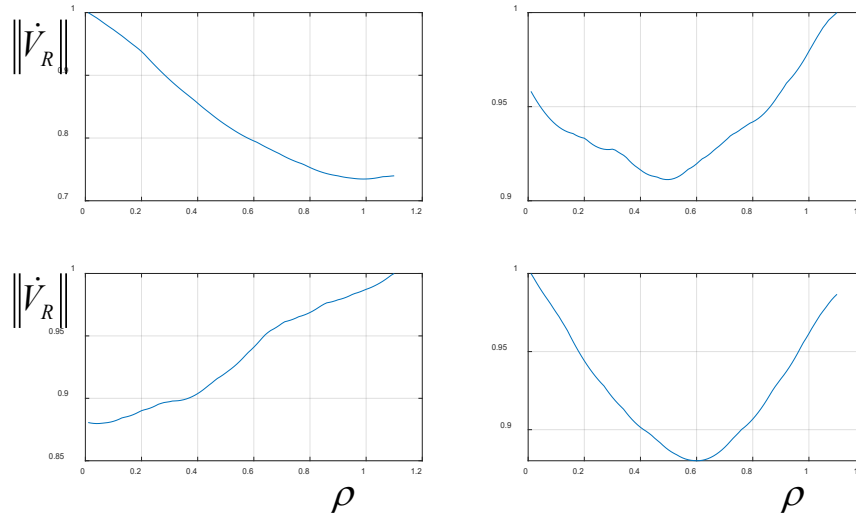

Figure 3. $\left\|\dot{V}_R\right\|$ (normalized) for $\tilde{t} = 1.5sec$ ($\Delta t = 0.02sec$) vs ρ for a) constant damping b) $CSMIP\kappa$ with $\kappa = 4$ c) Lanzi and Luco d) Rayleigh damping with tangent stiffness (5% in every mode).

As can be seen, the minimum in Fig.3a is reached in the vicinity of 1, correctly pointing to the fact that in this instance the damping matrix is constant. The results in (b) depicts a minimum at around 0.5, which gives an idea of how a nonlinearity with the extent shown in Fig.2 is mapped to $\bar{\rho}$ by the CSMIPκ model with κ =4. For the damping model proposed by Lanzi and Luco the minimum takes place very near zero, suggesting that this model produces large reductions in the inherent damping during the nonlinearity and finally in (d) which shows the result for the Rayleigh model with tangent stiffness, the minimum is only slightly to the left of the result for $CSMIP\kappa$ wit $\kappa = 4$. suggesting that these two models, at least in this example, produce comparable reductions.

Ground Motion #2

We consider the same recording station but use the horizontal record orthogonal to the previous one, which now corresponds to channel 1. The plot of the motion and the shear vs drift relation, which are depicted in Fig.4, show that the extent of inelasticity is somewhat larger than for motion #1. The maximum response ductility reaching a value slightly over 4.
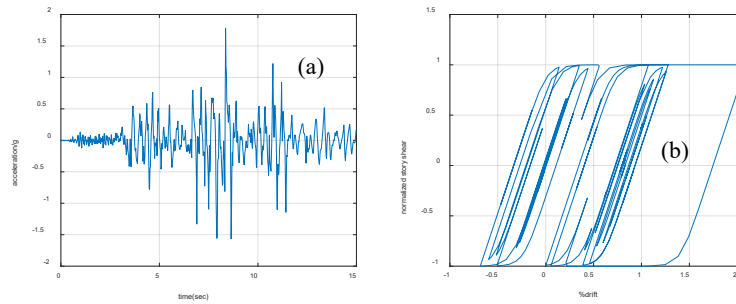

Figure 4. a) ground motion #2 b) first floor shear force drift response.

Instead of repeating the same cases as in Fig.3, we examine results obtained for data generated using the $CSMIP\kappa$ model with different values of κ, namely: 0,2,4 and 6. For $\kappa = 0$ the damping is constant and for the others the location of $\bar{\rho}$ is expected to shift progressively to the left. The results in Fig.5 confirm these expectations.
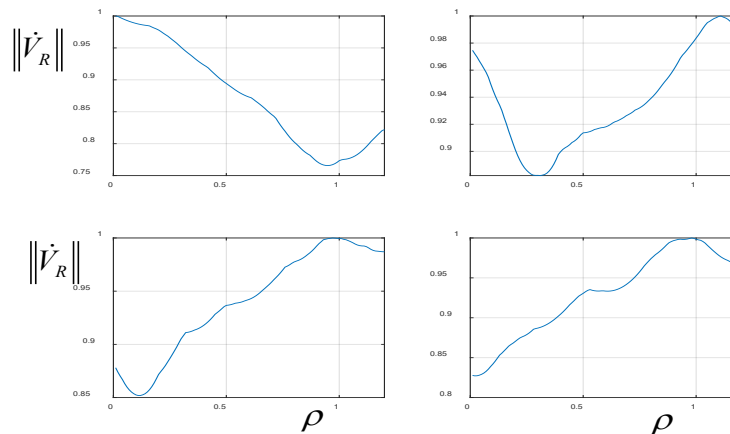

Figure 5. Normalized $\left\|\dot{V}_R\right\|$ for $\bar{t} = 1.5sec$ vs , responses from $CSMIP\kappa$ a-d) $\kappa = 0,2,4,6,$ respectively.

IDNB on Real Building Data

CSMIP station 12299

The sensor deployment is depicted in Fig.6. The largest structural response at this station, 0.62g, is for the Palm Spring earthquake of 1986 and we thus choose this record for examination. We select channels {13,12,11,10} in the N-S direction for examination. From inspection of the time history of the excitation the strong is taken to span from time step 100 to 550. System identification showed that (the negative) of the real part of the 1st pole is 0.29. The sampling frequency is 50 Hz.
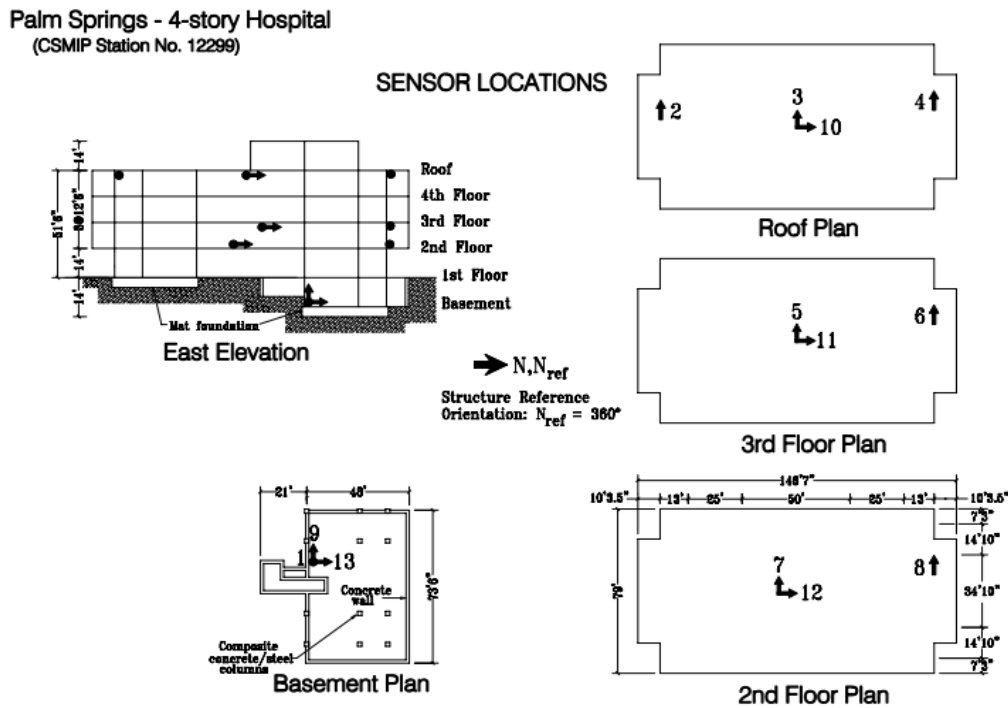

Figure 6. Sensor layout at station 12299

The *rhs* of Eq.7 (normalized) are depicted in Fig.7. The results, as can be seen, are reasonably consistent and point to a reduction in the effectiveness of inherent damping on the order of 50%
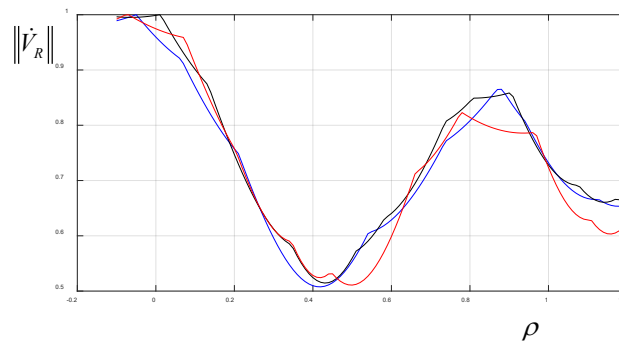

Figure 7. Normalized $\left\|\dot{V}_R\right\|$ for $\tilde{t}$=7,8 and 9 Δt.

CSMIP Station 14606

The sensor deployment is depicted in Fig.8. The largest structural response at this station, 0.49g, is for the Northridge earthquake and we chose the response of channels [3,5,8,11] for examination. From inspection of the time history of the input we take the strong motion to span from time step 1200 to 3189. System identification shows that (the negative) of the real part of the 1st pole is 0.447. The sampling frequency is 100 Hz.
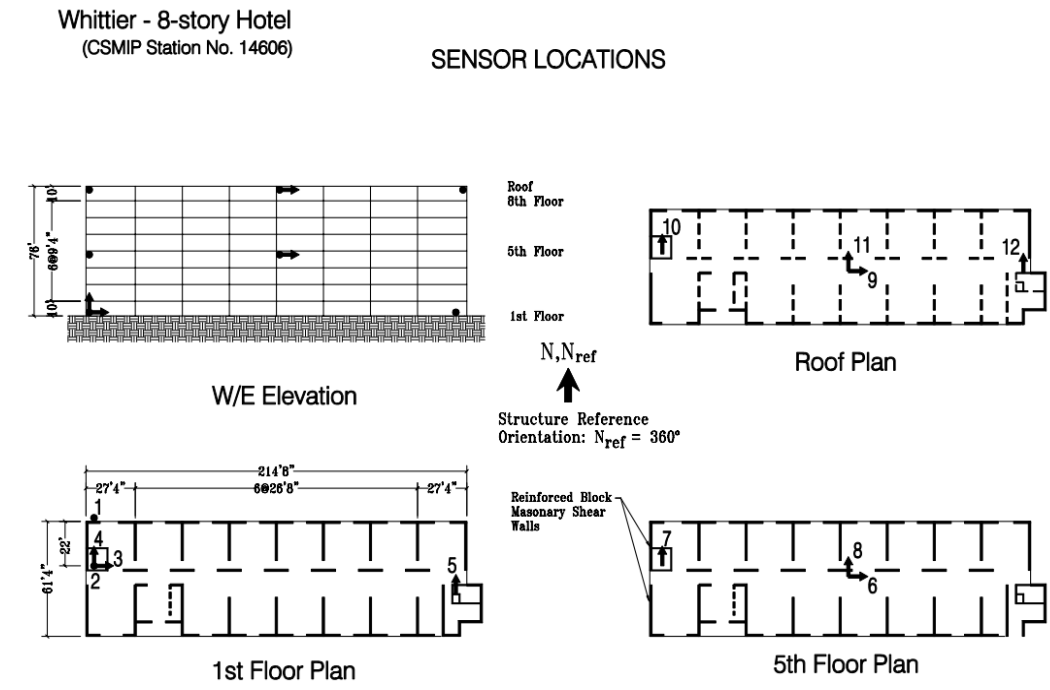

Figure 8. Sensor layout at station 14606

The *rhs* of Eq.7 (normalized) is depicted in Fig.9 for three assumed "yielding" durations. The result, again, is reasonably consistent and point to a reduction in the effectiveness of inherent damping on the order of 60%
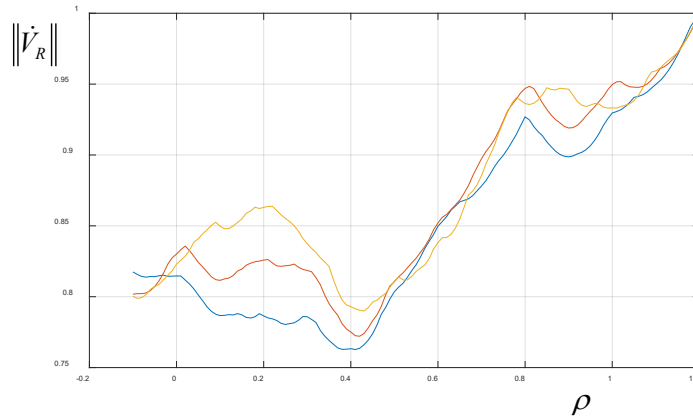
Figure 9. Normalized $\left\|\dot{V}_R\right\|$ for $\tilde{t}$=40, 45 and 50 Δt

CSMIP station 24322

The sensor deployment is depicted in Fig.10. The largest structural response at this station, 0.90g, is for the Northridge earthquake and we chose the response to this input for examination. We select the N-S direction and take the input motion (given the rigid basement) as the measurement at the ground floor. The channels used are {11,8,5,2} and we take the strong motion from time step 80 to 570. System identification gives (the negative) of the real part of the 1st pole as 0.091. The sampling frequency is 50 Hz.

Figure 10. Sensor layout at station 24322.

In this case the results for the scaling constant, as shown in Fig.11, consistently point to a minimum that is reached at a scaling larger than one, indicating (or presumably indicating) that the constraint of Eq.10 is not satisfied. In this case the IDNB interrogation does not hold.

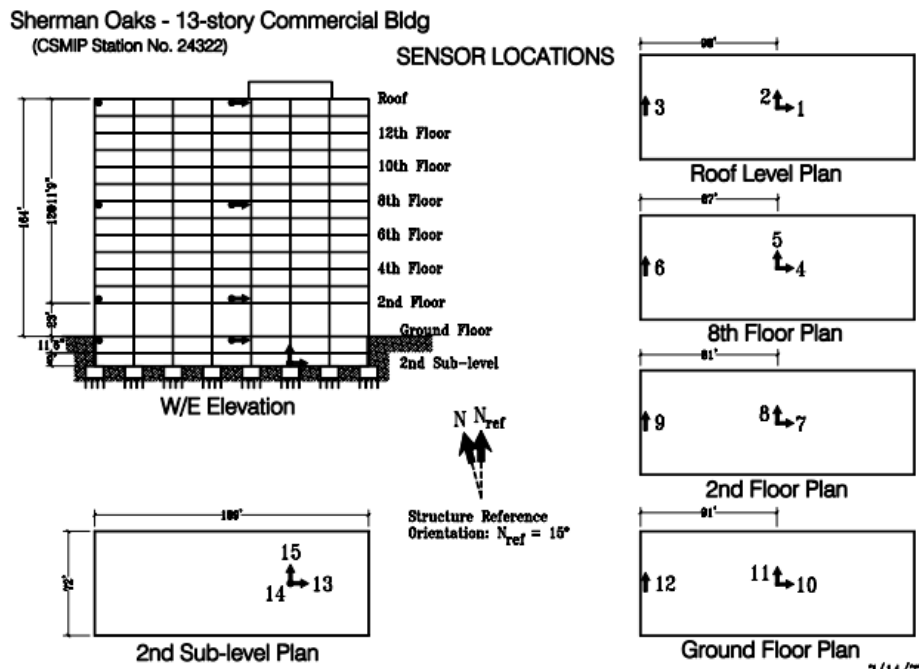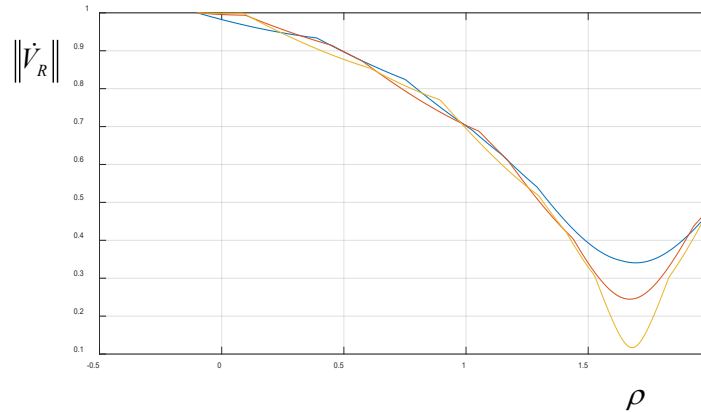**Figure 11.** Normalized $\left\|\dot{V}_R\right\|$ for $\tilde{t}$=6,8 and 10 Δt.

Concluding Observations

The IDNB scheme attempts to extract information on the behavior of inherent damping during nonlinear excursions by assuming that the rate of change of the base shear during some of these excursions is small enough to be discarded in equilibrium considerations. Since the foregoing assumption is not guaranteed satisfied the approach does not hold for all nonlinear data sets but this is not an important impediment since the goal is not to make assertions about particular structures, but to test which of the two propositions: a) constant pseudo-viscosity or b) some coupling with hysteresis, is the more plausible one. The results thus far suggest that the effectiveness of the inherent damping model may in fact decrease when hysteresis sets in, but it's important to stress that the reliability of this observation is conditional on the validation of IDNB which, at this point, has only been done for responses from shear building models with Bouc-When hysteresis without hardening. Work to determine the reliability of the scheme when the response signals come from more complex nonlinear models is currently ongoing.

References

[1]. Chopra, Anil K., and Frank McKenna. "Modeling viscous damping in nonlinear response history analysis of buildings for earthquake excitation." Earthquake Engineering & Structural Dynamics 45.2 (2016): 193-211.

[2]. Priestley, M. J. N., and D. N. Grant. "Viscous damping in seismic design and analysis." Journal of earthquake engineering 9.spec02 (2005): 229-255.

[3]. Jehel, Pierre, Pierre Léger, and Adnan Ibrahimbegovic. "Initial versus tangent stiffness-based Rayleigh damping in inelastic time history seismic analyses." Earthquake Engineering & Structural Dynamics 43.3 (2014): 467-484.

[4]. Smyrou, Eleni, M. J. Priestley, and Athol J. Carr. "Modelling of elastic damping in nonlinear time-history analyses of cantilever RC walls." Bulletin of Earthquake Engineering 9.5 (2011): 1559-1578.

[5]. Hall, John F. "Problems encountered from the use (or misuse) of Rayleigh damping." Earthquake engineering & structural dynamics 35.5 (2006): 525-545.

[6]. Luco, J. Enrique, and Armando Lanzi. "A new inherent damping model for inelastic time-history analyses." Earthquake Engineering & Structural Dynamics 46.12 (2017): 1919-1939.

[7]. Salehi, Mohammad, and Petros Sideris. "Enhanced Rayleigh damping model for dynamic analysis of inelastic structures." Journal of Structural Engineering 146.10 (2020): 04020216.

[8]. Caughey, T. K. (1960a). "Classical normal modes in damped linear dynamic systems." J. Appl. Mech., 27(2), 269–271.

[9]. Bernal, Dionisio. "Viscous damping in inelastic structural response." Journal of Structural Engineering 120.4 (1994): 1240-1254.

[10]. Lanzi, Armando, and J. Enrique Luco. "Elastic velocity damping model for inelastic structures." Journal of Structural Engineering 144.6 (2018): 04018065.

[11]. Bernal D., and A. Nasseri. "An approach for response reconstruction in seismic applications", Proceedings of the 3rd International Operational Modal Analysis Conference IOMAC09, Ancona Italy May 4-6 2009.

[12]. Bernal, D., and A. Nasseri. "Schemes for reconstructing the seismic response of instrumented buildings." SMIP09 Seminar on Utilization of Strong-Motion Data. 2009.

VALIDATION OF SEISMIC DESIGN PROVISIONS FOR DIAPHRAGMS AND ASSESSMENT OF HIGHER-MODE RESPONSES ON EARTHQUAKE-RESISTANT BUILDINGS – SECOND PROJECT UPDATE

C. Franco Mayorga and Georgios Tsampras

Department of Structural Engineering
University of California San Diego

Abstract

This paper disseminates the ongoing research conducted for the assessment of the Alternative Design Provisions for Diaphragms in buildings per ASCE/SEI 7-22 Section 12.10.3 by utilizing recorded strong-motion acceleration data. Details of the workflow developed for the assessment of the design provisions are presented.

Introduction

Floor diaphragms and their connections to the vertical elements of the seismic force-resisting systems (SFRS) are critical components of earthquake-resistant buildings. Underestimating the level of seismic-induced horizontal forces to which the diaphragms are subjected could be catastrophic. The loss of the ability of the connections of diaphragms to transfer forces to the SFRS could lead to local collapse of the floor or complete collapse of the building. Diaphragm collapses were observed after the Northridge earthquake due to the loss of connections between floor diaphragms and the vertical elements of precast concrete buildings and the vertical elements of tilt-up-wall buildings (Fleischman et al. (2013), Iverson and Hawkins (1994), Tilt-up-Wall Buildings (1996)). After the 2010-2011 Christchurch earthquakes, excessive damage and collapse of floor diaphragms were attributed to inadequate integrity of the load path, underestimation of seismic-induced horizontal forces, and poorly understood interactions between floor diaphragms and walls, supporting beams, and reinforced concrete (RC) moment frames (Gonzalez et al. (2017), Scarry (2014), Kam et al. (2011)). The complex interactions between diaphragms and other structural elements result in unpredictable seismic responses of buildings which often lead to damage to structural members that are designed to remain undamaged (Kam et al. (2011), Bull (2004), Wallace et al. (2012), Henry et al. (2017)).

Earthquake numerical simulations of buildings have shown that the seismic-induced horizontal forces in floor diaphragms can be large relative to the strength of the floor diaphragms. These excessive forces can lead to an inelastic and potentially non-ductile response of the diaphragms (Fleischman and Farrow (2001)). The contribution of the second and higher-mode responses to the total dynamic response of buildings (termed higher-mode effects) may contribute to the excessive forces and floor total accelerations (Sewell et al. (1986), Chopra (2007)). It has been shown that high floor accelerations due to the higher-mode effects can be expected in buildings with SFRS that develop a flexural yield mechanism at the base, such as flexural-dominant RC structural walls (Chopra (2007), Priestley and Amaris (2002), Wiebe sand

Christopoulos (2009), Panagiotou and Restrepo (2009), Tsampras et al. (2016)).

The Alternative Design Provisions for Diaphragms per ASCE/SEI 7-22 (2021) Section 12.10.3 provides estimates of the seismic-induced horizontal forces that can be used to design floor diaphragms. These force estimates were developed based on analysis of experimental data from shaking table tests (Panagiotou et al. (2011), Chen et al. (2016)) and earthquake numerical simulations (Choi et al. (2008), Fleischman (2013)). These force estimates consider the higher-mode effects. Thus, it is expected that they should result in more accurate estimates of the seismic-induced horizontal forces for the design of floor diaphragms.

The California Strong Motion Instrumentation Program (CSMIP) funds projects that utilize recorded acceleration response data to validate the seismic design provisions. In response to the Request for Proposal No. 1020-005 in 2020, Tsampras submitted a proposal that aimed to validate the seismic design provisions for diaphragms and assess the higher-mode responses on earthquake-resistant buildings by utilizing strong-motion acceleration data available in the Center for Engineering Strong Motion Data (CESMD). In 2022, CSMIP awarded a grant, and Tsampras and Mayorga initiated their research toward assessing the design provisions. Mayorga and Tsampras (2022) presented their first progress report during the 2022 Strong Motion Instrumentation Seminar (SMIP). More specifically, the authors focused on the estimation of the location of the center of rigidity from the recorded response data and the comparison between the peak floor accelerations at the estimated center of rigidity and the design acceleration coefficients computed using the equations in ASCE/SEI 7-22 Section 12.10.3.

The preliminary analysis showed that most of the building stations have not been subjected to ground motions with intensities comparable to the design-level earthquake intensity since they were instrumented. In support of this statement, Figure 1 shows the ratios of the peak floor accelerations PFA_x over the design acceleration coefficients C_{px} at three different locations over the height of multiple building stations (i.e., $h_x/h_n = 0.4, 0.8,$ and 1.0) with respect to the ratios of the ground motion spectral accelerations at the first-mode period $S_a(T_1, h_x/h_n = 0.0) = S_a(T_1)$ over the design spectral accelerations at the first-mode period $S_{ad}(T_1)$. The figure shows that most of the seismic events resulted in ratios $S_a(T_1)/S_{ad}(T_1)$ below 0.5. The results shown in Figure 1 indicate a lack of recorded acceleration response data from seismic events that result in spectral demands close to the design-level earthquake spectral demand. This introduces two challenges. The first challenge is that the acceleration coefficients need to be at the earthquake intensity of the recorded ground motions to compare them with the peak floor accelerations recorded at the building stations. The second challenge is that the inelastic response of the building stations subjected to the recorded ground motions is limited, therefore, the values of the redaction factor R and overstrength factor Ω_0 need to be adjusted according to the level of inelastic response at which the building stations were subjected. The ongoing research presented in this paper shows how these challenges can be addressed.
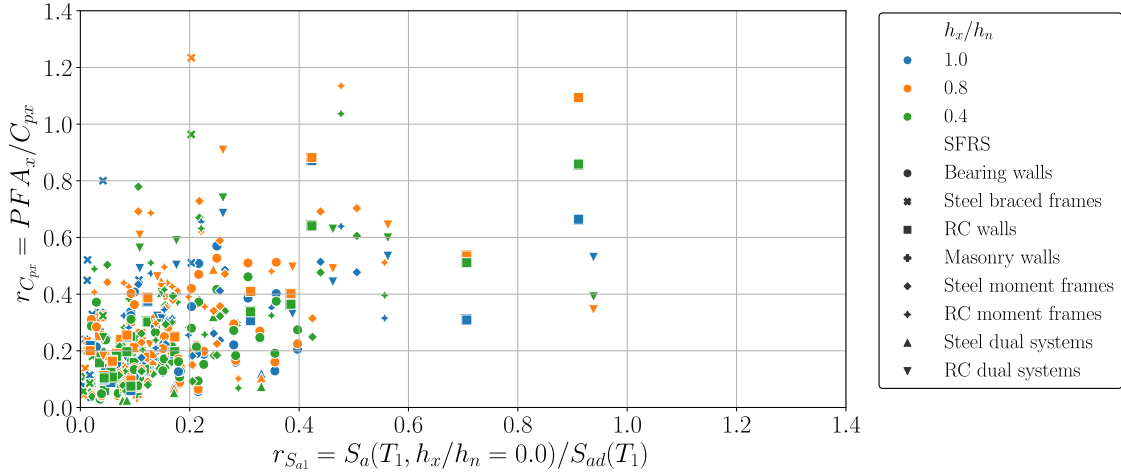
Figure 1. Ratio of the peak floor accelerations over design acceleration coefficients at three different locations over the height of the building stations subjected to various seismic events with respect to the ratio of the ground motion spectral acceleration over the design spectral acceleration at the first-mode period

The objective of this paper is to disseminate the ongoing research toward the validation of the seismic design provisions for diaphragms and assessment of the higher-mode responses on earthquake-resistant buildings by utilizing strong motion acceleration data available in the CESMD. This paper presents a summary of the equations used to compute the design acceleration coefficients per ASCE/SEI 7-22 Section 12.10.3, a workflow including the calculations required for the assessment of the design provisions, estimates of the first-, second-, and third-mode periods, estimates of the seismic performance factors R and Ω_0 based on the peak roof drift obtained from the recorded response data, four scaling approaches for the design acceleration coefficients, and a comparison between the design-based modified acceleration coefficients and the measured peak floor accelerations over the height of the buildings.

Data and metadata from a larger number of building stations are considered in this paper compared to the building stations considered by Mayorga and Tsampras (2022). Buildings within the California Geological Survey Network (CE) that have been subjected to peak floor accelerations larger than 0.2g without restriction on the number of stories are considered in this analysis.

ASCE/SEI 7-22 Section 12.10.3 Alternative Design Provisions for Diaphragms

In-plane seismic design forces for diaphragms, including chords, collectors, and their connections to the vertical elements are given in Section 12.10.3 Alternative Design Provisions for Diaphragms of the ASCE/SEI 7-22. The in-plane seismic design forces are defined as

$$F_{px} = \frac{C_{px}}{R_s} w_{px} \geq 0.2\, S_{DS} I_e w_{px} \tag{1}$$

where C_{px} is the design acceleration coefficient at level x, w_{px} is the weight tributary to the diaphragm at level x, R_s is the diaphragm design force reduction factor, S_{DS} is the design, 5% damped, spectral response acceleration parameter at short periods, and I_e is the building

importance factor. The distribution of design acceleration coefficients over the normalized building height is presented in Figure 2. In this figure, N is the number of stories above the base, h_x is the height above the base to the level x, h_n is the vertical distance from the base to the highest level of the SFRS of the structure, and C_{p0} is the diaphragm acceleration coefficient at the base. C_{p0} is computed as

$$C_{p0} = 0.4S_{DS}I_e \tag{2}$$

C_{pi} is the diaphragm design acceleration coefficient at 80% of h_n calculated as

$$C_{pi} = \max{(0.8C_{p0}, 0.9\Gamma_{m1}\Omega_0 C_s)} \tag{3}$$

where $\Gamma_{m1} = 1 + z_s(1 - 1/N)/2$ is the first modal contribution factor, Ω_0 is the overstrength factor, and C_s is the seismic response coefficient in accordance with Section 12.8.1.1 of the ASCE/SEI 7-22. The term C_{pn} is the diaphragm design acceleration coefficient at h_n computed as

$$C_{pn} = \sqrt{(\Gamma_{m1}\Omega_0 C_s)^2 + (\Gamma_{m2}C_{s2})^2} \geq C_{pi} \tag{4}$$

where

$$C_{s2} = \begin{cases} \min{\left(\frac{I_e S_{D1}}{0.03(N-1)}, (0.15N + 0.25)I_e S_{DS}, I_e S_{DS}\right)}, & N \geq 2 \\ 0 & , N = 1 \end{cases} \tag{5}$$

is the higher-mode seismic response coefficient and $\Gamma_{m2} = 0.9z_s(1 - 1/N)^2$. N was previously defined and z_s is the mode shape factor defined in Section 12.10.3.2.1 of the ASCE/SEI 7-22.
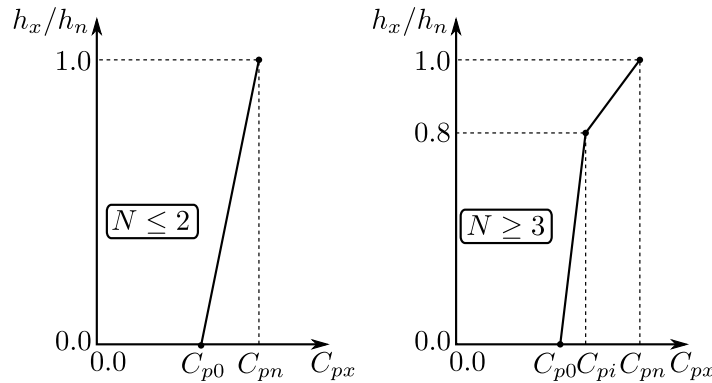

Figure 2. Calculation of the design acceleration coefficients in buildings with $N \leq 2$ and in buildings with $N \geq 3$ (Figure 12.10-2 in ASCE/SEI 7-22)

Equation (5) considers that the periods of the higher modes probably lie on the ascending, constant, or first descending branch of the two-period design response spectrum given by ASCE/SEI 7-22.

Workflow for Analysis of Recorded Data and Metadata

A workflow for the analysis of the recorded data and metadata to assess the seismic design provisions for diaphragms has been developed using the open-source programming language Python (Van Rossum and Drake (2009)). This workflow allows us to analyze data and metadata available in the CESMD along with metadata that we have generated and appended to the existing datasets. Seventy-seven combinations of building stations and seismic events have been analyzed using the workflow.

The workflow in its current form is executed in sixteen steps. Figure 3 shows a schematic representation of these steps with application to one example building station. Each step in the analysis workflow shown in the figure is summarized as follows:

- Step 1: The data and metadata are loaded into the workflow. The loaded database includes information available on the CESMD database along with information that has been manually extracted from drawings and other sources available for the building stations, their sites, and seismic events.
- Step 2: For the analysis of a specific building station under the selected seismic events indicated in the information incorporated in Step 1, the analyst selects the building station of interest. Analysis of the data and metadata of all building stations loaded in Step 1 can be performed as well.
- Step 3: A database is created within Python using Pandas DataFrames (type of database variable in Python).
- Step 4: The recorded accelerations for each channel are plotted and saved for checking purposes.
- Step 5: The peak recorded accelerations for each channel are computed and plotted over the height of the building station for checking purposes.
- Step 6: The location of the center of rigidity at each sufficiently instrumented floor is estimated using the method proposed by Şafak and Çelebi (1990) along with the utilization of the recorded acceleration data (Mayorga and Tsampras (2022)). Plots of the coherence area, a measure of the correlation between the translational and torsional responses, with respect to the estimated position of the center of rigidity in the floor plan are provided for the selected seismic events. If multiple seismic events are available, the potential shift of the estimated location of the center of rigidity can be computed from the derived data.
- Step 7: The estimation of the center of rigidity using recorded data allows the decomposition of the floor displacement, velocity, and acceleration data to horizontal translational and torsional floor displacements, velocities, and accelerations. The accuracy of the estimation of the location of the center of rigidity determines the accuracy of the decomposition of the translational and torsional components of the recorded floor displacements, velocities, and accelerations.
- Step 8: The spectral accelerations at instrumented floors are computed for the selected seismic events. The results are compared with the metadata already available in the CESMD for checking purposes.
- Step 9: The first-mode translational periods in the two directions of the building station are estimated considering the SFRS (based on metadata added manually in the expanded database), the building height, and the peak ground velocity using the empirical equations

derived by Xiang at al. (2016). See Section "Estimation of First-, Second- and Third-mode Periods".

- <u>Step 10</u>: The second- and third-mode translational periods are computed based on the estimated first-mode period using the analytical equations derived by Miranda and Taghavi (2005). See Section "Estimation of First-, Second- and Third-mode Periods".
- <u>Step 11</u>: The design spectrum for the specific building station is computed along with the design spectral accelerations and ground motion spectral accelerations at first-, second-, and third-mode translational periods of the building station in two horizontal directions. The ratio of the ground spectral acceleration over the design spectral accelerations at each period is also computed and stored in the expanded database as additional metadata.
- <u>Step 12</u>: The design acceleration coefficients for the two translational directions of the building station are computed using the design equations per ASCE/SEI 7-22 Section 12.10.3. The design acceleration coefficients are also computed using the design equations per ASCE/SEI 7-22 Section 12.10.1. for comparison purposes.
- <u>Step 13</u>: The distribution of the translational components of the recorded peak floor accelerations over the height of the building station is compared with the distribution of the design acceleration coefficients over the height of the building station.
- <u>Step 14</u>: R and Ω_0 at the earthquake intensity of the measured ground motions are estimated based on the peak roof drift at the center of rigidity computed using the displacement time-histories given in the CESMD dataset. See Section "Estimation of Seismic Performance Factors".
- <u>Step 15</u>: The design acceleration coefficients are scaled to the measured (recorded) earthquake intensity using four scaling approaches. See Section "Design-based Modified Acceleration Coefficients".
- <u>Step 16</u>: Metrics to quantify the difference in magnitude and distribution over the building height of the design-based modified acceleration coefficients and the peak floor accelerations are computed. See Section "Preliminary Comparison between Scaled Acceleration Coefficients and Measured Peak Floor Accelerations".

Buildings Stations

A set of seventy-seven instrumented buildings that are part of the CSMIP were selected to compare their peak floor accelerations to the design acceleration coefficients. The building stations considered in this analysis belong to the California Geological Survey Network (CE). They have various numbers of stories, mostly below 20 stories. They were designed for risk categories II or IV. Their foundation soils were classified as B, C, or D. They have been subjected to ground motions that resulted in recorded peak floor accelerations larger than 0.2g since they were instrumented.
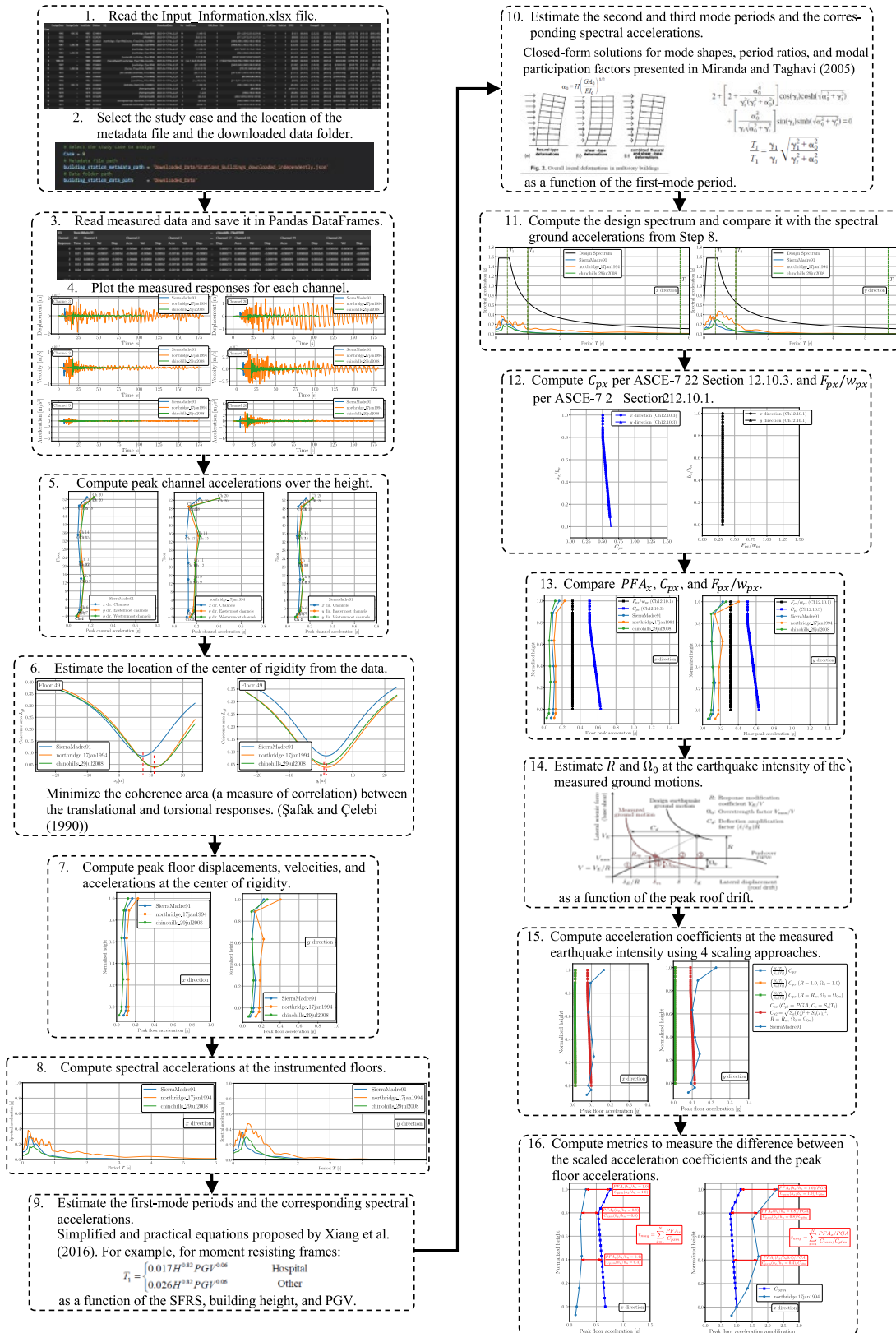
1. Read the Input_Information.xlsx file.

2. Select the study case and the location of the metadata file and the downloaded data folder.

3. Read measured data and save it in Pandas DataFrames.

4. Plot the measured responses for each channel.

5. Compute peak channel accelerations over the height.

6. Estimate the location of the center of rigidity from the data.

Minimize the coherence area (a measure of correlation) between the translational and torsional responses. (Şafak and Çelebi (1990))

7. Compute peak floor displacements, velocities, and accelerations at the center of rigidity.

8. Compute spectral accelerations at the instrumented floors.

9. Estimate the first-mode periods and the corresponding spectral accelerations.
Simplified and practical equations proposed by Xiang et al. (2016). For example, for moment resisting frames:

$$T_1 = \begin{cases} 0.017 H^{0.82} PGV^{0.06} & \text{Hospital} \\ 0.026 H^{0.82} PGV^{0.06} & \text{Other} \end{cases}$$

as a function of the SFRS, building height, and PGV.

10. Estimate the second and third mode periods and the corresponding spectral accelerations.
Closed-form solutions for mode shapes, period ratios, and modal participation factors presented in Miranda and Taghavi (2005)

as a function of the first-mode period.

11. Compute the design spectrum and compare it with the spectral ground accelerations from Step 8.

12. Compute C_{px} per ASCE-7 22 Section 12.10.3. and F_{px}/w_{px} per ASCE-7 2 Section212.10.1.

13. Compare PFA_x, C_{px}, and F_{px}/w_{px}.

14. Estimate R and Ω_0 at the earthquake intensity of the measured ground motions.

as a function of the peak roof drift.

15. Compute acceleration coefficients at the measured earthquake intensity using 4 scaling approaches.

16. Compute metrics to measure the difference between the scaled acceleration coefficients and the peak floor accelerations.

Figure 3. Schematic representation of the workflow and application to one example building station

Forty-three cases of analysis, each of which corresponds to one building station and one or more seismic events, are considered. Table 1 lists the station of measurement, recorded seismic events, design date, design code, number of stories, building risk category, site class, spectral response acceleration parameter at short periods S_s, and spectral response acceleration parameter at a period of 1 [s] S_1 for each analysis case. These spectral response acceleration parameters are obtained based on the building location in terms of latitude and longitude given on the CESMD website https://www.strongmotioncenter.org/ and the risk category defined in terms of the building use or occupancy.

Table 1. Analysis case, station of measurement, recorded seismic event, design date, design code, number of stories, building risk category, site class, spectral response acceleration parameter at short periods S_s, and spectral response acceleration parameter at a period of 1 [s] S_1

Case	Station	Recorded seismic events	Design date	Design code**	Number of stories*	Risk Category	Site Class	S_s[g] *****	S_1[g] *****
1	CE14654	Northridge (1994)	1985	UBC-82	14	II	D	1.851	0.652
2	CE24236	Whittier (1987)	1925	--	14	II	D	2.092	0.750
3	CE24322 ***	Northridge (1994), Encino (2014)	1964	--	13	II	D	1.962	0.700
4	CE24464	Northridge (1994)	1967	LABC-66	20	II	C	2.082	0.747
5	CE24566	Northridge (1994)	1971	--	12	II	C	2.090	0.762
6	CE24569	Northridge (1994)	1961	LABC-60	15	II	C	1.993	0.710
7	CE24601	Landers (1992), Northridge (1994)	1980	--	17	II	C	1.978	0.705
8	CE24602	Sierra Madre (1991), Northridge (1994), Chino Hills (2008)	1988-90	--	52	II	C	1.967	0.700
9	CE24643	Northridge (1994)	1967	--	19	II	D	2.082	0.744
10	CE24680	Encino (2014)	1965	LABC-64	14	II	D	2.270	0.720
11	CE57357 ****	Mt. Lewis (1986), Loma Prieta (1989)	1972	--	13	II	D	1.530	0.523
12	CE58480	Loma Prieta (1989)	1964	--	18	II	D	1.500	0.600
13	CE58483	Loma Prieta (1989)	1964	--	24	II	C	1.802	0.686
14	CE58639	Berkeley (2018)	1975	UBC-73	13	II	D	1.865	0.711
15	CE12266	Palm Springs (1986)	1970	--	1	II	D	2.122	0.856
16	CE12284	Palm Springs (1986)	1974	--	4	II	D	1.500	0.610
17	CE12299	Palm Springs (1986)	1967	--	4	IV	D	1.814	0.754
18	CE13213	Borrego Springs (2010)	1994	--	3	IV	D	1.773	0.694
19	CE13589	Landers (1992), Northridge (1994)	1971	--	10	IV	D	1.384	0.494
20	CE14311	Whittier (1987)	1968	--	5	II	D	1.546	0.556
21	CE14606	Northridge (1994), Chino Hills (2008), Whittier Narrows (2010)	1984	UBC-83	8	II	D	1.842	0.657
22	CE23285	Landers (1992), Northridge (1994)	1968	--	5	II	D	2.384	1.014
23	CE23287	Landers (1992), Northridge (1994), San Bernardino (2009), Borrego Springs (2010)	1970	--	6	II	D	2.438	0.977
24	CE23495	Palm Springs (1986), Landers (1992), Big Bear (1992), Cabazon (2018), ci38457511 (2019)	1971	--	1	II	D	1.890	0.744

Case	Station	Recorded seismic events	Design date	Design code**	Number of stories*	Risk Category	Site Class	S_s[g] *****	S_1[g] *****
25	CE23511	Chino Hills (2008)	1971	--	2	II	D	1.762	0.639
26	CE23516	Landers (1992)	1983	--	3	II	D	2.453	0.983
27	CE24385	Whittier (1987), Sierra Madre (1991), Northridge (1994)	1974	--	10	II	D	2.017	0.699
28	CE24386	Northridge (1994)	1965	--	7	II	D	2.115	0.712
29	CE24517	Landers (1992)	1974	--	3	II	D	1.500	0.600
30	CE24571	Sierra Madre (1991), Landers (1992)	1963	--	9	II	C	2.090	0.761
31	CE24571 ******	Northridge (1994)	1963	--	9	II	C	2.090	0.761
32	CE24609	Landers (1992), Northridge (1994), ci38443183 (2019), ci38457511 (2019)	1986	UBC-79	5	IV	D	1.500	0.600
33	CE57355	Morgan Hill (1984), Loma Prieta (1989), Alum Rom (2007)	1964	--	10	II	D	1.500	0.600
34	CE57356	Morgan Hill (1984), Loma Prieta (1989), Alum Rock (2007)	1971	--	10	II	D	1.500	0.600
35	CE58334	Piedmont (2007), Berkeley (2011), Piedmont (2015)	1973	--	3	II	B	2.161	0.834
36	CE13698	Lake Elsinore (2007), Chino Hills (2008)	1991	--	2	II	D	2.024	0.797
37	CE23634	Landers (1992), Big Bear (1992), Northridge (1994)	1991	--	5	IV	D	2.287	0.914
38	CE24104	Chatsworth (2007)	1983	--	2	IV	D	2.055	0.724
39	CE24248	ci38695658 (2020)	1986	--	9	IV	C	2.287	0.914
40	CE24370	Whittier (1987)	1976	--	6	II	D	2.023	0.694
41	CE24463	Whittier (1987), Northridge (1994)	1970	LABC-70	5	II	D	1.898	0.676
42	CE24514	Whittier (1987), Northridge (1994)	1976	--	6	IV	C	2.653	0.857
43	CE47459	Morgan Hill (1984), Loma Prieta (1989)	1948 & 1955	--	4	II	D	2.588	0.967

* Number of stories above the ground level
** Design code given in the building station websites. UBC: Uniform Building Code. LABC: Los Angeles Building Code.
*** The building was strengthened with friction dampers after the 1994 Northridge Earthquake.
**** 96 dampers were installed after the Loma Prieta Earthquake to reduce building movement.
***** S_s and S_1 are obtained based on the building location and Risk Category.
****** Building station CE24571 was divided into two analysis cases because the data from Channel 7 on the second floor was not found for the seismic events associated with the analysis case 30.

The SFRS for the analysis cases given in Table 1 are assumed based on the design date (and design code when available). Bearing walls, Steel braced frames, RC walls, Masonry walls, Steel moment frames, RC moment frames, Steel dual systems, and RC dual systems are considered. The dual systems are SFRS composed of a combination of walls or braced frames and moment frames where the moment frames can resist at least 25% of the prescribed seismic forces.

Table 2 lists the assumed SFRS, the corresponding response modification coefficient R, overstrength factor Ω_0, and the deflection amplification factor C_d. The seismic performance

factors R, Ω_0, and C_d are obtained from ASCE/SEI 7-22 Table 12.2-1.

Table 2. Assumed seismic force-resisting systems, response modification coefficients R, overstrength factors Ω_0, and deflection amplification factor C_d

Case	Assumed Seismic Force-resisting System (SFRS) in x and y directions*	Response modification coefficient R in x and y directions	Overstrength factor Ω_0 in x and y directions	Deflection amplification factor C_d in x and y directions
1	Steel dual systems	6.0	2.5	5.0
2	RC dual systems	5.5	2.5	4.5
3	RC moment frames	5.0	3.0	4.5
4	RC moment frames	5.0	3.0	4.5
5	Steel moment frames	4.5	3.0	4.0
6	Steel moment frames	4.5	3.0	4.0
7	Bearing walls	4.0	2.5	4.0
8	Steel braced frames	6.0	2.0	5.0
9	Steel moment frames, Steel braced frames	4.5, 6.0	3.0, 2.0	4.0, 5.0
10	RC dual systems	5.5	2.5	4.5
11	Steel moment frames	4.5	3.0	4.0
12	Steel moment frames	4.5	3.0	4.0
13	RC dual systems	5.5	2.5	4.5
14	Bearing walls	4.0	2.5	4.0
15	Bearing walls	1.5	2.5	1.5
16	RC walls	5.0	2.5	4.5
17	Steel moment frames	4.5	3.0	4.0
18	Steel moment frames	4.5	3.0	4.0
19	RC walls	5.0	2.5	4.5
20	Bearing walls	4.0	2.5	4.0
21	Bearing walls	3.5	2.5	2.25
22	RC walls	5.0	2.5	4.5
23	Bearing walls	4.0	2.5	4.0
24	Bearing walls	4.0	2.5	4.0
25	RC moment frames	5.0	3.0	4.5
26	Steel moment frames	4.5	3.0	4.0
27	RC dual systems	5.5	2.5	4.5
28	RC dual systems	5.5	2.5	4.5
29	Masonry walls	2.0	2.5	2.0
30	RC moment frames	5.0	3.0	4.5
31	RC moment frames	5.0	3.0	4.5
32	Steel moment frames	4.5	3.0	4.0
33	RC moment frames, RC walls	5.0	3.0, 2.5	4.5
34	Bearing walls	4.0	2.5	4.0
35	RC walls	5.0	2.5	4.5
36	Steel dual systems	6.0	2.5	5.0
37	Steel moment frames	4.5	3.0	4.0
38	Steel moment frames	4.5	3.0	4.0
39	Steel braced frames	8.0	2.0	4.0
40	Steel moment frames	4.5	3.0	4.0
41	RC moment frames	5.0	3.0	4.5
42	RC walls	5.0	2.5	4.5
43	RC walls	5.0	2.5	4.5

* The SFRS are assumed based on the definitions given in Table 12.2-1 of the ASCE/SEI 7-22.

Estimation of First-, Second-, and Third-mode Periods

The first-mode translational periods in the two directions of the building stations are estimated using the empirical equations proposed by Xiang et al. (2016). They identified the modal quantities (i.e., natural periods and equivalent viscous damping ratios) of ninety-four building stations using three time-domain and one frequency-domain system identification methods considering more than one thousand seismic records. They combined the results from these system identification methods to obtain unique values of the first-mode period and damping ratio for each combination of building station and seismic event. They proposed simplified and practical equations for the first-mode period and damping ratio in terms of structural system type, building height, and peak ground velocity. The equations are used to estimate the first-mode period for each combination of building station and seismic event listed in Table 1. The assumed SFRS given in Table 2, the building heights obtained from the building station websites, and the recorded peak ground velocities are considered as inputs for the equations proposed by Xiang et al. (2016).

The second- and third-mode periods are estimated using the analytical equations derived by Miranda and Taghavi (2005). They used a simplified model based on an equivalent continuum structure consisting of a combination of a flexural beam and a shear beam to approximate the dynamic characteristics of buildings. Assuming uniform distributions of mass and stiffness over the height of the building, they presented the following closed-form solution for the period ratios

$$\frac{T_i}{T_1} = \frac{\gamma_1}{\gamma_i} \sqrt{\frac{\gamma_1^2 + \alpha_0^2}{\gamma_i^2 + \alpha_0^2}} \tag{6}$$

where T_i is the ith-mode period, γ_i is the eigenvalue parameter associated with the ith-mode period, and α_0 is a nondimensional parameter that controls the degree of participation of the overall flexural and overall shear deformations to the total deformation in the simplified models of multistory buildings. γ_i is the ith-root of the characteristic equation

$$2 + \left[2 + \frac{\alpha_0^4}{\gamma_i^2(\gamma_i^2 + \alpha_0^2)}\right] cos(\gamma_i) \cosh\left(\sqrt{\gamma_i^2 + \alpha_0^2}\right) + \frac{\alpha_0^2}{\gamma_i\sqrt{\gamma_i^2 + \alpha_0^2}} sin(\gamma_i) \sinh\left(\sqrt{\gamma_i^2 + \alpha_0^2}\right) \tag{7}$$

and α_0 usually ranges from 0 to 1.5 for shear wall and braced frame buildings, from 1.5 to 5 for dual system buildings, and from 5 to 20 for moment-resisting frame buildings (Miranda and Reyes (2002)).

Equation (6) is used to estimate the second- and third-mode periods for each combination of building station and seismic event listed in Table 1. Values of α_0 equal to 0.75 for shear wall and braced frame buildings, 3.25 for dual system buildings, and 12.5 for moment-resisting frame buildings are assumed (Miranda and Reyes (2002), Taghavi and Miranda (2005)).

Estimation of Seismic Performance Factors

The definition of the seismic performance factors R and Ω_0 used to compute the design acceleration coefficients per ASCE/SEI 7-22 Section 12.10.3 assumes that buildings are subjected to a design-level earthquake intensity ground motion. Most of the building stations considered in this study were subjected to ground motions with an earthquake intensity lower than the design level. Thus, the acceleration coefficients must be computed using ASCE/SEI 7-22 considering R and Ω_0 values modified to account for the reduced intensity of ground motions. The computed acceleration coefficients can be compared with the recorded peak floor accelerations. This section presents a simplified and practical way to estimate R and Ω_0 based on the peak roof drift computed at the estimated center of rigidity as a measure of the level of inelastic response of the building.

The seismic performance factors are defined in terms of the global inelastic response of the SFRS idealized as the pushover curve presented in Figure 4. This figure is based on Figure 1-1 in FEMA P695 (2009), in which R, Ω_0, and C_d are represented as incremental differences despite they are dimensionless ratios of forces, accelerations, or displacements. In Figure 4, V_E represents the force that would be developed in the SFRS if the system remained entirely linear-elastic for the design-level earthquake ground motion. V_{max} represents the actual maximum strength of the fully yielded system, and V is the seismic base shear required for design. R and Ω_0 are defined as

$$R = \frac{V_E}{V} \tag{8}$$

and

$$\Omega_0 = \frac{V_{max}}{V} \tag{9}$$

, respectively. δ_E represents the roof drift of the SFRS corresponding to V_E, δ_E/R represents the roof drift of the SFRS corresponding to V, and δ represents the roof drift of the SFRS corresponding to the design-level earthquake ground motion assuming that the system has reached the plastic range C_d is defined as

$$C_d = \frac{\delta}{\delta_E} R \tag{10}$$
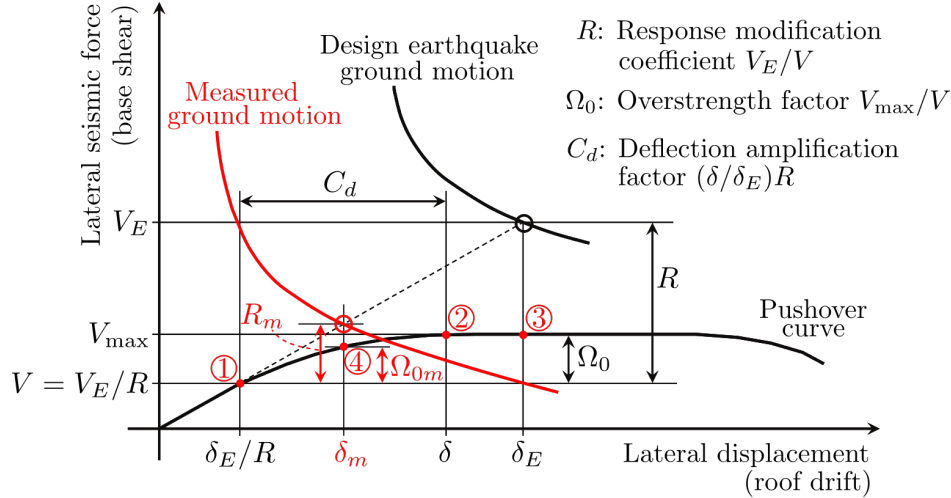
Figure 4. Illustration of seismic performance factors (R, Ω_0, and C_d)

For a measured (recorded) ground motion with an intensity lower than the design-level earthquake, the relationship of the expected base shear demand and the expected roof drift demand is represented by the red curve in Figure 4. The seismic performance factors R_m and Ω_{0m} at the measured roof drift δ_m (point 4) are lower than the R and Ω_0 expected for the design-level earthquake ground motion (point 3), respectively. Considering that the pushover curve is a property of the system, R_m varies between 1.0 when $\delta_m = \delta_E/R$ and R when $\delta_m = \delta_E$ (variation between points 1 and 3), and Ω_{0m} varies between 1.0 when $\delta_m = \delta_E/R$ and Ω_0 when $\delta_m = \delta$ (variation between points 1 and 2). Assuming that the deformation of the building follows the first-mode translational shape, the roof drift of the yielded building corresponding to the design-level earthquake ground motion is equal to the design upper limit or allowable story drift Δ_a given in ASCE/SEI 7-22 Table 12.12-1 for $h_{sx} = h_n$ (i.e., $\delta = \Delta_a$), and a linear variation of R_m and Ω_{0m} in terms of δ_m, the seismic performance factors for a measured ground motion can be estimated as

$$
R_m = \begin{cases} 1.0, & \delta_m < \frac{\delta_E}{R} = \frac{\Delta_a}{C_d} \\ 1.0 + \frac{(R-1.0)}{\Delta_a/C_d(R-1.0)}(\delta_m - \Delta_a/C_d), & \frac{\Delta_a}{C_d} \leq \delta_m < \frac{\Delta_a}{C_d}R \\ R, & \delta_m \geq \delta_E = \frac{\Delta_a}{C_d}R \end{cases} \tag{11}
$$

and

$$
\Omega_{0m} = \begin{cases} 1.0, & \delta_m < \frac{\delta_E}{R} = \frac{\Delta_a}{C_d} \\ 1.0 + \frac{(\Omega_0-1.0)}{\Delta_a(1.0-1/C_d)}(\delta_m - \Delta_a/C_d), & \frac{\Delta_a}{C_d} \leq \delta_m < \Delta_a \\ \Omega_0, & \delta_m \geq \Delta_a \end{cases} \tag{12}
$$

, respectively.

The authors acknowledge that this approach assumes that either the allowable roof drift controls the design or it is close to the roof drift corresponding to the design-level earthquake ground motion assuming that the system has reached the plastic range. The authors also acknowledge that the variation of the overstrength factor in terms of the roof drift is not linear. However, it is considered a practical approximation of R_m and Ω_{0m} used to compute the design acceleration coefficients per ASCE/SEI 7-22 Section 12.10.3 for measured ground motions with earthquake intensities different to the design-level earthquake intensity considering multiple building stations with various SFRS. The authors will continue the assessment of the assumptions during the remaining duration of the ongoing project.

Design-based Modified Acceleration Coefficients

The design acceleration coefficients are modified to consider the earthquake intensity of the measured ground motions. Four scaling approaches are used to modify the design acceleration coefficients. The design-based modified acceleration coefficients are compared with the peak floor accelerations at the center of rigidity induced by the measured ground motions.

Approach 1

This approach considers the design acceleration coefficients per ASCE/SEI 7-22 Section 12.10.3 scaled with respect to the ratio of the ground motion spectral acceleration over the design spectral acceleration at the estimated first-mode period ($S_a(T_1)/S_{ad}(T_1)$). This approach represents a case in which the design acceleration spectrum is scaled by $S_a(T_1)/S_{ad}(T_1)$ assuming the R and Ω_0 corresponding to a building behaving in the plastic range.

Approach 2

This approach considers the design acceleration coefficients per ASCE/SEI 7-22 Section 12.10.3 using $R = 1.0$ and $\Omega_0 = 1.0$ scaled with respect to the ratio of the ground motion spectral acceleration over the design spectral acceleration at the estimated first-mode period ($S_a(T_1)/S_{ad}(T_1)$). This approach represents a case in which the design acceleration spectrum is scaled by $S_a(T_1)/S_{ad}(T_1)$ assuming the R and Ω_0 corresponding to a building behaving in the linear-elastic range.

Approach 3

This approach considers the design acceleration coefficients per ASCE/SEI 7-22 Section 12.10.3 using $R = R_m$ and $\Omega_0 = \Omega_{0m}$ scaled with respect to the ratio of the ground motion spectral acceleration over the design spectral acceleration at the estimated first-mode period ($S_a(T_1)/S_{ad}(T_1)$). This approach represents a case in which the design acceleration spectrum is scaled by $S_a(T_1)/S_{ad}(T_1)$ assuming the R and Ω_0 corresponding to a building with an inelastic response depending on the earthquake intensity of the measured ground motion.

Approach 4

This approach considers the design acceleration coefficients per ASCE/SEI 7-22 Section

12.10.3 using $C_{p0} = S_a(T = 0.0\ [s]) = PGA$, $C_s = S_a(T_1)$, $C_{s2} = \sqrt{(S_a(T_2)^2 + S_a(T_3)^2)}$, $R = R_m$, and $\Omega_0 = \Omega_{0m}$. This approach represents a case in which the design acceleration spectrum is modified in scale and shape taking into account the ground motion spectral accelerations at $T = 0\ [s]$ and at the first-, second-, and third-mode periods assuming the R and Ω_0 corresponding to a building with an inelastic response depending on the earthquake intensity of the measured ground motion.

The first two scaling approaches represent extreme cases in terms of the level of inelastic response of the building stations. The third scaling approach includes the level of inelastic response based on the roof drift at the center of rigidity. The fourth scaling approach incorporates the shape of the ground motion spectral accelerations. The next section compares the magnitude and distribution over the building height of the design-based modified acceleration coefficients computed using the four scaling approaches with the peak floor accelerations at the center of rigidity from the measured ground motions.

Preliminary Comparison between Design-based Modified Acceleration Coefficients and Measured Peak Floor Accelerations

The design-based modified acceleration coefficients introduced in the previous section are compared with the peak floor accelerations at the center of rigidity for each combination of building station and seismic event listed in Table 1. The magnitude and distribution over the building height of the design-based acceleration coefficients are compared with the magnitude and distribution over the building height of the peak floor accelerations at the center of rigidity.

The average ratio of the peak floor accelerations (PFA_x) over the design-based modified acceleration coefficients (C_{pxm}) through the floors of the building (i.e., $r_{mag} = (1/N)\sum_{x=1}^{N} PFA_x/C_{pxm}$) is used as a metric to quantify the difference in magnitude between the design-based modified acceleration coefficients and the peak floor accelerations. r_{mag} larger than 1.0 indicates that the design-based modified acceleration coefficients underestimate the peak floor accelerations and r_{mag} lower than 1.0 indicates the design-based modified acceleration coefficients overestimate the peak floor accelerations.

The average ratio of the amplification of the peak floor accelerations (PFA_x/PGA; PGA: peak ground acceleration) over the amplification of the design-based modified acceleration coefficients (C_{pxm}/C_{p0m}) through the floors of the building (i.e., $r_{amp} = (1/N)\sum_{x=1}^{N}[(PFA_x/PGA)/(C_{pxm}/C_{p0m})]$) is used as a metric to quantify the difference in the distribution over the height of the building between the design-based modified acceleration coefficients and the peak floor accelerations. r_{amp} larger than 1.0 indicates that the design-based modified acceleration coefficients underestimate the amplification of the peak floor accelerations and r_{amp} lower than 1.0 indicates that the design-based modified acceleration coefficients overestimate the amplification of the peak floor accelerations over the height of the building.
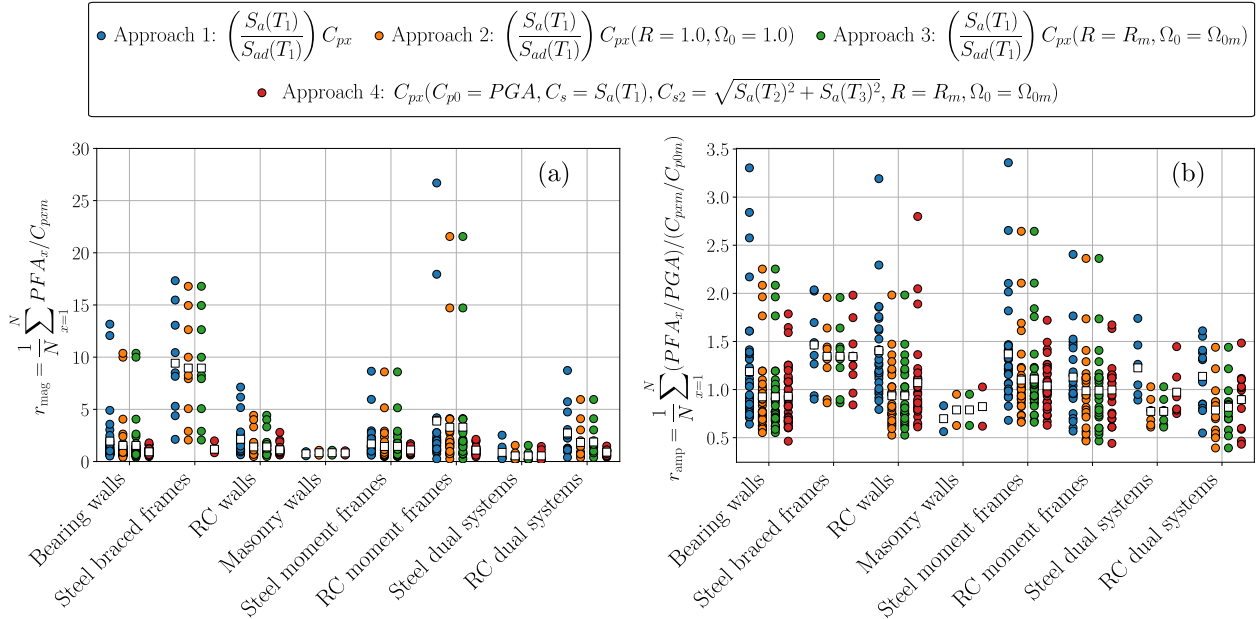
Figure 5 shows r_{mag} and r_{amp} in terms of the SFRS for each combination of building station and seismic events listed in Table 1 and the SFRS listed in Table 2. The four scaling approaches are shown in the figure. Each circular marker corresponds to one direction of

analysis (x or y) for one combination of building station and seismic event. The blue markers correspond to the scaling approach 1, the orange markers correspond to the scaling approach 2, the green markers correspond to the scaling approach 3, and the red markers correspond to the scaling approach 4. The square white markers correspond to mean values of r_{mag} and r_{amp} for each SFRS and scaling approach. The mean values and coefficients of variation of r_{mag} and r_{amp} are presented in Table 3 and Table 4, respectively. These tables also include the count of combinations of building stations and seismic events considering each direction of analysis as an independent data point. The last rows of Table 3 and Table 4 correspond to the mean values and coefficients of variations of r_{mag} and r_{amp}, respectively, considering all the SFRS.

Figure 5. r_{mag} and r_{amp} ratios in terms of the SFRS for each combination of building station and seismic events listed in Table 1 and the SFRS listed in Table 2. Design-based modified acceleration coefficients using four scaling approaches

Table 3. Mean values and coefficients of variation of the r_{mag} ratios

SFRS	Count	Mean value $\mu_{r_{mag}}$ (coefficient of variation $\sigma_{r_{mag}}/\mu_{r_{mag}}$ [%])			
		Approach 1	Approach 2	Approach 3	Approach 4
Bearing walls	40	1.95 (134.5)	1.54 (137.4)	1.54 (137.4)	0.93 (32.9)
Steel Braced frames	9	9.42 (54.6)	8.95 (57.6)	8.95 (57.6)	1.18 (27.6)
RC walls	27	2.13 (75.3)	1.40 (72.2)	1.40 (72.2)	1.12 (41.2)
Masonry walls	2	0.75 (37.4)	0.84 (39.1)	0.84 (39.1)	0.82 (35.0)
Steel moment frames	35	1.69 (91.9)	1.44 (106.6)	1.45 (106.0)	1.11 (25.0)
RC moment frames	23	3.87 (156.7)	3.28 (149.9)	3.29 (149.3)	1.09 (40.4)
Steel dual systems	6	0.88 (103.9)	0.54 (101.1)	0.54 (101.1)	0.54 (107.6)
RC dual systems	14	2.74 (83.2)	1.83 (85.0)	1.87 (81.6)	0.90 (32.8)
All	156	2.65 (136.9)	2.16 (147.7)	2.16 (147.1)	1.02 (37.5)

Almost all the design-based modified acceleration coefficients using the scaling approach 2 resulted in the same r_{mag} and r_{amp} that those obtained using the scaling approach 3. This

suggests that most of the building stations behaved in the linear-elastic or near to the linear-elastic range ($R_m \approx 1.0$ and $\Omega_{0m} \approx 1.0$) when they were subjected to the ground motions generated by the seismic events considered in this stage of the ongoing project. This is expected because most of the measured ground motions are lower in intensity than the design-level earthquake.

Figure 5a) and Table 3 shows that the design-based modified acceleration coefficients using the scaling approaches 1, 2, and 3 underestimate the magnitude of the peak floor accelerations. The mean values of the corresponding r_{mag} are larger than 2.0 with coefficients of variations larger than 130.0% for these scaling approaches. This suggests that scaling the design acceleration coefficients by the ratio $S_a(T_1)/S_{ad}(T_1)$ is not a good approach to estimate the magnitude of peak floor accelerations even if the level of inelastic response is well estimated. The design-based modified acceleration coefficients using the scaling approach 4 approximate reasonably well the magnitude of the peak floor accelerations. The mean value of r_{mag} is 1.02 with a coefficient of variation of 37.5% for this scaling approach. Considering the SFRS with more than 10 data points, the scaling approach 4 better estimates the magnitude of the peak floor accelerations for Bearing walls (r_{mag} closer to 1.0 with a coefficient of variation of 32.9%) and worse estimates the magnitude of the peak floor accelerations for the RC walls (r_{mag} further from 1.0 with a coefficient of variation of 29.6%), but still being a reasonable approximation.

Figure 5a) also shows that r_{mag} for some of the Steel braced frames and RC moment frames using the scaling approaches 1-3 are larger than 15.0, which means that the magnitude of the peak floor accelerations is severely underestimated using these scaling approaches.

Table 4. Mean values and coefficients of variation of the r_{amp} ratios

SFRS	Count	Mean value $\mu_{r_{amp}}$ (coefficient of variation $\sigma_{r_{amp}}/\mu_{r_{amp}}$ [%])			
		Approach 1	Approach 2	Approach 3	Approach 4
Bearing walls	40	1.19 (41.9)	0.92 (38.1)	0.92 (38.1)	0.93 (28.3)
Steel Braced frames	9	1.46 (29.5)	1.35 (25.4)	1.35 (25.4)	1.34 (28.7)
RC walls	27	1.41 (34.7)	0.94 (33.7)	0.94 (33.7)	1.07 (43.4)
Masonry walls	2	0.70 (33.8)	0.79 (36.5)	0.79 (36.5)	0.82 (46.5)
Steel moment frames	35	1.37 (36.1)	1.10 (34.6)	1.11 (35.4)	1.04 (22.3)
RC moment frames	23	1.13 (33.5)	0.99 (40.0)	0.99 (39.4)	1.00 (27.2)
Steel dual systems	6	1.23 (25.0)	0.77 (20.2)	0.77 (20.2)	0.97 (30.4)
RC dual systems	14	1.14 (27.2)	0.79 (34.9)	0.82 (31.5)	0.90 (29.8)
All	156	1.26 (39.8)	0.98 (39.8)	0.98 (39.6)	1.01 (33.6)

Figure 5b) and Table 4 shows that the distribution of the design-based modified acceleration coefficients over the heights of the buildings approximate reasonably well the distribution of the peak floor accelerations over the heights of the buildings. The mean values of the corresponding r_{amp} are in between 0.98 and 1.26 with coefficients of variations smaller than 40.0% for the scaling approaches considered in this analysis. Considering the SFRS with more than 10 data points, the scaling approach 4 better estimates the distribution of the peak floor accelerations over the height of the buildings for RC moment frames (r_{amp} closer to 1.0 with a coefficient of variation of 27.2%) and worse estimates the distribution of the peak floor accelerations over the height of the buildings for the RC dual systems (r_{amp} further from 1.0 with a coefficient of variation of 33.6%), but still being a good approximation.

The authors are evaluating the implementation of other metrics to compare the acceleration coefficients computed based on the design provision equations and the measured peak floor accelerations.

Conclusions

The analysis of the results of the ongoing project presented in this document suggests that:

- The equations to compute the design acceleration coefficients per ASCE/SEI 7-22 Section 12.10.3 can predict reasonably well the magnitude of the peak floor accelerations when the spectral accelerations of the measured ground motions at $T = 0\ [s]$ and at the first-, second-, and third-mode periods are considered. The scaling approaches that considered only the spectral accelerations of the measured ground motions at the first-mode periods underestimate the peak floor accelerations.

- The equations to compute the design acceleration coefficients per ASCE/SEI 7-22 Section 12.10.3 can predict reasonably well the distribution of the peak floor accelerations over the height of the building. However, measured data or simulated data at the design-level earthquake intensity is required to fully validate the design provisions.

Acknowledgments

References

ASCE/SEI 7-22 (2021). Minimum design loads and associated criteria for buildings and other structures. *American Society of Civil Engineers*.

Bull, D. K. (2004). Understanding the Complexities of Designing Diaphragms in Buildings for Earthquakes. *Bulletin of the New Zealand Society for Earthquake Engineering* 37, no. 2: 70–88. https://doi.org/10.5459/bnzsee.37.2.70-88.

Chen, Michelle C., Pantoli, E., Wang, X., Astroza, R., Ebrahimian, H., Hutchinson, T.C., Conte, J.P., Restrepo, J. I., Marin, C., Walsh, K. D., Bachman, R.E., Hoehler, M.S., Englekirk, R., and Faghihi, M. (2016). "Full-Scale Structural and Nonstructural Building System Performance

during Earthquakes: Part I – Specimen Description, Test Protocol, and Structural Response." *Earthquake Spectra* 32, no. 2: 737–70. https://doi.org/10.1193/012414eqs016m.

Choi, H., Christopoulos, C., and Tremblay, R. (2008). Comparison of the Seismic Response of Steel Buildings Incorporating Self-Centering Energy Dissipative Braces, Buckling Restrained Braced and Moment Resisting Frames. Research Report 05-2008, University of Toronto, Canada.

Chopra, Anil K (2007). *Dynamics of Structures*. Pearson Education.

Federal Emergency Management Agency (FEMA) (2009). FEMA P695 Recommended Methodology for Quantification of Building System Performance and Response Parameters. *Project ATC-63*, Prepared by the Applied Technology Council, Redwood City.

Fleischman, R. B., and Farrow, K. T. (2001). Dynamic Behavior of Perimeter Lateral-System Structures with Flexible Diaphragms. *Earthquake Engineering & Structural Dynamics* 30, no. 5: 745–63. https://doi.org/10.1002/eqe.36.

Fleischman, R. B., Restrepo, J. I., Naito, C. J., Sause, R., Zhang, D., and Schoettler, M. (2013). "Integrated Analytical and Experimental Research to Develop a New Seismic Design Methodology for Precast Concrete Diaphragms." *Journal of Structural Engineering* 139, no. 7: 1192–1204. https://doi.org/10.1061/(ASCE)ST.1943-541X.0000734.

González, Alfredo, Spacone, E., and Nascimbene, R. (2017). Performance-Based Seismic Design Framework for RC Floor Diaphragms in Dual Systems. *Procedia Engineering*, X International Conference on Structural Dynamics, EURODYN 2017, 199: 3546–51. https://doi.org/10.1016/j.proeng.2017.09.512.

Henry, Richard S., Dizhur, D., Elwood, K. J., Hare, J., and Brunsdon, D (2017). Damage to Concrete Buildings with Precast Floors during the 2016 Kaikoura Earthquake. *Bulletin of the New Zealand Society for Earthquake Engineering* 50, no. 2: 174–86. https://doi.org/10.5459/bnzsee.50.2.174-186.

Iverson, J. K., and Hawkins, N. M. (1994). Performance Of Precast/Prestressed Building Structures During Northridge Earthquake. *PCI Journal* 39, no. 2. https://trid.trb.org/view/390643.

Kam, W. Y., Pampanin, S., and Elwood, K. (2011). Seismic Performance of Reinforced Concrete Buildings in the 22 February Christchurch (Lyttleton) Earthquake. *University of Canterbury. Civil and Natural Resources Engineering*. https://ir.canterbury.ac.nz/handle/10092/9006.

Mayorga, C.F., and Tsampras. G., (2022). Validation of seismic design provisions for diaphragms and assessment of higher-mode responses on earthquake-resistant buildings. *Strong Motion Instrumentation Program Seminar*, Department of Conservation, California.

Miranda E., and Reyes C.J. (2002). Approximate lateral drift demands in multistory buildings with nonuniform stiffness. *ASCE Journal of Structural Engineering* 128, no. 7: 840–849 https://doi.org/10.1061/(ASCE)0733-9445(2002)128:7(840).

Miranda E., and Taghavi S. (2005). Approximate floor acceleration demands in multistory buildings I: Formulation. *ASCE Journal of Structural Engineering* 131, no. 2: 203–211 https://doi.org/10.1061/(ASCE)0733-9445(2005)131:2(203).

Panagiotou, Marios, and Restrepo, J. I. (2009). Dual-Plastic Hinge Design Concept for Reducing Higher-Mode Effects on High-Rise Cantilever Wall Buildings. *Earthquake Engineering & Structural Dynamics* 38, no. 12: 1359–80. https://doi.org/10.1002/eqe.905.

Panagiotou, Marios, Restrepo, J. I., and Conte, J. P. (2011). Shake-Table Test of a Full-Scale 7-Story Building Slice. Phase I: Rectangular Wall. *Journal of Structural Engineering* 137, no. 6: 691–704. https://doi.org/10.1061/(ASCE)ST.1943-541X.0000332.

Priestley, M. J., and Alejandro D. Amaris (2002). *Dynamic Amplification of Seismic Moments and Shear Forces in Cantilever Walls*. IUSS Press.

Şafak, Erdal, and Çelebi, M (1990). Method to Estimate Center of Rigidity Using Vibration Recordings. *Journal of Structural Engineering* 116, no. 1: 85–97. https://doi.org/10.1061/(ASCE)0733-9445(1990)116:1(85).

Scarry, J M (2014). Floor Diaphragms – Seismic Bulwark or Achilles' Heel. *NZSEE Conference*, Auckland, New Zealand.

Sewell, R. T., Cornell, C. A., Toro, G. R., and McGuire, R. K. (1986). A Study of Factors Influencing Floor Response Spectra in Nonlinear Multi-Degree-of-Freedom Structures. *John A. Blume Earthquake Engineering Center Technical Report Series*. https://purl.stanford.edu/vf765pj9489.

Tilt-up-Wall Buildings. (1996). *Earthquake Spectra* 12, no. 1 (suppl): 99–123. https://doi.org/10.1193/1.1585922.

Taghavi, S. and Miranda, E. (2005). Approximate Floor Acceleration Demands in Multistory Buildings. II: Applications. *Journal of Structural Engineering* 131, no. 2: 212–220. https://doi.org/10.1061/(ASCE)0733-9445(2005)131:2(212).

Tsampras, Georgios, Sause, R, Zhang, D., Fleischman, R. B, Restrepo, J. I., Mar, D., and Maffei, J. (2016). Development of Deformable Connection for Earthquake-Resistant Buildings to Reduce Floor Accelerations and Force Responses. *Earthquake Engineering & Structural Dynamics* 45, no. 9: 1473–94. https://doi.org/10.1002/eqe.2718.

Van Rossum, G., and Drake, F. L. (2009). Python 3 Reference Manual. Scotts Valley, CA: CreateSpace.

Wallace, John W., Massone, L. M., Bonelli, P., Dragovich, J., Lagos, R., Lüders, C., and Moehle, J. (2012). Damage and Implications for Seismic Design of RC Structural Wall Buildings. *Earthquake Spectra* 28, no. 1(supl): 281–99. https://doi.org/10.1193/1.4000047.

Wiebe, L., and Christopoulos, C. (2009). Mitigation of Higher Mode Effects in Base-Rocking Systems by Using Multiple Rocking Sections. *Journal of Earthquake Engineering* 13, no. sup1: 83–108. https://doi.org/10.1080/13632460902813315.

Xiang, Yijun, Harris, A., Naeim, F., and Zareian, F. (2016). Identification And Validation of Natural Periods and Modal Damping Ratios for Seismic Design and Building Code. *SMIP16 Seminar Proceedings*.

ASSESSMENT OF VIBRATION CHARACTERISTICS OF BRIONES AND TERMINUS DAMS USING EARTHQUAKE RECORDINGS

Makbule Ilgac and Adda Athanasopoulos-Zekkos

University of California, Berkeley

Abstract

The potential dam failure modes related to earthquakes are often the driving design criteria for new dams and the primary concern when evaluating the safety of existing dams. Ground motion recordings on dam sites at different locations were studied to estimate dams' fundamental and second mode vibration. Earthquake-based horizontal to vertical ratio (HVSR) are evaluated. Fourier amplification ratios using crest records over the abutment or downstream records are also assessed. The vibration characteristics are evaluated based on different methods and the resulting estimate of the fundamental frequency and second mode of vibration for Briones and Terminus dams are presented.

Introduction

The seismic response of earth dams is admittedly rather complicated and therefore advanced methods of dynamic analysis need to be employed to capture the actual behaviour of dams under seismic conditions. Such methods and associated advanced constitutive models do exist nowadays, but they need to be further developed and validated against known case studies, so that reliable results can be obtained for further dam analysis and design. Various methods have been developed over the years and these range from the simple numerical shear beam method up to the sophisticated nonlinear coupled dynamic analysis including consideration of reservoir-dam interaction effects. However, it is important to note, that as the methods become more sophisticated and can capture more aspects of the soil response, the nonlinearity as well as the reservoir-dam interaction during shaking, the analyses become computationally intensive.

When evaluating the seismic response of earth dams, dam fundamental frequency and second mode vibration are the key parameters in the dynamic response of a dam, can be assessed using the horizontal-to-vertical spectral ratio (HVSR) and Fourier amplification ratio from crest to abutment or downstream records. The HVSR is mostly assessed by performing microtremor measurements in the field. However, when earthquake records are available, HVSR can also be calculated using the recorded earthquake motions. Additionally, cross spectra which is defined here as the Fourier amplitude spectra of the horizontal component (FASH) of the crest records over the FASH of the abutment or downstream records are also indicative of vibration characteristics of the dam. With that purpose, our vision is to use existing ground motion recordings at earth dam sites that are part of the California Strong Ground Motion Instrumentation Program (CSMIP) database to develop a simpler approach to investigate the dynamic characteristics of dam sites. Specifically, our approach aims to compute and analyze the horizontal-to-vertical spectral ratio (HVSR) and cross spectra at sensor locations positioned at dam sites using earthquake recordings and investigate the dam resonant frequencies. For that

purpose, ground motion data on dam sites at different locations (i.e., right crest, left crest, etc.) are cataloged and processed. First signal-to-noise ratios (SNR) were calculated to determine the usable frequency range and assess the quality of the ground motions. The processed motions are used to study the vibration characteristics of dams.

The HVSR is the ratio between the Fourier amplitude spectra (FAS) of the horizontal and the vertical component of microtremors was first introduced by Nogoshi and Igarashi (1970 and 1971), and widely used following the study by Nakamura (1989, 1996, 2000). Several researchers studied HVSR method, either using microtremors (mHVSR) (Nagoshi and Igarashi (1971), Nakamura (1989, 2000), Yong et al. (2013)) or strong ground motion data (eHVSR) (Lermo & Chavez-Garcia (1993), Hassani et al. (2020)), as an indicator of the subsurface conditions and can be successfully applied for identifying the fundamental resonance frequency. Earthquake-based HVSRs are calculated as the Fourier amplitude spectra ratio of the horizontal to vertical components (FASH/FASV) of the ground motion records at the surface using the intense S-wave portion and using the entire motion which are two common approaches in the literature. Studying the dam vibration characteristics, Fourier amplitude ratio can be calculated as the ratio of FFTcrest to FFTabutment or FFTdownstream records. The vibration characteristics are evaluated based on different methods and the resulting estimate of the resonance frequencies to understand the local and site-specific features for Briones and Terminus Dam sites at different locations (i.e., right crest, left crest, etc.) are presented in this study.

Description of Selected Dams

Briones Dam

Briones Dam is located in the western part of Contra Costa County within the San Francisco Bay Area (37.9135 N, 122.2092 W), and built in 1964. The dam is an earth dam and serves a primary purpose of flood control and water supply. It stands at an elevation of 189 meters, with a height of 273 feet (81.9 meters) and a crest length of 2100 feet (630 meters). In 1975, a total of nine accelerometers were installed, positioned on the center and left crests (Loc2, Loc3) as well as the left abutment (Loc1) of the dam. Figure 1 shows the plan view of the dam and the installed accelerometers (California Strong Motion Instrumentation Program, 2014). The accelerometer placed at the center crest and the one at the left crest are oriented in alignment with the dam's transverse and longitudinal directions. The sensor at the left abutment orientation was updated due to field change after 06/24/2014 from 31° and 121° to 90° and 360°. Site investigation data and cross sections of the dam could not be acquired for Briones Dam which would provide important information in understanding the dynamic behaviour of the dam. Between 1984 and 2021, Briones Dam experienced several earthquake events, and 16 of them are documented by CSMIP with recordings at the right and left crest, and the left abutment locations. These earthquakes occurred at epicentral distances ranging from 6 to 35 kilometers and have magnitudes (M_w) from 3.3 to 6.0 with peak acceleration (PGA), from 0.09 g to 0.18 g (geometric mean of the two-horizontal components). The largest PGA was recorded at the dam was during the Piedmont Area Earthquake on July 20, 2007, which had a magnitude of 4.2 and PGA of 0.18 g at the left crest of the dam. Accelerograms were bandpass filtered with at 0.30 and 40.00 Hz and instrument- and baseline-corrected by CSMIP database. Moment magnitude, epicentral ($R_{epi.}$) and hypocentral (R_h) distances and PGA at three sensor location for the 16 recorded events are provided in Table 1.
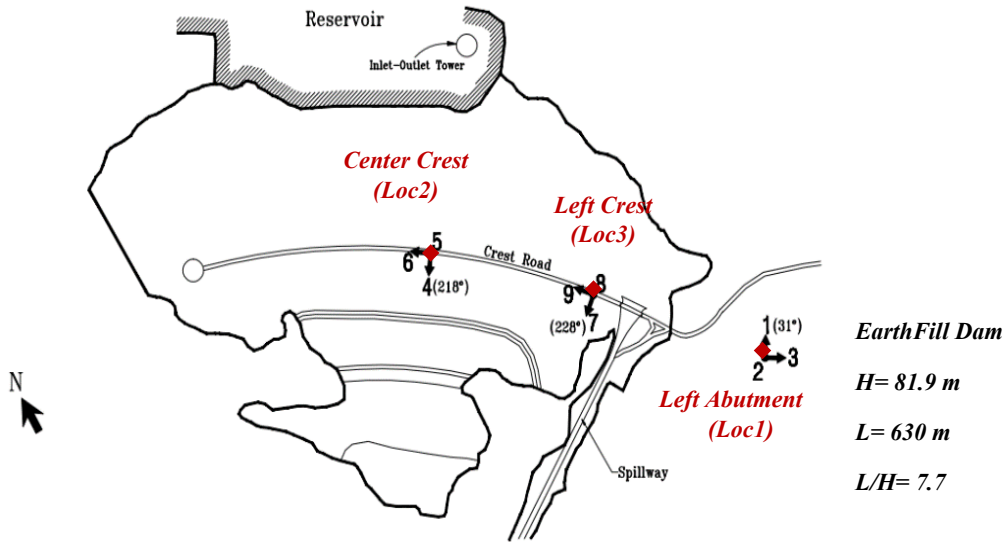
Figure 1. Plan view of Briones Dam (CGS - CSMIP Station CE 58183, diagram revised on 7/16/14, CGS: California Geological Survey)

Table 1. Information on earthquake data recorded in Briones Dam

EQ #	M_w	$R_{epi.}$ (km)	R_h (km)	Left Abutment (Loc1) PGA*	Center Crest (Loc2) PGA*	Left crest (Loc3) PGA*
2	3.6	6.5	11.1	0.03	0.02	0.03
3	4.2	12	13.3	0.09	0.13	0.18
4	6.0	35.2	37.0	0.02	0.04	0.04
5	4.0	8.8	10.0	0.06	0.04	0.07
6	4.1	9.9	19.3	0.04	0.07	0.08
7	3.5	19.6	21.2	0.01	0.01	0.01
8	4.0	7.5	11.0	0.05	0.03	0.03
9	3.8	6.3	11.5	0.06	0.03	0.03
10	3.5	6.1	11.5	0.02	0.01	0.01
11	3.9	8.4	12.5	0.04	0.07	0.04
12	3.8	7.7	14.4	0.01	0.02	0.01
13	4.4	6.6	14.0	no data	0.03	0.03
14	3.5	7	11.6	0.02	0.01	0.02
15	3.3	7	11.6	0.02	0.01	0.01
16	4.5	13.5	19.5	0.04	0.12	0.11
17	3.9	24.3	26.0	0.01	0.01	0.02

* PGA units are in g and the values presented as the geometric mean of the two horizontal component

Terminus Main and Auxiliary Dams

Terminus main and auxiliary dams are located on Kaweah River in Tulera County, California (36.4102 N, 119.0050W), and built in 1962. The dam is an earth dam and serves a primary

purpose of flood control and irrigation water supply. It stands at an elevation of 297 meters. The main dam has a height of 255 feet (78 meters) and a crest length of 2375 feet (724 meters) (data taken from http://cdec.water.ca.gov/) and the auxiliary dam has a height of 144 feet (44 meters) and a crest length of 876 feet (267 meters) approximately measured from the Google Earth. A total of five accelerometers were installed, positioned on the right crest (Loc5), mid-slope (Loc6), right abutment (Loc4), downstream (Loc3) and upper tower (Loc7) of the main dam. Two accelerometers were installed on auxiliary dam, positioned on the center crest (Loc2) and right abutment (Loc1) of the dam. Figure 2 shows the plan view of the dams and the installed accelerometers by California Strong Motion Instrumentation Program along with simplified plan view sketches prepared for both dams. The accelerometers placed at the center crest and abutments are oriented in alignment with the dams' transverse and longitudinal directions for both structures. Site investigation data and cross sections of the dams could not be acquired for Terminus Dams which would provide important information in understanding the dynamic behaviour of the dam.
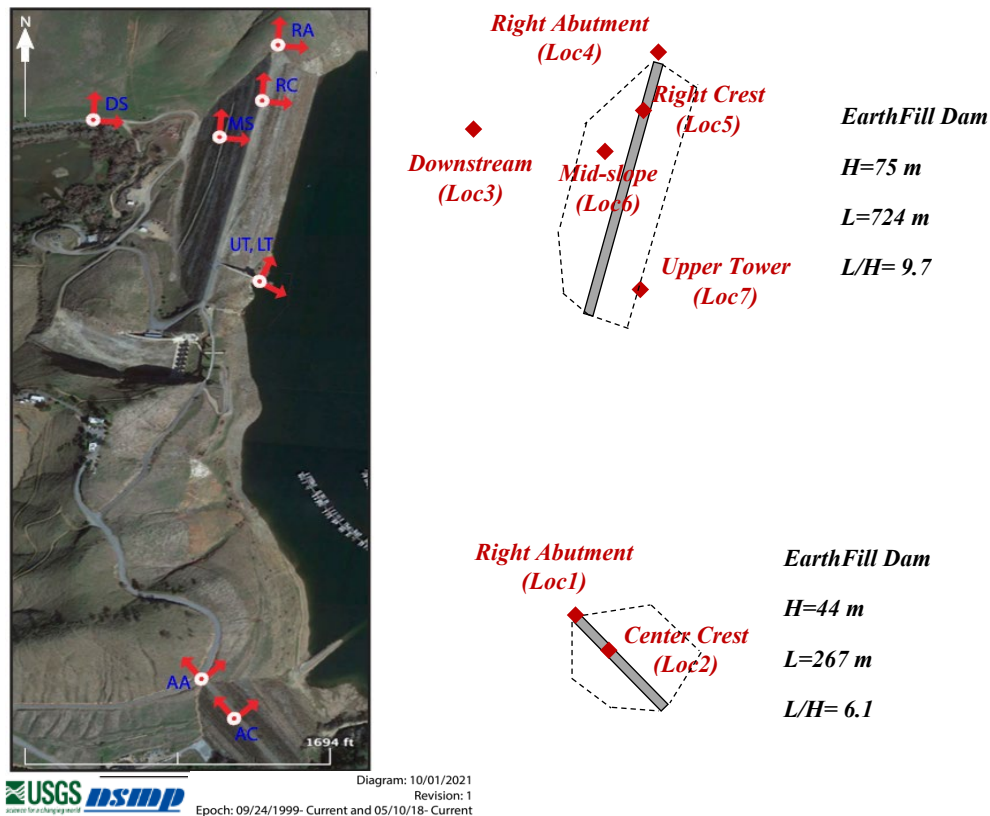
Figure 2. Plan view of Terminus main and auxiliary dams (Terminus Dam NSMP Station 1098, diagram revised on 10/01/21, NSMP: National Strong Motion Project)

CMSIP database provides two earthquake recordings for Terminus Dams. 4th of July 2019 and 5th of July 2019 Ridgecrest Earthquakes occurred at epicentral distances of 156 and 145 km kilometers and have magnitudes (M_w) of 6.4 and 7.1. The peak acceleration (PGA) at the main dam right crest was recorded as 0.03 g and 0.05 g (geometric mean of the two-horizontal components) for 6.4 and 7.1 magnitude events respectively. Similarly, the peak acceleration (PGA) at the auxiliary dam crest was recorded as 0.05 g and 0.08 g for 6.4 and 7.1 magnitude

events. Accelerograms were bandpass filtered at 0.10 and 40.00 Hz and instrument- and baseline-corrected by the CSMIP database. Moment magnitude, epicentral ($R_{epi.}$) and hypocentral (R_h) distances, and PGA at 5 sensor locations for the two recorded events are provided in Table 2.

Table 2. Information on earthquake data recorded in Terminus Dam

EQ #	1	2
M_w	6.4	7.1
$R_{epi.}$ (km)	156.1	145.2
R_h (km)	156.5	145.4
Location	**PGA (g)**	
Loc 1-Aux Dam Right Abutment	0.01	0.02
Loc 2-Aux Dam Crest	0.05	0.08
Loc 3-Main Dam Downstream	0.01	0.02
Loc 4-Main Dam Right Abutment	0.01	na
Loc 5-Main Dam Right Crest	0.03	0.05

* PGA units are in g and the values are presented as the geometric mean of the two-horizontal component

Signal-to-Noise Ratio (SNR)

Signal-to-noise ratio can be defined as the ratio of the Fourier amplitude spectrum of the signal (S-wave) time window by the spectrum of the pre-event noise. SNR provides information on the quality of the ground motions if the amplitude of the signal is strong enough (e.g., SNR>2-10) at a given frequency to be used in various applications (e.g., HVSR analysis). Hence, SNR calculation provides a usable frequency range and allows us to detect high-quality data.

For the ground motion dataset of Briones and Terminus Dam, SNRs are calculated for 55 earthquake recordings. For this study we followed the procedure describe in Kishida et al. (2016) which provides a semi-automated procedure for windowing time series and computing Fourier amplitude spectra to extract various waves. Different window series (pre-event noise, P-wave and S-wave and coda wave) were extracted, and visual examination of the recording was performed to attain a better-quality dataset. Fourier amplitude spectra of different windows were calculated and smoothed with Konno and Ohmachi (1988) (b=20) functions. SNR cutoff value of 3 (e.g., Field and Jacob, 1995) is used to determine the usable frequency range. We have also chosen to carefully assess the vertical components data quality which most of the time has higher noise than horizontal components, as the one of the purposes of the SNR calculation is to compute HVSR in this study.

An illustrative example is shown to present the extraction of time windows and calculation of SNR following the procedure by Kishida et al (2016). Figure 3a shows the vertical direction of th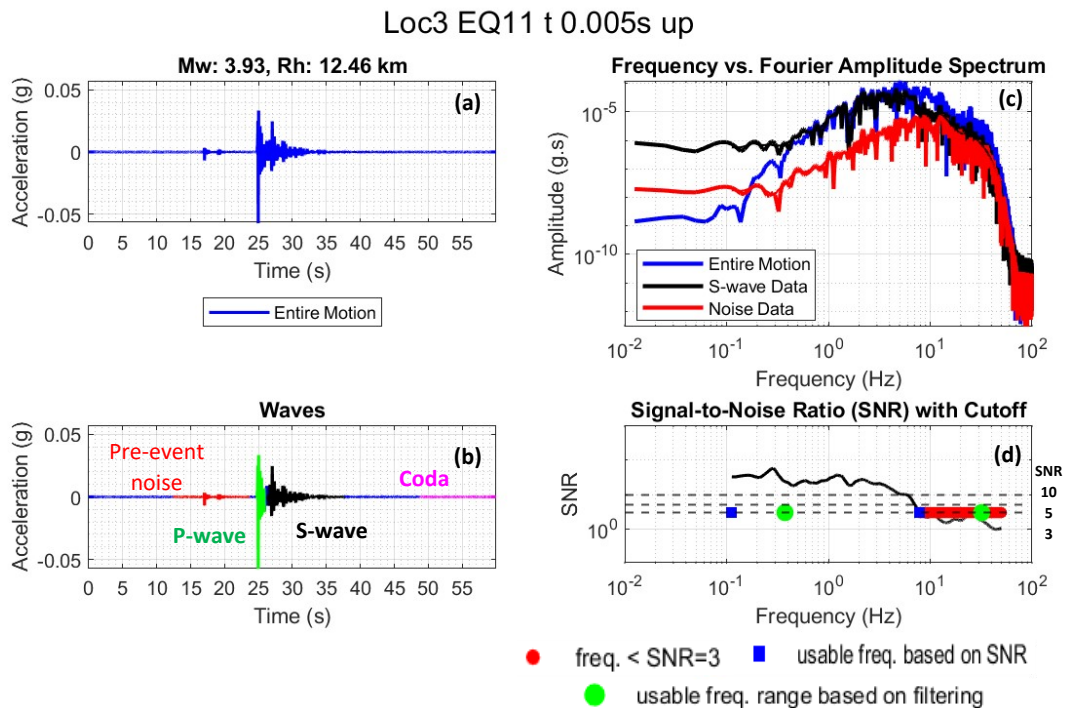e acceleration time history of El Cerrito Earthquake of 5th of March 2012 (EQ11) recorded at the left crest (Loc3) of Briones Dam. M_w is 3.93 and hypocentral distance is 12.46 km for this

event. Figure 3b shows the different window series (pre-event noise, P-wave and S-wave and coda wave) and Figure 4c presents the FAS of the signal and noise window series. SNR with cutoff limits of 3-5-10 is plotted on Figure 3d along with the usable frequency range of 0.1 to 8 Hz which is determined with an SNR cutoff value of 3. The same examination was performed for the transverse and longitudinal components as well. The resulting usable frequency range is determined by comparing the results of three component data as 0.1-8 Hz. 45 recording 3 component data, in total 135 acceleration time history are examined for Briones Dam. The lowest usable frequency range varies between 0.1-1.1 Hz and the highest usable frequency ranges between 7.9-50 Hz.

A similar exercise is performed for 10 recording 3 component data, in total 30 acceleration time history for Terminus Dams. When the event noise window is not adequate (shorter than 10 sec), coda waves are used to evaluate the quality of data. 4th of July 2019 and 5th of July 2019 Ridgecrest Earthquakes recorded at Terminus Dam had short noise durations hence signal to coda ratio was assessed with a cutoff value of 2 to determine the usable frequency range. The lowest usable frequency range varies between 0.3-0.5 Hz and the highest usable frequency of 40 Hz for the records at Terminus Dams.

Figure 3. (a) Acceleration time history of El Cerrito Earthquake of 5th of March 2012 (EQ11) recording at left crest (Loc3) of Briones Dam in vertical direction, (b) different window series (pre-event noise, P-wave and S-wave and coda wave), (c) FAS of the Signal and Noise window series, (d) SNR with cutoff limits of 3-5-10.

Horizontal-to-Vertical Spectral Ratio

There exist several different approaches to assess HVSR based on ground motion data. One of the most common approaches is using the intense S-wave part of the records with a SNR above a

certain cutoff. In this approach Fourier amplitude spectra ratio of the horizontal to vertical components (FAS$_H$/FAS$_V$) of the ground motion records using the intense S-wave portion is calculated (e.g., Kawasee et al 2011, Ktenidou et al 2015). Another alternative is using the complete waveforms (typically P$_{wave}$ arrival to end of S$_{coda}$). (e.g., Zhu et al 2020). After calculating HVSR for each event, the logarithmic mean and standard deviation of the HVSR curve at each dam sensor location are calculated as given in Equation 1 and 2. The resonant frequencies of dam are defined as the peak frequencies of the average HVSR curve. Note that 'n' is the number of recordings at dam in Equations 1 and 2.

$$\ln\left(\overline{HVSR}(f)\right) = \frac{\left(\sum_{j=1}^{n} \ln\left(HVSR_j(f)\right)\right)}{n} \qquad \text{Eq. 1}$$

$$stdev(f) = \sqrt{\frac{\sum_{j=1}^{n}\left(\ln\left(HVSR_j(f)\right) - \ln\left(\overline{HVSR_j}(f)\right)\right)^2}{n-1}} \qquad \text{Eq. 2}$$

In this study, we calculated HVSR by using entire and S-wave portion approaches and compared the resultant vibration characteristics with Fourier amplification ratios at dam sites. The result of the HVSR analysis for the Briones and Terminus dams will be discussed in detail next.

Briones Dam

We have attempted to calculate HVSR in the longitudinal and transverse (upstream-downstream) direction of the dam to determine the vibration characteristics (first (fundamental) and second mode) of Briones Dam at Center Crest (Loc2) and Left Crest (Loc3) separately.

Figure 4a and b and Figure 5a and b present the HVSR results of 16 earthquake data (gray line) along with the logarithmic mean (solid line) and standard deviation (dashed line) of HVSR curves at the center crest (Loc2) and left crest (Loc3) in transverse and longitudinal directions using the intense part of the motions (S-wave). Two vertical dashed lines HVSR=0.5 and 2 are also plotted to investigate the amplifications which are greater than ~2. The first mode (fundamental) frequencies of the Briones dams are determined as 1.2 and 1.0 Hz at center crest (Loc2) in longitudinal and transverse directions respectively and 0.9 Hz at left crest (Loc3) in both directions. The second mode of vibration was observed at 6.1 Hz and 4.7 Hz at center crest (Loc 2) in longitudinal and transverse directions respectively. Whereas second mode peaks were observed at 3.6 Hz and 3.7 Hz at left crest (Loc3) in longitudinal and transverse directions respectively.

The HVSR using the same set of earthquake motions are also calculated using the entire record. Figure 6a and b and Figure 7 ab and b present the HVSR results of 16 earthquake data (gray line) along with the logarithmic mean (solid line) and standard deviation (dashed line) of HVSR curves at the center crest (Loc2) and left crest (Loc3) in longitudinal and transverse directions. The first mode (fundamental) frequencies of the Briones dams are determined as 1.2 and 1.0 Hz at center crest (Loc2) in longitudinal and transverse directions and 0.9 Hz at left crest (Loc3) in both directions. The second mode of vibration was observed at 5.9 Hz at center crest (Loc 2) in longitudinal and no clear peak was observed in transverse directions. Whereas second mode peaks were observed at 3.6 Hz at left crest (Loc3) in longitudinal and transverse directions.
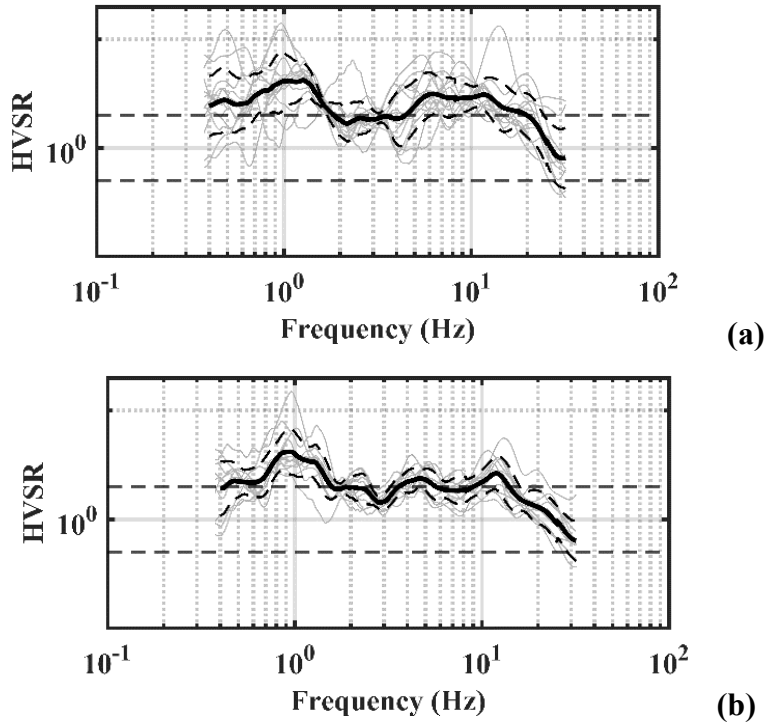
Figure 4. HVSR results of earthquake data (gray line) along with the mean (solid line) and standard deviation (dashed line) of HVSR curves using S-wave at the center crest (Loc2) in a) longitudinal and b) transverse directions.
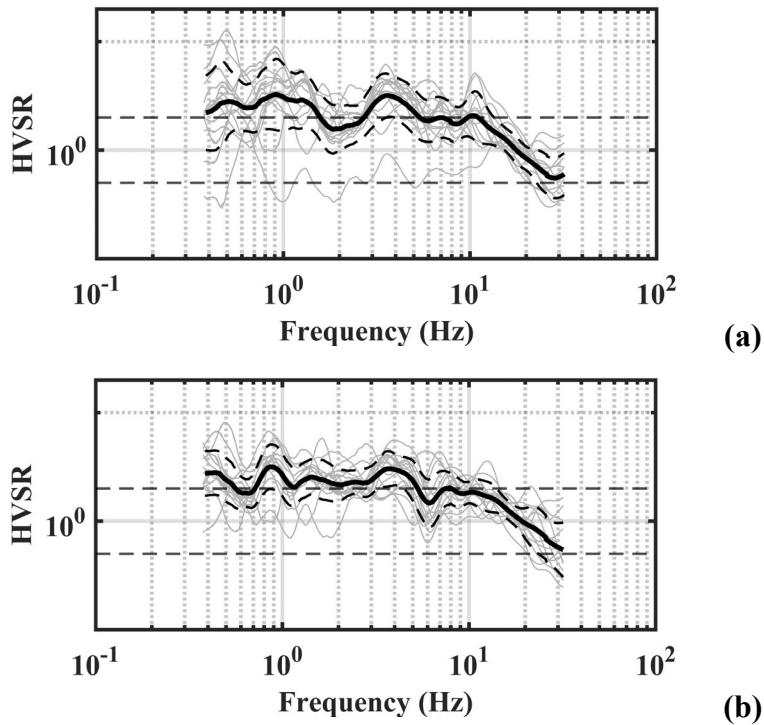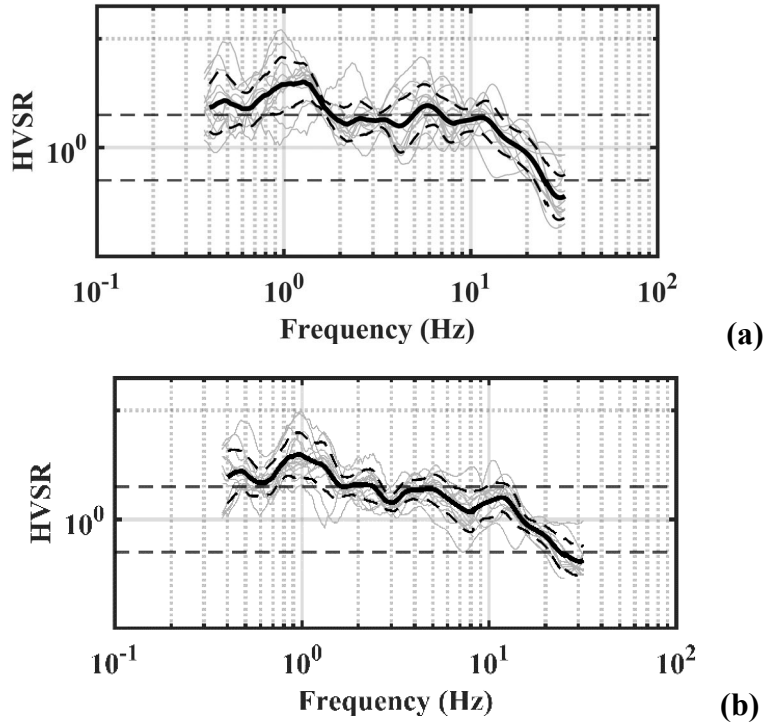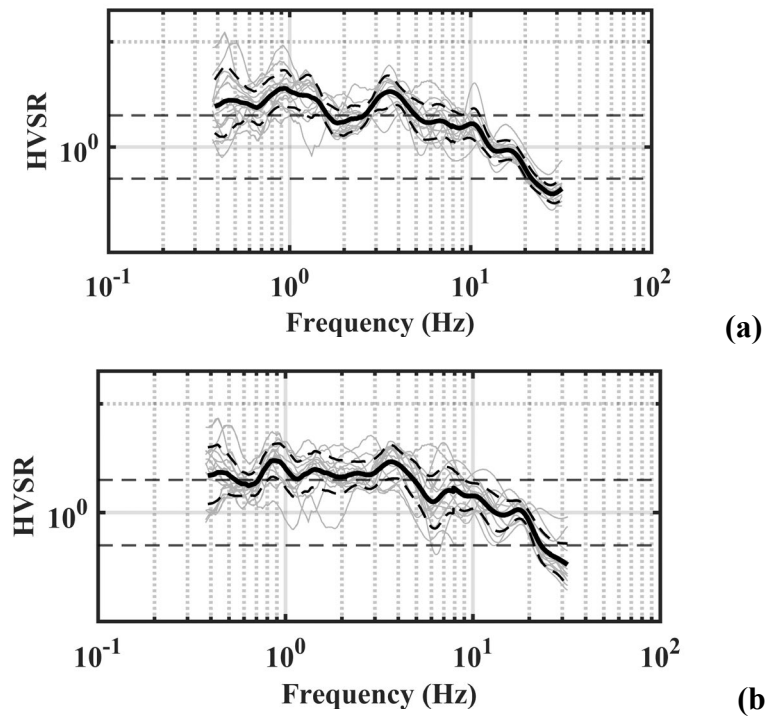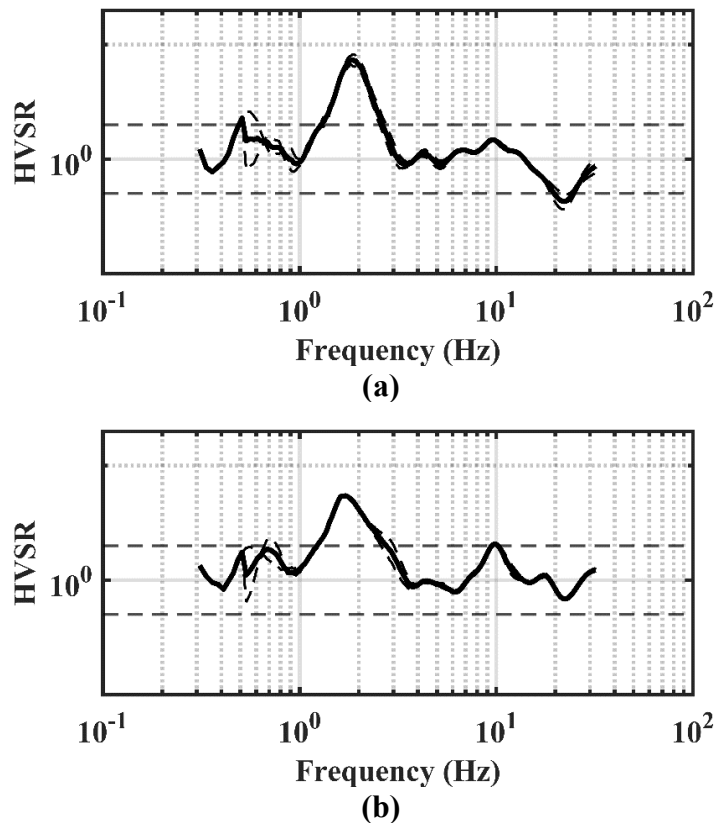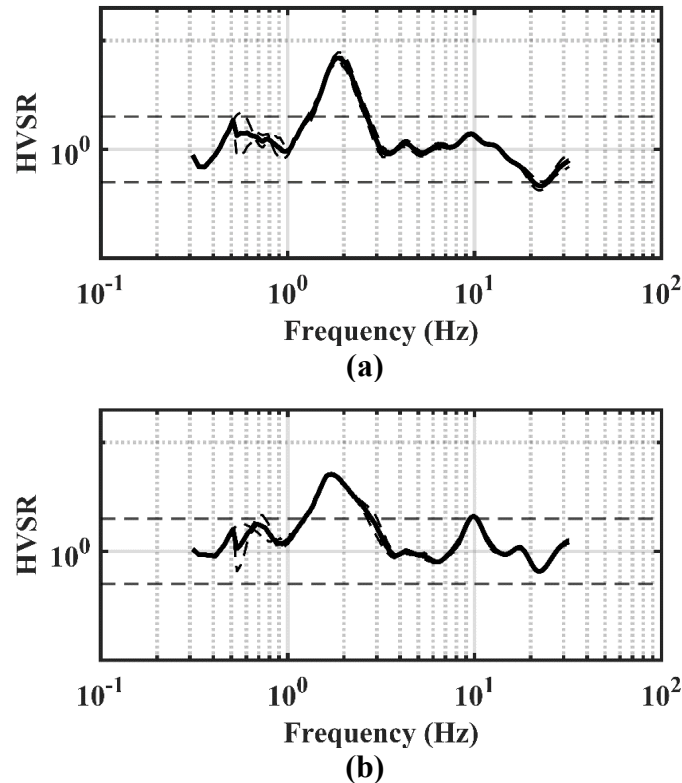

Figure 5. HVSR results of earthquake data (gray line) along with the mean (solid line) and standard deviation (dashed line) of HVSR curves using S-wave at the left crest (Loc3) in a) longitudinal and b) transverse directions.

(a)

(b)

Figure 6. HVSR results of earthquake data (gray line) along with the mean (solid line) and standard deviation (dashed line) of HVSR curves using entire record at the center crest (Loc2) a) in longitudinal and b) transverse direction.

(a)

(b)

Figure 7. HVSR results of earthquake data (gray line) along with the mean (solid line) and standard deviation (dashed line) of HVSR curves using entire record at the left crest (Loc3) a) in longitudinal and b) transverse direction.

Terminus Dam

HVSR in longitudinal and transverse (upstream-downstream) direction of the Terminus main and auxiliary dams are also calculated to determine the vibration characteristics (first (fundamental) and second mode) at the main dam right crest (Loc5). Figure 8a and b presents the HVSR results of 2 earthquake data (gray line) along with the logarithmic mean (solid line) and standard deviation (dashed line) of HVSR curves at the right crest (Loc5) in transverse and longitudinal directions using the intense part of the motions (S-wave). The first mode (fundamental) frequencies of the Terminus dams are determined as 1.9 and 1.7 Hz at right crest (Loc5) in longitudinal and transverse directions respectively. The second mode of vibration was observed at 9.6 Hz and 9.8 Hz at right crest (Loc5) in longitudinal and transverse directions being less clear in longitudinal direction.
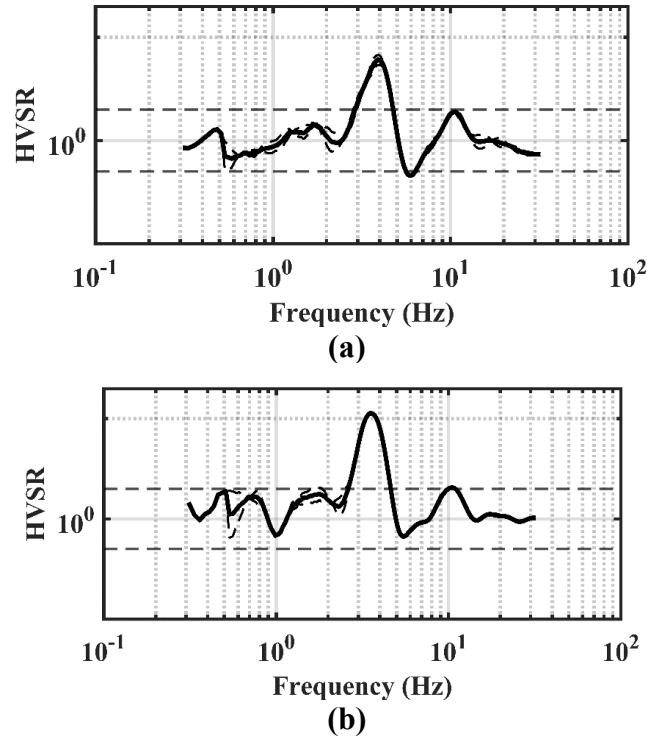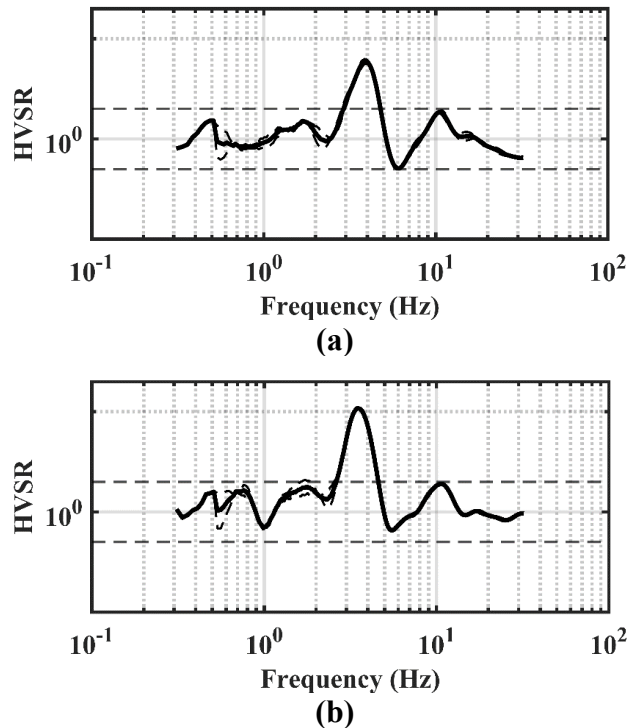

(a)

(b)

Figure 8. HVSR results of earthquake data (gray line) along with the mean (solid line) and standard deviation (dashed line) of HVSR curves using S-wave at the main dam right crest (Loc5) in a) longitudinal and b) transverse directions.

The HVSR using the same set of earthquake motions are also calculated using the entire record. Figure 9a and b present the HVSR results of 2 earthquake data (gray line) along with the logarithmic mean (solid line) and standard deviation (dashed line) of HVSR curves at the right crest (Loc5) in longitudinal and transverse directions. The first mode (fundamental) frequencies of the Terminus dams are determined as 1.9 and 1.7 Hz at right crest (Loc5) in longitudinal and transverse directions. The second mode of vibration was observed at 9.7 Hz and 10 Hz in longitudinal and transverse directions again less clear in longitudinal direction. First (fundamental) and second mode vibrations determined by HVSR using either S-wave or entire

motion were around 1.8 Hz and 9.8 Hz for Terminus Dam.

(a)

(b)

Figure 9. HVSR results of earthquake data (gray line) along with the mean (solid line) and standard deviation (dashed line) of HVSR curves using entire motion at the main dam right crest (Loc5) in a) longitudinal and b) transverse directions.

Terminus Auxiliary Dam

We have also calculated HVSR in the longitudinal and transverse (upstream-downstream) direction of the auxiliary dam to determine the vibration characteristics (first (fundamental) and second mode) at center crest (Loc2). Figure 10a and b presents the HVSR results of 2 earthquake data (gray line) along with the logarithmic mean (solid line) and standard deviation (dashed line) of HVSR curves at the center crest (Loc2) in transverse and longitudinal directions using the intense part of the motions (S-wave). The first mode (fundamental) frequencies of the Terminus auxiliary dam are determined as 4 Hz and 3.6 Hz at center crest (Loc2) in longitudinal and transverse directions. The second mode of vibration was observed at 10.4 Hz at center crest (Loc 2) in longitudinal and transverse directions. The HVSR using the same set of earthquake motions are also calculated using the entire record. Figure 11a and b present the HVSR results of two earthquake data using entire records at the center crest (Loc2) in longitudinal and transverse directions. The first mode (fundamental) frequencies of the Terminus auxiliary dam are determined as 3.9 Hz and 5.1 Hz at center crest (Loc2) in longitudinal and transverse directions. The second mode of vibration was observed at 10.6 Hz at and 10.9 Hz at the center crest (Loc 2) in longitudinal transverse directions. The first (fundamental) and second mode vibrations as determined by HVSR using either S-wave or entire motion were around 3.8 Hz and 10.5 Hz for Terminus Dam.

(a)

(b)

Figure 10. HVSR results of earthquake data (gray line) along with the mean (solid line) and standard deviation (dashed line) of HVSR curves using S-wave at the auxiliary dam center crest (Loc2) a) longitudinal and b) transverse directions.

(a)

(b)

Figure 11. HVSR results of earthquake data (gray line) along with the mean (solid line) and standard deviation (dashed line) of HVSR curves using entire motion at the auxiliary dam center crest (Loc2) in a) longitudinal and b) transverse directions.

71

Crest to Abutment or Downstream Ratio

The ratio of Fourier amplitude spectrum of the records at crest (FFT_{crest}) to abutment ($FFT_{abutment}$) or downstream ($FFT_{downstream}$) records are calculated for Briones and Terminus dams at different locations (i.e., right crest, left crest, etc.). After calculating crest to abutment ratios for each event the mean and standard deviation are calculated similarly described for HVSR in equations 1 and 2. The resonant frequencies of dam are defined as the peak frequencies of the average crest to abutment or downstream curve.

Briones Dam

The ratio of crest to abutment records are calculated for Briones Dam at each sensor location: center and left crest (Loc2 and Loc3, see Figure 1) in longitudinal and transverse directions. The site conditions at the abutment site are not known, however the HVSR results at the abutment site show no low-frequency peaks as expected for a rock site, hence they are used as a reference site. The FAS ratio of the crest records (Loc2&3) to the abutment records (Loc1) (e.g. $FAS_{H,Loc2}/FAS_{H,Loc1}$ and $FAS_{H,Loc3}/FAS_{H,Loc1}$) are calculated for 16 earthquake events recorded at Briones Dam. Figures 12a-b and c-d present crest to abutment ratio results of 16 earthquake data along with the logarithmic mean and standard deviation at center crest ($FAS_{H,Loc2}/FAS_{H,Loc1}$) and left crest ($FAS_{H,Loc3}/FAS_{H,Loc1}$) in longitudinal and transverse directions, respectively. The first peak frequencies are determined as 1.2 and 1.3 Hz at center crest (Loc2) in longitudinal and transverse directions respectively and less clear peaks at 1.2 Hz and 1.4 Hz at left crest (Loc3). The second peak was observed at 5.5 Hz and 3.0 Hz at center crest (Loc 2) in longitudinal and transverse directions whereas second mode peaks were observed at 3.0 Hz and 3.4 Hz at left crest (Loc3) in longitudinal and transverse directions respectively.
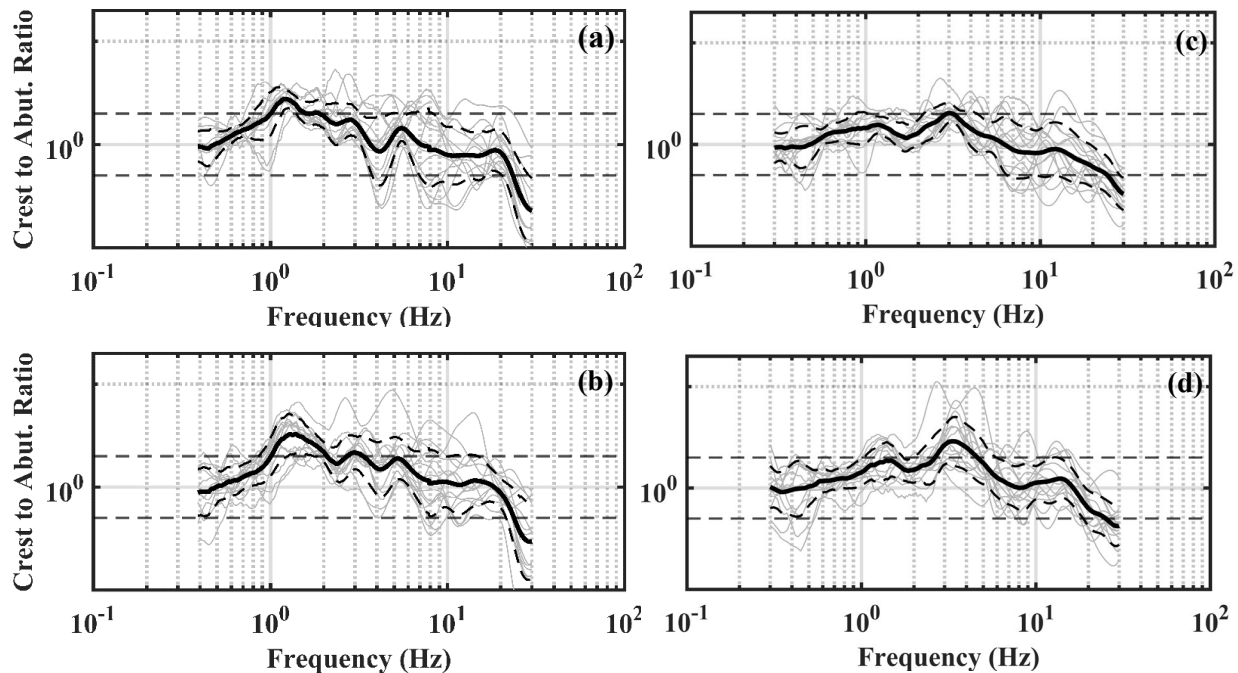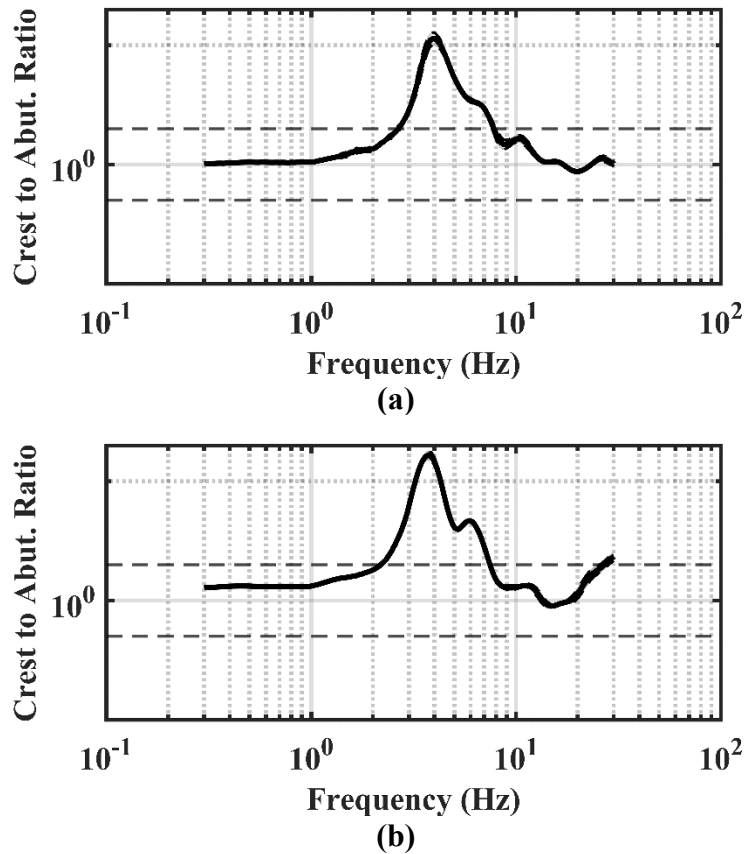

Figure 12. Crest to abutment ratio results of 16 earthquake data along with the mean and standard deviation at a) center crest (Loc2) in longitudinal and b) transverse directions, c) left crest (Loc3) in longitudinal and d) transverse directions.

Terminus Main Dam

The ratio of crest to abutment or downstream records are calculated for Terminus Dam at right crest (Loc5, see Figure 2) in longitudinal and transverse directions. The FAS ratio of the right crest records (Loc5) to the right abutment records (Loc4) (e.g. $FAS_{H,Loc5}/FAS_{H,Loc4}$) and crest to downstream ratio which is ratio of the right crest records (Loc5) to the downstream records (Loc3) (e.g. $FAS_{H,Loc5}/FAS_{H,Loc3}$) are calculated for the two recorded events. Figures 13a and b present right crest to abutment ratio results at right crest in longitudinal and transverse directions, respectively. The first peak frequencies are determined as 2 Hz at center crest (Loc5) in longitudinal and transverse directions respectively. No clear second peaks were observed when assessing crest to abutment ratios at Terminus Dam except a second peak around 10 Hz in transverse directions. Similarly crest to downstream ratios presented in Figure 13 c and d indicated first peak around 2 Hz in both directions with no clear second peak at right crest.
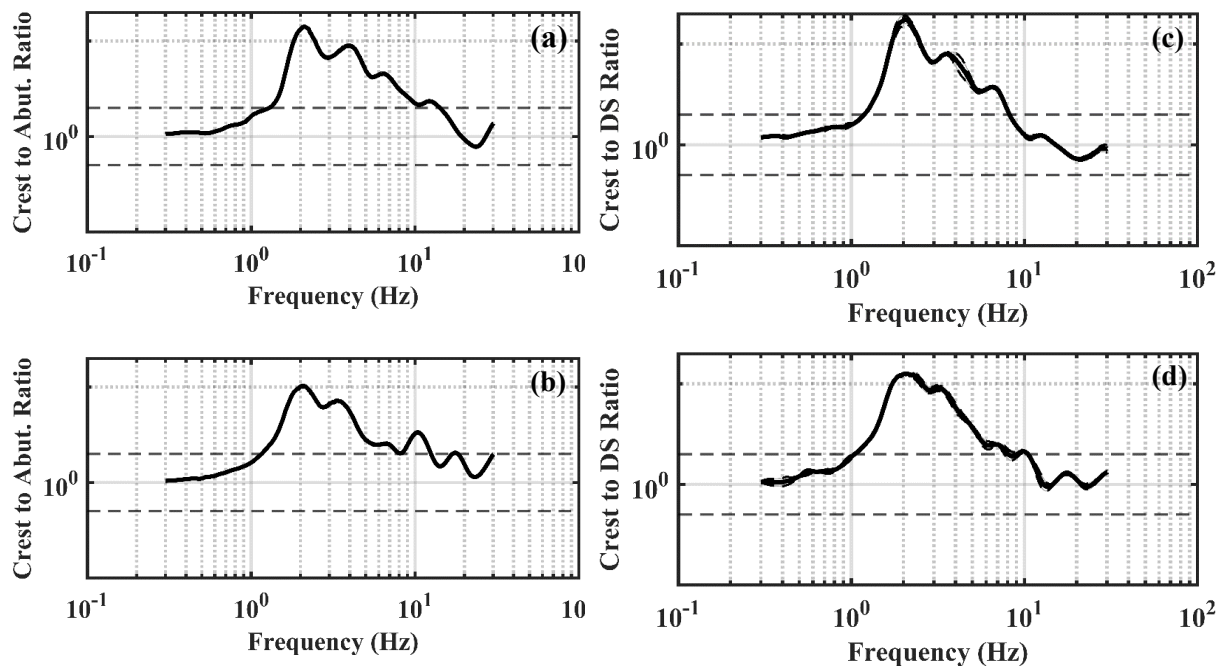
Figure 13. Crest to abutment ratio results of 2 earthquake data at a) right crest (Loc5) in longitudinal and b) transverse directions and crest to downstream ratio results of 2 earthquake data along with the mean and standard deviation at c) right crest (Loc5) in longitudinal and d) transverse directions.

Terminus Auxiliary Dam

Crest to abutment ratios are calculated as explained in the previous sections for Terminus auxiliary dam center crest (Loc2) ($FAS_{H,Loc2}/FAS_{H,Loc1}$) for 2 earthquake events as shown in Figure 14a and b. The first peak frequencies are observed around 4 Hz at center crest (Loc 2) in longitudinal and transverse directions with no secondary peaks.

(a)

(b)

Figure 14. Crest to abutment ratio results of 2 earthquake data along with the mean and standard deviation at a) center crest (Loc2) in longitudinal and b) transverse directions.

Interpretation of Results and Comparison with Available Literature

Table 3 presents the first and second mode frequency values obtained for Briones Dam's center crest and left crest locations in transverse and longitudinal direction with respect to dam body. HVSR using S_{wave} and entire records and crest to abutment ratios at center crest (Loc 2) of Briones Dam in transverse and longitudinal directions indicate similar first mode frequencies ranges 1.0-1.3 Hz. Second mode frequencies are determined as 4.7-6.1 Hz from HVSR results and 3.0-5.5 Hz from crest to abutment ratio. At left crest location (Loc3) first peak observed around 0.9-1.4 Hz for Briones Dam. Second mode frequencies are determined as 3.6-3.7 Hz from HVSR results and 3.0-3.4 Hz from crest to abutment ratio at left crest.

Table 4 presents the first and second mode frequency values obtained at main and auxiliary Terminus Dams' crest locations in transverse and longitudinal direction with respect to dam body. HVSR using S_{wave} and entire record and crest to abutment or downstream ratios at Terminus main dam right crest (Loc 5) in transverse and longitudinal directions indicate similar first mode frequencies ranges 1.7-1.9 Hz and from crest to abutment/downstream ratio as 1.9-2.2 Hz. Second mode frequencies at the same location are determined as 9.6-10 Hz from HVSR results and no second mode peaks were observed from crest to abutment ratio. HVSR using S_{wave} and entire record and crest to abutment or downstream ratios at Terminus auxiliary dam center crest (Loc2) in transverse and longitudinal directions indicate similar first mode frequencies

ranges 3.5-4.0 Hz. Second mode frequencies at the same location are determined as 10.4-10.9 Hz from HVSR results and no second mode peaks were observed from crest to abutment ratio.

Table 3. Fundamental and second mode frequency values obtained by different methods in Briones Dam at center and left crest.

Method	Direction	Freq. (Hz) Center crest (Loc2)	Freq. (Hz) Left Crest (Loc3)
HVSR$_\text{S-wave}$	Longitudinal	1.2/6.1	0.9/3.6
	Transverse	1.0/4.7	0.9/3.7
HVSR$_\text{entire}$	Longitudinal	1.2/5.9	0.9/3.6
	Transverse	1.0/*	0.9/3.6
Crest/Abutment ratio	Longitudinal	1.2/5.5	1.2*/3.0
	Transverse	1.3/3.0	1.4*/3.4

Table 4. Fundamental and second mode frequency values obtained by different methods in Terminus Dams at right and center crest.

Method	Direction	Freq. (Hz) Main Dam Right Crest (Loc5)	Freq. (Hz) Aux. Dam Center Crest (Loc2)
HVSR$_\text{S-wave}$	Longitudinal	1.9/9.6	4.0/10.4
	Transverse	1.7/9.8	3.6/10.4
HVSR$_\text{entire}$	Longitudinal	1.9/*	3.9/10.6
	Transverse	1.7/10	3.5/10.9
Crest/Downstream ratio	Longitudinal	1.9/*	NA
	Transverse	2.2/*	NA
Crest/Abutment ratio	Longitudinal	2.2/*	4.0/*
	Transverse	2.0/*	4.0/*

Note: Fundamental vibration frequency/ Second mode of vibration, *no clear peak.

Figures 15a and b present a comparison of first mode frequency from HVSR results using S-wave versus entire motion in longitudinal and transverse directions for dams. As can be inferred from the figure, for the selected dam location HVSR result at crest sensors using either S-wave or entire motion resulted in similar first mode frequency peaks.
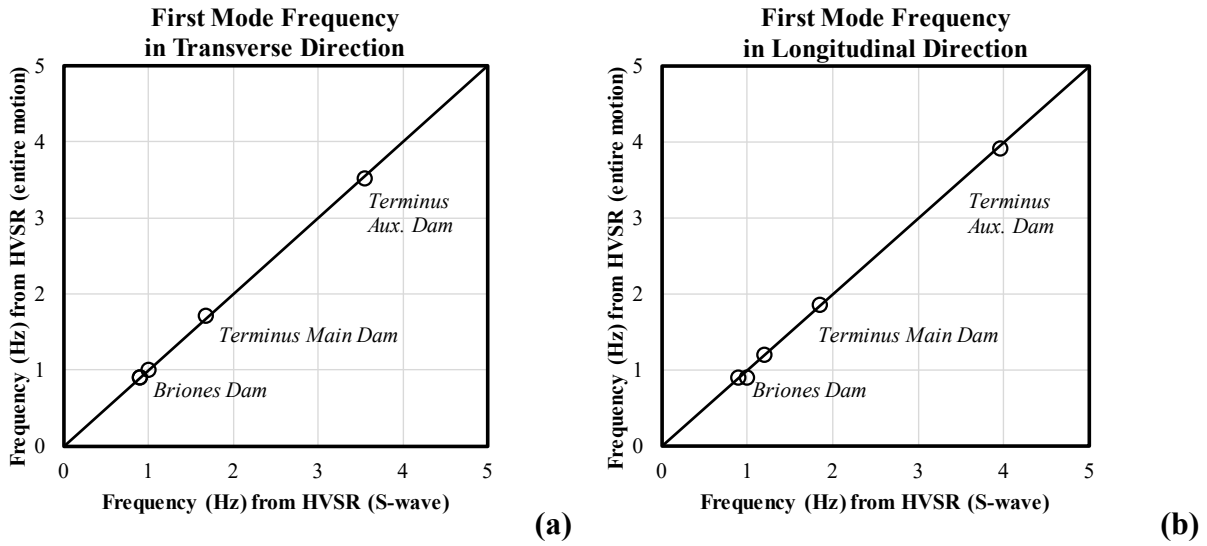
Figure 15. Comparison of first mode frequency from HVSR results using S-wave versus entire motion in a) longitudinal and b) transverse directions for dams.

Figures 16a and b present a comparison of first mode frequency from HVSR results using S-wave versus crest to abutment ratio in longitudinal and transverse directions for dams. As can be inferred from the figure, for the selected dam location HVSR result and crest to abutment ratio resulted in similar first mode frequency peaks.
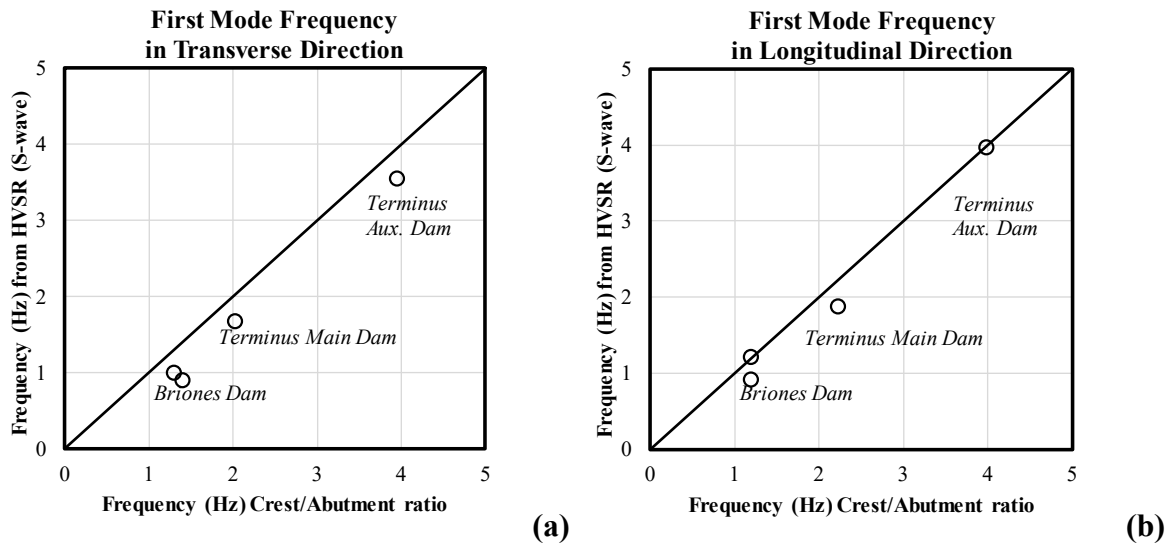
Figure 16. Comparison of first mode frequency from HVSR results using S-wave versus crest to abutment ratio in a) longitudinal and b) transverse directions for dams.

Gazetas (1987) showed that dams built in narrow canyons behave stiffer than those built in wide canyons. Their work provides recommendation of the stiffening effect of a narrow canyon on the fundamental natural as a function of L/H which is the aspect ratio. Figure 17 a-d presents L/H versus first and second mode frequency in transverse and longitudinal directions for Briones and Terminus dams along with data from Hwang et al (2008), Verret and LeBoeuf

(2021), Zimmaro and Ausilio (2020). Hwang et al (2008) studied the ratio of the Fourier amplitude spectrum and the response spectrum of the records from the crest to the downhole analyzing more than 30 events at each dam. The result of fundamental frequency of 5 dams with different aspect ratio in longitudinal and transverse directions are presented. Verret and LeBoeuf (2021) studied the vibration characteristics of Farneto del Principe Dam by various methods (e.g ambient noise measurements, shear beam methods, numerical analysis, analyzing recorded earthquake motion). Lastly, Zimmaro and Ausilio (2020) studied the vibration characteristics of Farneto del Principe Dam by performing finite element analysis and compare their results with other methods (e.g. shear beam method, etc.).
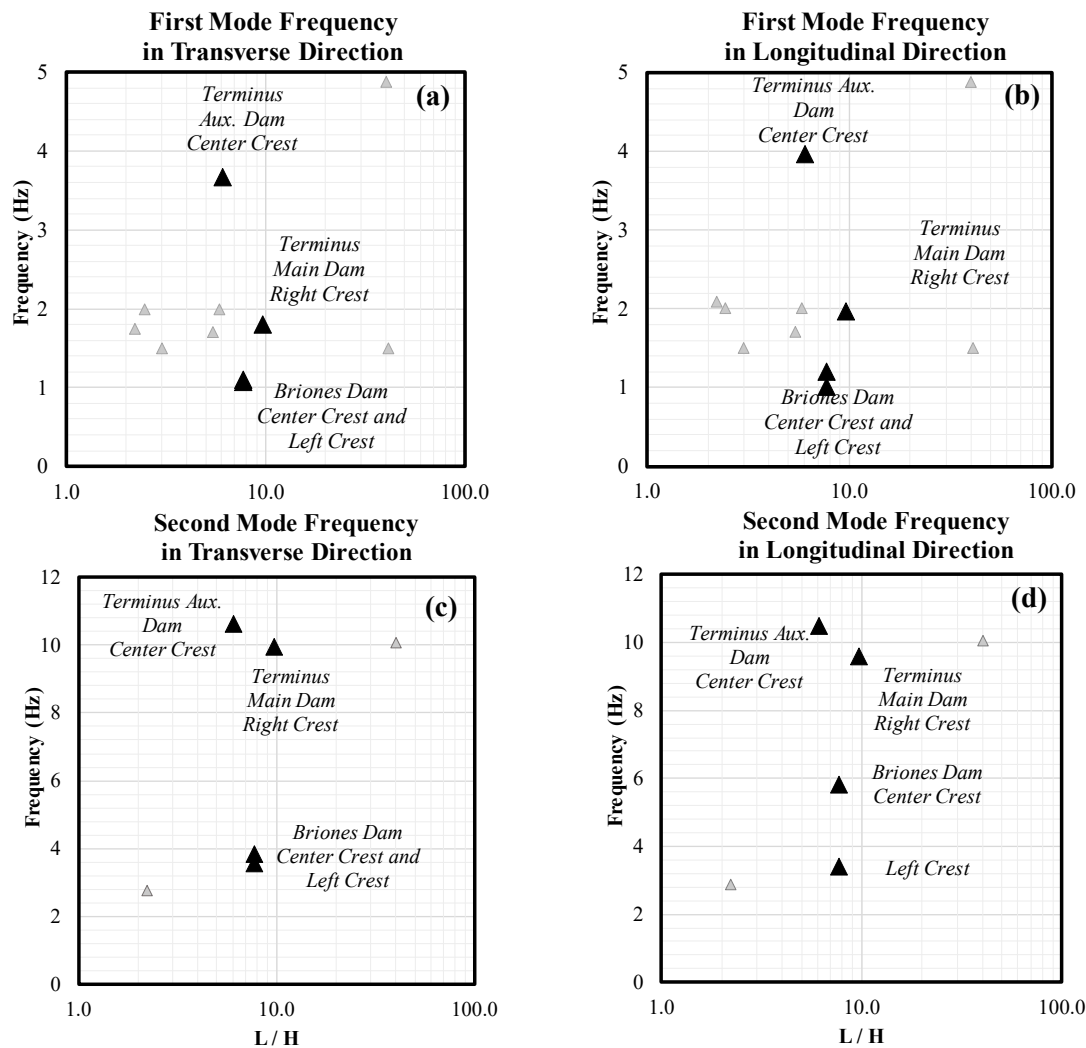
Figure 17. Summary of L/H versus frequency for selected dams in this study along with data from Hwang et al (2008), Verret and LeBoeuf (2021), Zimmaro and Ausilio (2020) a) first mode in transverse direction, b) first mode in longitudinal direction, c) second mode in transverse direction, d) second mode in longitudinal direction.

It can be concluded that the scatter in Figure 17 is wide as the first and second mode of the dams are examined for different aspect ratios. The vibration characteristics of dams (their natural periods and modal shapes) are affected by various factors which can be the reason behind

the large scatter. The effect of canyon geometry, dam height and crest length, aspect ratio (L/H), the inclination of the two sloping faces, inhomogeneous dam materials, shear modulus and damping properties of dam material, the stiffness characteristics of the foundation materials, dam-reservoir interaction, level of nonlinearity under earthquake loading, directional effects (different vibration modes in upstream-downstream and longitudinal direction) are the factors that control the dynamic behavior of dams. The earthquake recordings that are used in this paper having peak accelerations less than 0.20g hence provides the assessment of fundamental behavior of dams. However, the dynamic analysis of dams requires a good understanding of the in-situ conditions and information on dam and foundation materials which is lacking for Briones and Terminus Dams. Although some of the aspects are still investigated, the comparison of first mode (fundamental) and second mode frequencies derived analyzing the low intensity events using HVSR and crest to abutment ratio provides comparable and promising results to evaluate the dynamic behavior of dams with simple methods. The effect of aspect ratio and other parameters on first and second mode frequency are currently studied for additional case histories and conclusions will be the scope of a future study.

Conclusions

The availability of the earthquake recordings at Briones and Terminus Dam provides an opportunity to assess the dynamic characteristics of the dam. Several different approaches were studied to assess the first and second mode frequency of the dam by comparing HVSRs. The comparison provides promising results to evaluate the dynamic behavior of dams with simple methods. Availability of a more detailed subsurface characterization as well as field measurements are needed before specific recommendations are formulated.

Acknowledgements

References

1) Borcherdt, Roger D. (1970). Effects of local geology on ground motion near San Francisco Bay. *Bulletin of the Seismological Society of America* 60.1: 29-61.
2) Gazetas, G. (1987). Seismic response of earth dams: some recent developments. Soil dynamics and earthquake engineering, 6(1), 2-47.
3) Hassani, B., Yong, A., Atkinson, G. M., Feng, T., & Meng, L. (2019). Comparison of site dominant frequency from earthquake and microseismic data in California. *Bulletin of the Seismological Society of America*, 109(3), 1034-1040.
4) Hwang, J. H., Wu, C. P., & Chou, J. T. (2008). Motion characteristics of compacted earth dams under small earthquake excitations in Taiwan. In Geotechnical Earthquake Engineering and Soil Dynamics IV (pp. 1-12).
5) Kawase, H., Sánchez-Sesma, F. J., & Matsushima, S. (2011). The optimal use of horizontal-to-vertical spectral ratios of earthquake motions for velocity inversions based on diffuse-field theory for plane waves. *Bulletin of the Seismological Society of America*, 101(5), 2001-2014.
6) Kishida, T., Ktenidou, O. J., Darragh, R. B., & Walter, S. (2016). Semi-automated procedure for windowing time series and computing Fourier amplitude spectra (FAS) for the NGA-West2 database.
7) Konno, K. and Ohmachi, T., (1998). Ground-motion characteristics estimated from spectral

ratio between horizontal and vertical components of microtremor, *Bull. seism. Soc. Am.*, 88, 228–241.

8) Ktenidou, O. J., Chávez-García, F. J., Raptakis, D., & Pitilakis, K. D. (2015). Directional dependence of site effects observed near a basin edge at Aegion, Greece. *Bulletin of Earthquake Engineering,* 14, 623-645.

9) Lermo, J., and Chávez-García, F. J. (1993). Site effect evaluation using spectral ratios with only one station. *Bull. of the seismological society of America*, 83(5), 1574-1594.

10) Nakamura, Y., (1989), "A method for dynamic characteristics estimation of subsurface using microtremor on the ground surface", *QR of Railway Technical Research Institute*, Vol 30, pp. 25-33.

11) Nakamura, Y., (1996). Real-time information systems for hazards mitigation, *Proceedings of the 11th World Conference on Earthquake Engineering*, Acapulco, Mexico.

12) Nakamura, Y., (2000). Clear identification of fundamental idea of Nakamura's technique and its applications, *Proceedings of the 12th World Conference on Earthquake Engineering,* Auckland, New Zealand.

13) Nogoshi, M. and Igarashi, T. (1970). On the propagation characteristics of microtremors. *J. Seism. Soc.* Japan 23, 264-280 (in Japanese with English abstract).

14) Nogoshi, M. and Igarashi, T. (1971). On the amplitude characteristics of microtremors. *J. Seism. Soc*. Japan. 24, 24-40 (in Japanese with English abstract).

15) Verret, D., & LeBoeuf, D. (2022). Dynamic characteristics assessment of the Denis-Perron dam (SM-3) based on ambient noise measurements. Earthquake Engineering & Structural Dynamics, 51(3), 569-587

16) Zhu, C., Cotton, F., & Pilz, M. (2020). Detecting site resonant frequency using HVSR: Fourier versus response spectrum and the first versus the highest peak frequency. *Bull. of the Seismological Society of America*, 110(2), 427-440.

17) Zimmaro, P., & Ausilio, E. (2020). Numerical evaluation of natural periods and mode shapes of earth dams for probabilistic seismic hazard analysis applications. Geosciences, 10(12), 499.

CALIBRATION OF THE NEAR-SURFACE SEISMIC STRUCTURE IN THE SCEC COMMUNITY VELOCITY MODEL VERSION S

Kim Olsen and Te-Yang Yeh

Department of Earth and Environmental Sciences
San Diego State University

Abstract

We have estimated the thickness distribution of a geotechnical layer in the SCEC CVM-S4.26M01 (updated with recent ambient noise results) that generates the least-biased fit between 3D 0-1 Hz physics-based ground motion simulations and strong motion data in the greater Los Angeles area, CA, for 7 M_w4.4-5.4 earthquakes. Outside the basins, the optimal GTL thickness distribution shows strong spatial variation, generally increasing from near 0 m at the edges of the basins to values of 1,000 m or larger at distances of about 10-50 km, in particular toward the northeast, east and southeast.

Introduction

The near-surface seismic structure to a depth of about 1,000 m, particularly the shear-wave velocity (V_s), can strongly affect the propagation of seismic waves, and therefore must be accurately calibrated for ground motion simulations used in seismic hazard assessment. The V_s structure of the material deeper than about 1,000 m are typically reasonably-well determined by tomography studies. However, at shallower depths, when constraints are missing from borehole studies, geotechnical measurements, and water and oil wells, typically at rock sites outside the sedimentary basins, the material parameters are often poorly characterized.

When the alluded geological constraints are not available, models, such as the Statewide California Earthquake Center (SCEC) Community Velocity Models (CVMs), default to regional tomographic estimates that do not resolve the uppermost V_s values, and therefore deliver unrealistically high shallow V_s estimates. The SCEC Unified Community Velocity model (UCVM) software includes a method to incorporate the near-surface earth structure by applying a generic overlay based on measurements of time-averaged V_s in the top 30 m (V_{s30}) to taper the upper part of the model to merge with tomography at a depth of 350 m, which can be applied to any of the velocity models accessible through UCVM. However, Hu et al. (2022) used 3D deterministic simulations in the Los Angeles area with the SCEC CVM-S4.26.M01 model to show that low-frequency (< 1 Hz) ground motions at sites where the material properties in the top 350 m are modified by the generic overlay ("taper") significantly underpredict those from the 2014 M_w5.1 La Habra earthquake. On the other hand, Hu et al. (2022) showed that extending the V_{s30}-based taper of the shallow velocities to a depth of 700-1,000 meters improved the fit between their synthetics and seismic data at those sites significantly, without compromising the fit at well constrained sites.

In addition to recommending that the taper depth be extended, Hu al. (2022) also proposed further work. Specifically, they suggested that their results be checked using additional ground motion metrics, and including multiple earthquakes generating waves propagating into the basins from different azimuths, which has been shown to affect amplification patterns (Olsen, 2000). Moreover, although they found improvements using a uniform tapering depth, they observed some spatial variabilities that, if accounted for, may further improve their method. Here, we further analyze the near-surface velocities in the SCEC CVM-S4.26.M01 outside the greater Los Angeles basins, with the goal of improving the fit between synthetic and observed seismic data. Toward this goal, we simulate 0-1 Hz physics-based wave propagation for 7 well-recorded events with magnitudes between 4.4 and 5.4 and varying azimuth with respect to the Los Angeles area (see Figure 1), and estimate a spatially-variable distribution of optimal tapering depths outside the sedimentary basins. Finally, we assess the how well the long-period ground motions were predicted in the sedimentary basins for the 7 events, and provide recommendations for further work.
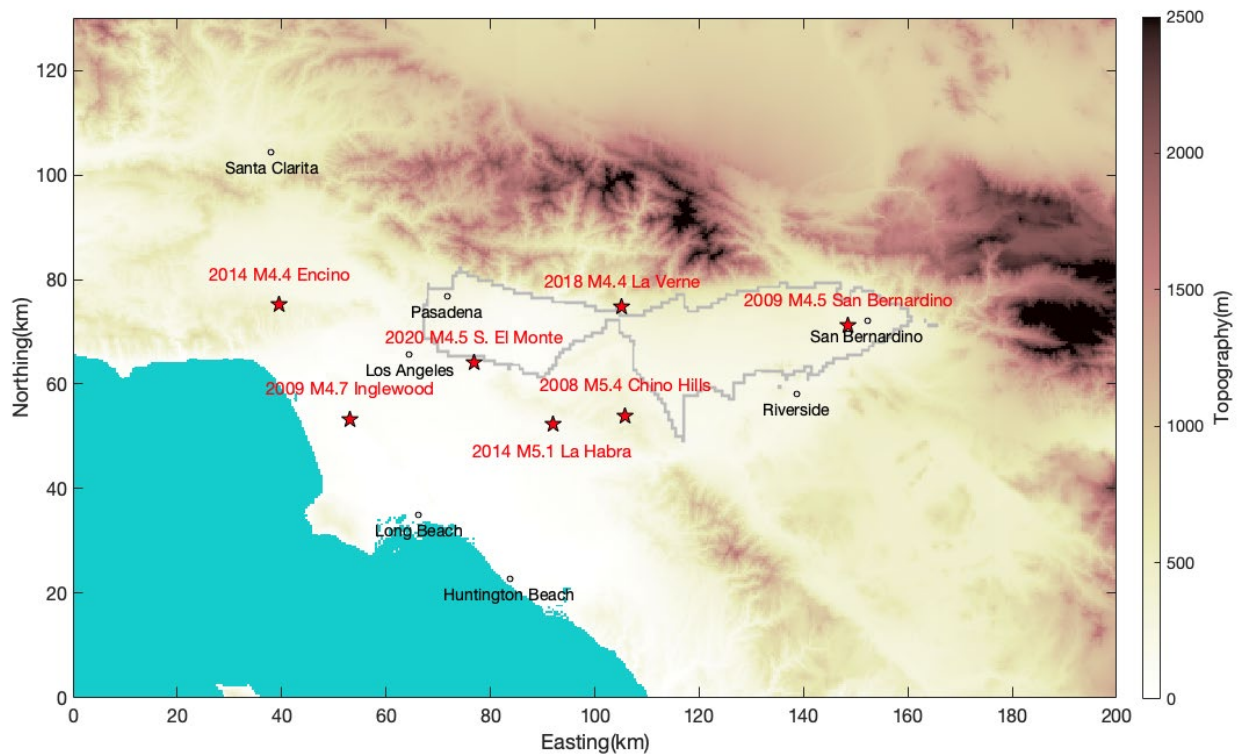
Figure 1. Map showing the simulation domain and locations of the events included in this study. The thick gray line depicts the boundary of the SGSB model imaged by Li et al. (2023).

Numerical Method

We use the 4th-order accurate finite-difference code AWP-ODC (Cui et al., 2010) for our simulations. In order to reduce the computational cost, we used 3 velocity meshes separated vertically with a factor-of-three increase in grid spacing with depth via a discontinuous mesh approach (Nie et al., 2017). Topography is modeled used the curvilinear grid approach by O'Reilly et al. (2022).

Table 1 provides details of the numerical simulations. We used a minimum shear wave velocity of 180 m/s in the top block, ensuring at least 6.7 points per minimum wavelength (O'Reilly et al., 2022).

Velocity and Anelastic Attenuation Model

Our target reference model in this study is the SCEC CVM version 4.26-M01 (CVM-S in the following, Small et al., 2017). We extract a domain of dimensions 200 km (X) x 130 km (Y) x 100 km (Z), covering the entire Los Angeles basin (LAB), San Fernando basin (SFB), San Gabriel basin (SGB), Chino basin (CB), and San Bernardino basin (SBB), as well as the surrounding areas (Figure 1). Following Olsen et al. (2003), we assume $Q_{s,0}$ to be proportional to the local S-wave speed, $Q_{s,0} = kV_s$, where k is a parameter specific to the study area. We adopt the same model as Hu et al. (2022) for the anelastic attenuation, namely $Q_s=0.1V_s$ (V_s in m/s) and $Q_p=2Q_s$.

Goodness-of-fit (GOF) Measure

We use the Fourier amplitude spectral (FAS) bias as a quantification of model performance, defined as

$$FAS_{bias}(f) = log_{10}\frac{FAS_{model}(f)}{FAS_{data}(f)},$$

where $FAS_{model}(f)$ and $FAS_{data}(f)$ are the root-mean-squared horizontal spectra of the simulated and observed waveforms, respectively. Before computing the FAS bias, all spectra were smoothed using the Konno-Ohmachi method with a bandwidth of 40 (Konno and Ohmachi, 1998). Finally, we compute the mean of the FAS bias values over the frequency points between 0.3 - 1 Hz.

Table 1. Simulation parameters.

Model dimensions	Top mesh: 6,696 x 4,320 x 416 Middle mesh: 2,232 x 1,440 x 480 Bottom mesh: 744 x 480 x 160
Grid spacings	30 m: Free surface to 12.42 km depth 90 m: 12.21 km depth to 55.32 km depth 270 m: 54.69 km depth to 96.62 km depth
Minimum Vs	180 m/s
Maximum frequency	1 Hz
Timestep	0.0015 s
Simulated time length	100 s

Near-surface Geotechnical Layer (GTL)

We follow the approach of Hu et al. (2022) to calibrate the near-surface velocity structure within our model domain. This calibration entails replacing the velocity model extracted from the SCEC CVM-S, from the free surface to a given tapering depth (z_T) with V_S, V_p and density computed using the formulations of Ely et al. (2010) along with local V_{S30} information. This approach provides a smooth transition between the near-surface velocity structures and the original model. We used measured V_{S30} values wherever available, and the values from Thompson et al. (2018) elsewhere.

To implement the GTL, we use the taper function proposed by Ely et al. (2010), which considers the local V_{s30} value, given by

$$
\begin{aligned}
z &= z'/z_T \\
f(z) &= z + b(z - z^2) \\
g(z) &= a - az + c(z^2 + 2\sqrt{z} - 3z) \\
V_S(z) &= f(z)V_{ST} + g(z)V_{S30} \\
V_P(x) &= f(z)V_{PT} + g(z)P(V_{S30}) \\
\rho(z) &= R(V_P)
\end{aligned}
\qquad (1)
$$

where z is a normalized depth, z' is depth, z_T is a transition depth, and V_p and V_s are computed using linear combinations of $f(z)$ and $g(z)$ functions along with V_{PT} and V_{ST}, which are V_P and V_S, respectively, in the original model at z_T. P and R are functions used for the V_P scaling law from the Brocher (2005) and Nafe-Drake law, respectively. Here, we use the coefficients a=1/2, b=2/3, and c=3/2 in Eq. (1), consistent with Ely et al. (2010).

Due to the simplification in the formulation of Ely et al. (2010), the resulting V_{s30} of the V_s taper does not always match the input V_{s30} value. We corrected for this discrepancy in all models with the GTL implemented by replacing the V_s profile in the top 30 m with the re-scaled V_s profile for generic rock sites from Boore and Joyner (1997), defined as

$$
Vs_c(z) = (Vs_{BJ1997}(z)/617)V_{S30}, z < 30m \qquad (2)
$$

where V_{sc} is the corrected V_s profile, $V_{s\,BJ1997}$ is the V_s profile for generic rock sites from Boore and Joyner (1997), and V_{s30} is the targeted V_{s30} value to be matched. The scale factor (617 m/s) used here is the V_{s30} of $V_{s\,BJ1997}$, which is given by

$$
\begin{aligned}
Vs_{BJ1997}(z) &= 245m/s, z \leq 1m \\
Vs_{BJ1997}(z) &= 2206(z/1000)^{0.272}m/s, 1 < z \leq 30m,
\end{aligned}
\qquad (3)
$$

where the depth is in meters. To avoid creating a velocity contrast at 30 m depth, we linearly transition V_{sc} at 30 m [V_{sc} (30)] to the existing V_s at a depth of 60 m [V_{sc} (60)] that is,

$$Vs_c(z) = Vs_c(30) + \frac{Vs(60) - Vs_c(30)}{(60 - 30)}(z - 30), 30m \leq z \leq 60m. \text{ (4)}$$

V_p and density were computed from V_{sc} using empirical relations from Brocher (2005). Note that in the simulations with a grid spacing of 30 m, the velocities were computed by the harmonic average of velocity values within the depth range associated with each grid.

Ground Motion Simulations

We simulate 7 M_w4.4-5.4 events (2014 M_w4.4 Encino, 2009 M_w4.7 Inglewood, 2020 M_w4.5 South El Monte, 2018 M_w4.4 La Verne, 2009 M_w4.5 San Bernardino, M_w5.1 2014 La Habra, and the 2008 M_w5.4 Chino Hills earthquakes, see Fig. 1) to further calibrate the tapering depths in the greater Los Angeles area. The La Habra and Chino Hills events are simulated using the finite fault sources described in Hu et al. (2022) and Shao et al. (2012), respectively, while the remaining events (M_w4.4-4.7) are considered sufficiently small to be simulated using point sources for frequencies up to 1 Hz. All point sources use a Brune-type moment-rate function and a stress drop of 3 MPa.

We follow the approach of Hu et al. (2022) and classify site locations based on surface V_s in the original CVM-S into type A (surface $V_s \leq 1000$ m/s) and type B (surface $V_s > 1000$ m/s) sites. Figure 2 shows the location of the source and stations of types A and B.
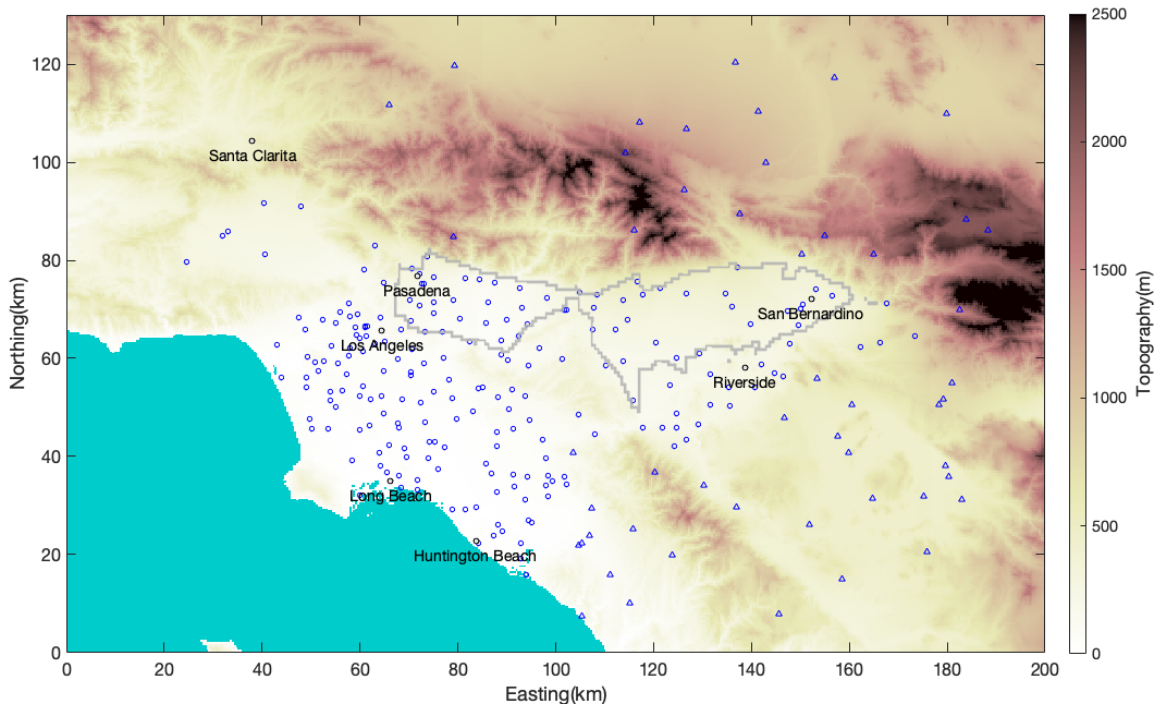
Figure 2. Locations of the stations (type A – surface $V_s < 1{,}000$ m/s, circles), type B – surface $V_s > 1{,}000$ m/s, triangles).

Update of SGB, CHB and SBB in CVM-S

First, we test whether a newer and higher-resolution shear wave velocity model for the SGB, CHB and the SBB constrained by ambient noise tomography (Li et al., 2023, hereafter labeled 'SGSB'), is able to improve the fit to observed ground motions for our test events. To ensure a smooth transition where two models intersect, we used the weighting approach from Ajala and Persaud (2021) with a 15 km-wide transition zone. As shown in Figure 3, the model imaged by Li et al. (2023) as expected increases the spatial resolution within the domain covered by the ambient noise imaging, particularly in the top 1 - 2 km, while the constraints on deeper structures (3+ km) from this model are mainly for the San Gabriel basin.

Figures 4-5 show the average bias for stations located above the SGSB model for the 7 events. The effects of the SGSB model update varies for the 7 events, with the largest improvements for the La Habra, Chino Hills and El Monte events, for frequencies 0.2-0.5 Hz (38% averaged for the 3 components). We therefore implement the SGSB model in the CVM-S reference model in the following tests.

Calibration of Spatial Variation of GTL Depths for Type B sites

Our next step is to reassess the bias at type B sites (surface V_s > 1,000 m/s) that Hu et al. (2022) analyzed for the 2014 M5.1 La Habra earthquake, for the 7 earthquakes shown in Figure 1. Figures 6-12 show interpolated areal distributions of the average FAS bias at all sites for 0-1 Hz ground motion simulations of the events, using tapering depths (z_T) of 0 m (no GTL), 150 m, 300 m, 600 m, 900 m and 1,200 m (42 simulations). The FAS bias maps show that type B sites are generally underpredicted without adding the GTL for all events, which is consistent with the findings from the La Habra simulations by Hu et al. (2022). Furthermore, Figures 13-14 show average bias values for frequencies between 0.2-1.0 Hz for each event for tapering depths of 0 m (no GTL), 600 m and 1,200 m. These results indicate that the optimal tapering depths for type B sites vary considerably spatially. For example, Figures 13-14 suggest that optimal tapering depth is relatively deep (1,000-1,200 m) for the La Habra, Inglewood and San Bernardino events and about 600 m for the El Monte earthquake, while the Chino Hills event favors a very shallow GTL (near 0 m). Note, that the small number of type B sites for the Encino event (5) and to some extent the Inglewood event (12) increases the uncertainty of estimating the optimal tapering layer.

With simulations of the 7 events, we evaluated the performance of different tapering depths based on the event-averaged FAS bias values at each site, denoted as $\overline{FAS_{bias}}$, given by

$$\overline{FAS_{bias}}(z_T) = \frac{\sum_{i=1}^{N_{evt}} FAS_{bias,i}(z_T)}{N_{evt}},$$

where N_{evt} is the number of events. Each site thus uses up to 7 FAS bias values for each tapering depth. The estimation of the optimal tapering depth at each site is then obtained by minimizing the absolute value of the event-averaged FAS bias ($|\overline{FAS_{bias}}(z_T)|$). To further improve our estimates, we discarded sites that only recorded a single event. Compiling all the best-fit tapering depths estimated at all the sites that qualify, we used an inverse-distance weighted interpolation to calculate a map that shows the spatially-varying tapering depth throughout our domain.
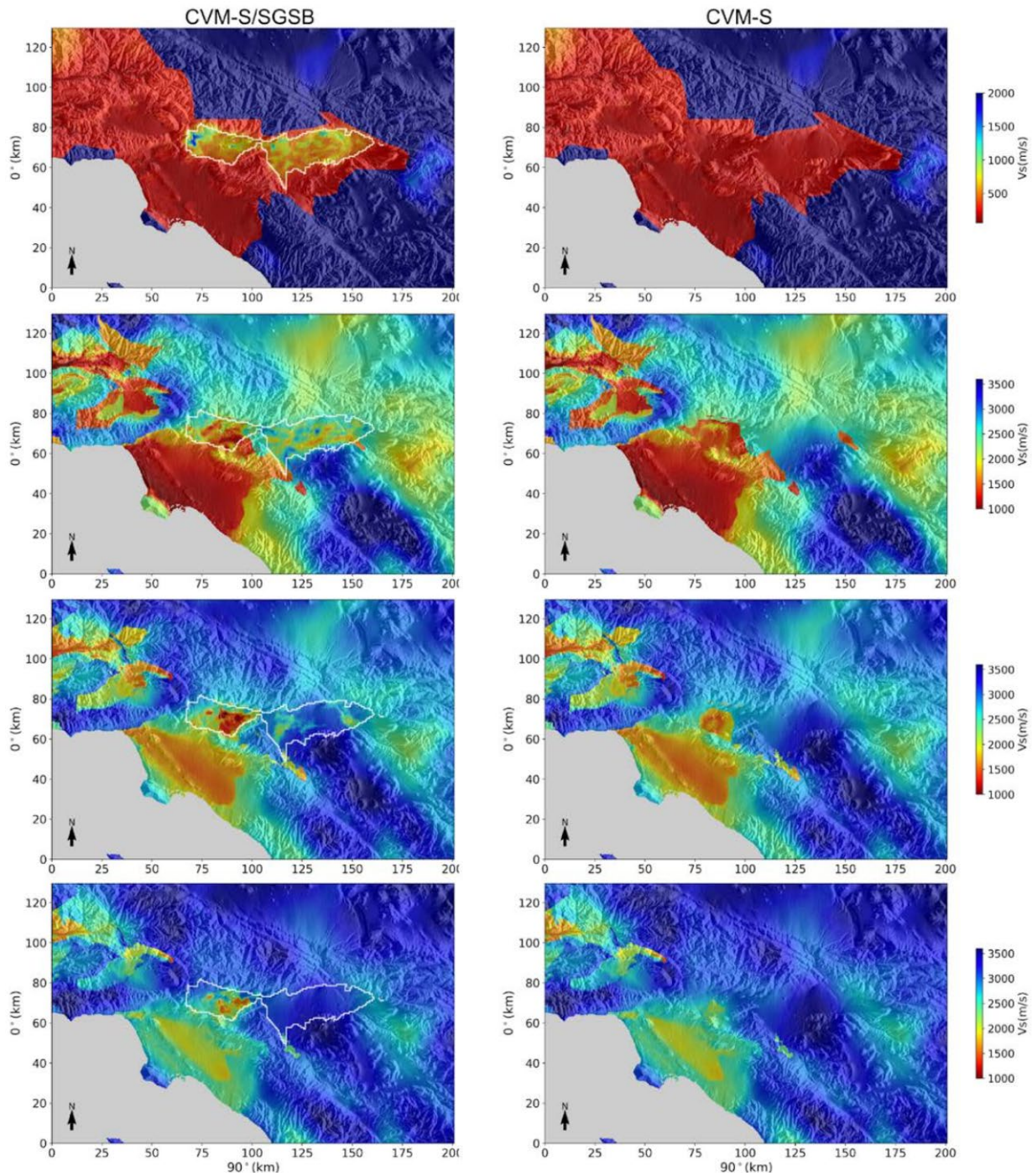
Figure 3. Horizontal slices of shear wave speeds at different depths extracted from the combined model (CVM-S/SGSB) and the original CVM-S. The white polygon in the CVM-S/SGSB model outlines the surface projection of the imaging domain of Li et al. (2023).
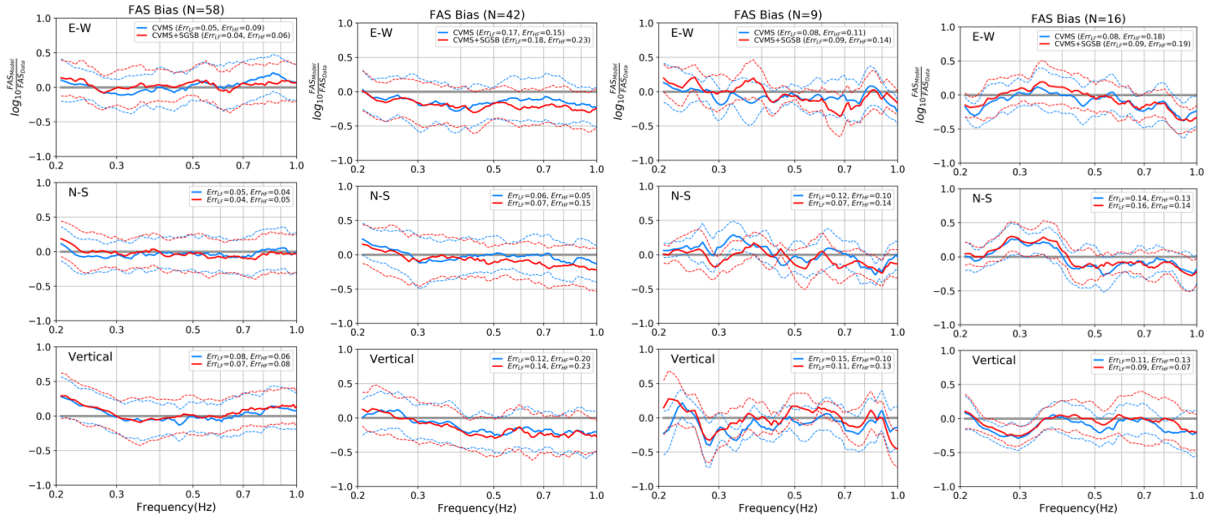
Figure 4. Comparisons of FAS bias curves derived from simulations with the original CVMSI (blue) and with CVMSI+SGSB (red), computed from all stations within the imaging domain of Li et al. (2023), for (left to right) the 2008 M_w5.4 Chino Hills, 2009 M_w4.5 San Bernardino, 2009 M_w4.7 Inglewood, and 2014 M_w4.4 Encino events. Err_{LF} and Err_{HF} depict the average bias for 0.2-0.5 Hz and 0.5-1.0 Hz, respectively.
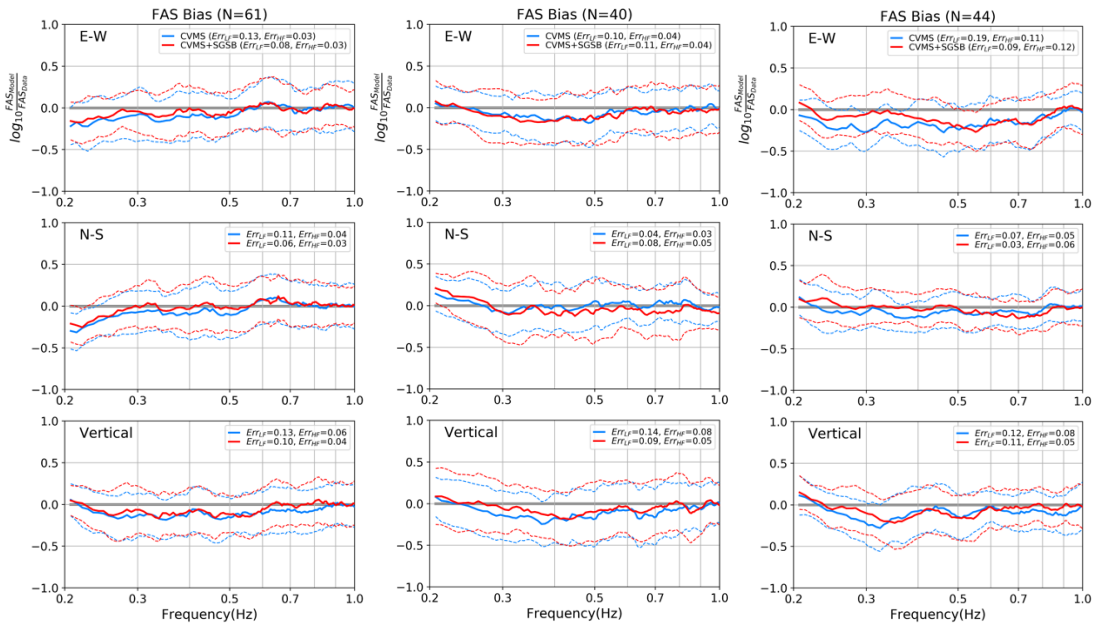
Figure 5. Same as Figure 4, but for (left to right) the 2014 M_w5.1 La Habra, 2018 M_w4.4 La Verne, and 2020 M_w4.5 South El Monte events.

Figure 15 shows the average optimal GTL tapering depth, inferred from the maps of average 0.3-1.0 Hz FAS combined for the 7 events shown in Figure 1, at the 348 sites with two or more measurements. For type B sites (triangles), as indicated by the individual events (Figures 6-12), the optimal tapering depth shows strong spatial variation. In general, the optimal tapering depths appear to increase away from the sedimentary basins, in particular toward the northeast, east and southeast.
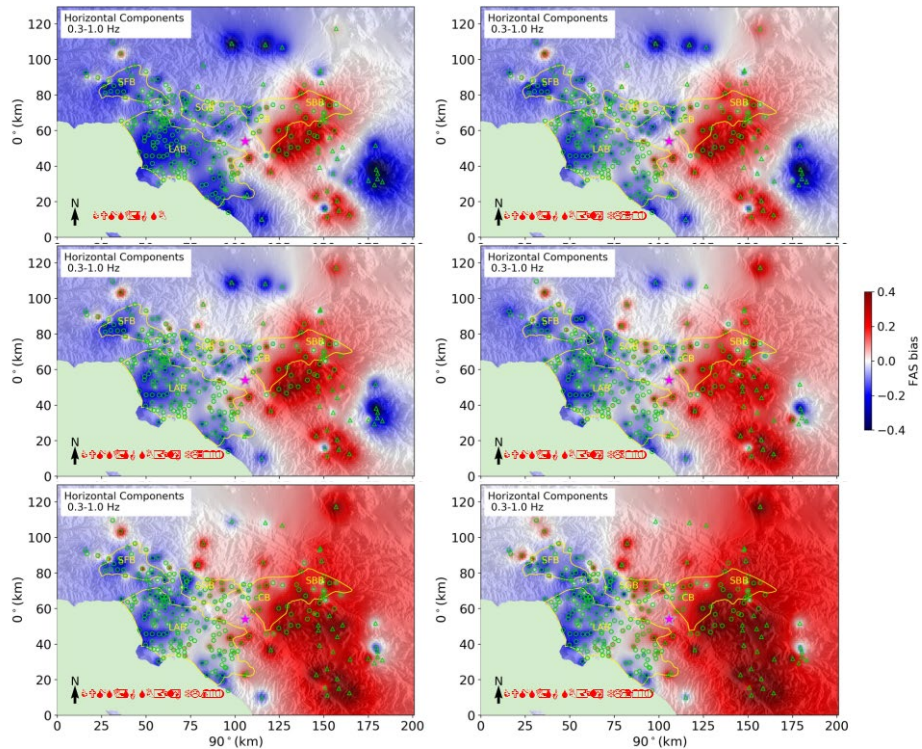
Figure 6. 0.3-1.0 Hz FAS bias at sites for the 2008 M_w5.4 Chino Hills earthquake with GTL depths of 0 m, 150 m, 300 m, 600 m, 900 m and 1200 m. The yellow lines depict approximate outlines of the SFB, LAB, SGB, CB, and SBB.
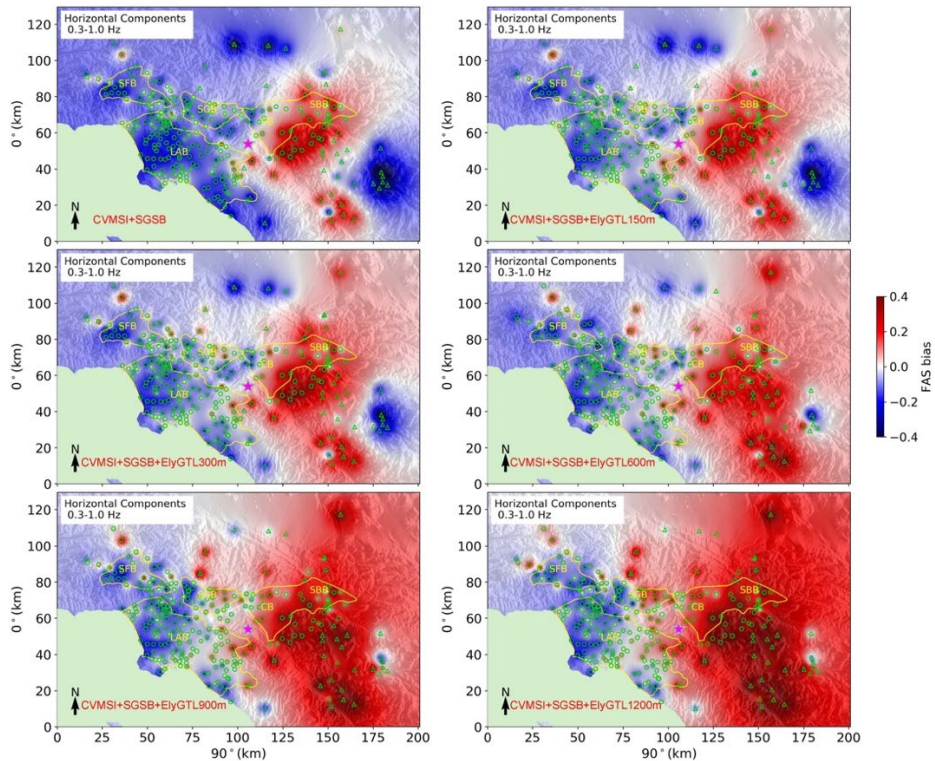
Figure 7. Same as Fig. 6, but for the 2009 M_w4.5 San Bernardino earthquake.
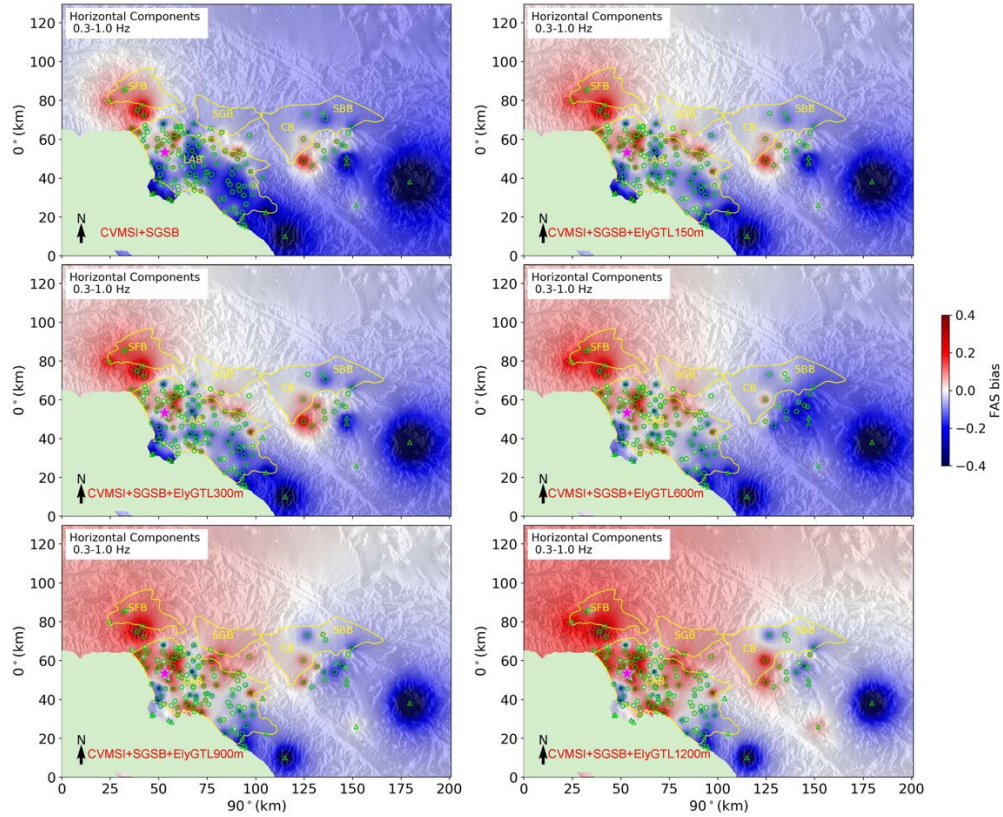
Figure 8. Same as Fig. 6, but for the 2009 M$_w$4.7 Inglewood earthquake.
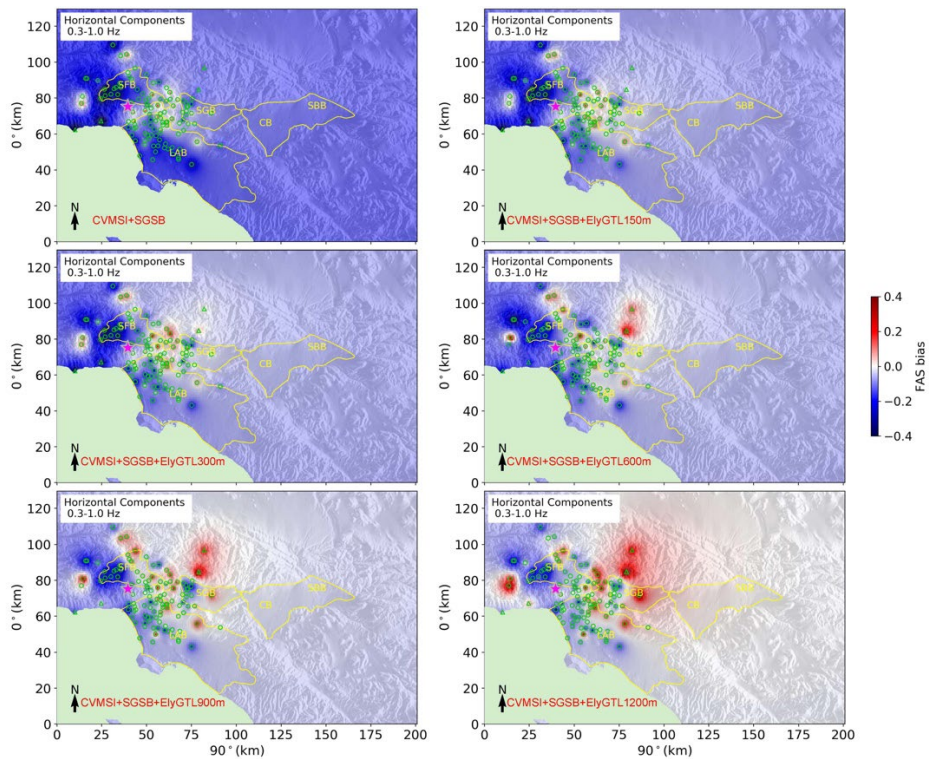
Figure 9. Same as Fig. 6, but for the 2014 M$_w$4.4 Encino earthquake.
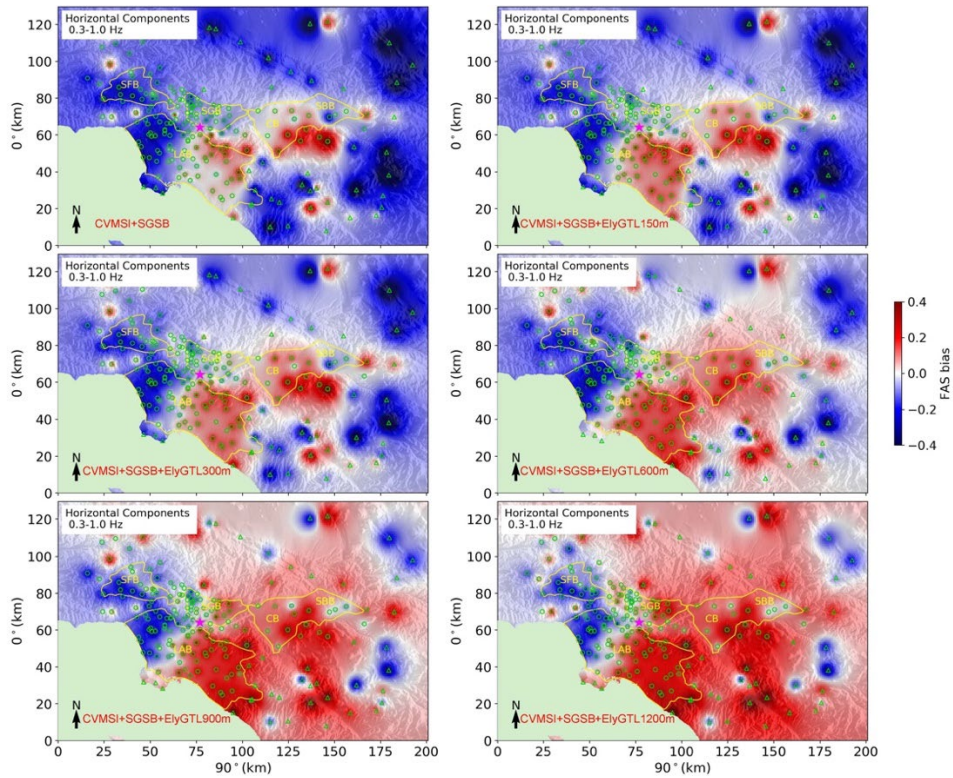
Figure 10. Same as Fig. 6, but for the 2014 M_w5.1 La Habra earthquake.
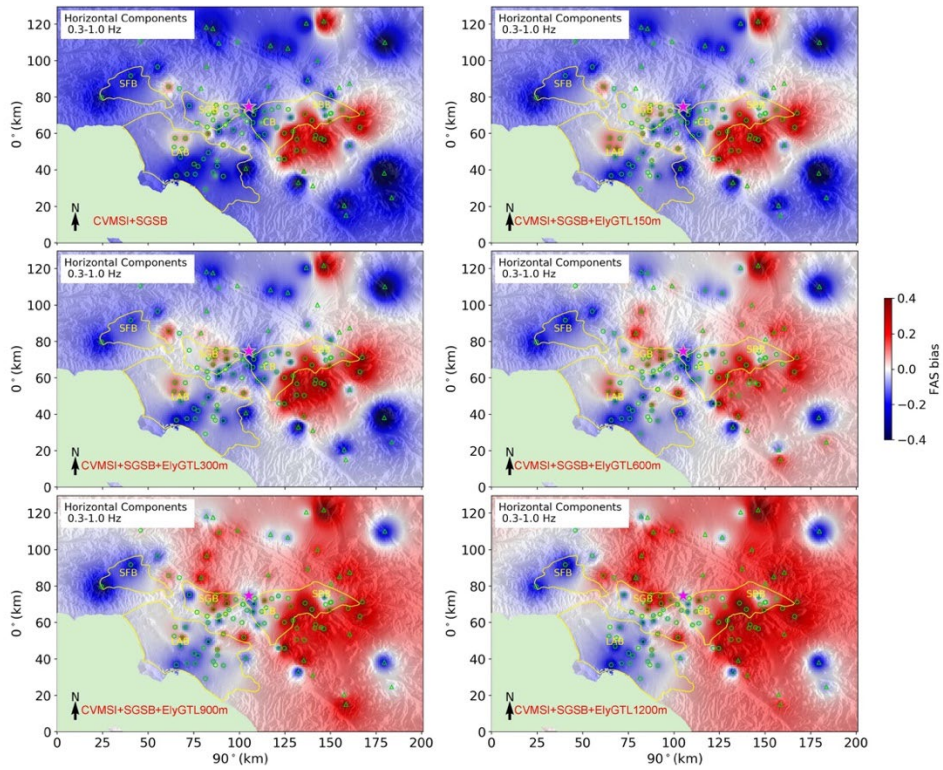
Figure 11. Same as Fig. 6, but for the 2018 M_w4.4 La Verne earthquake.
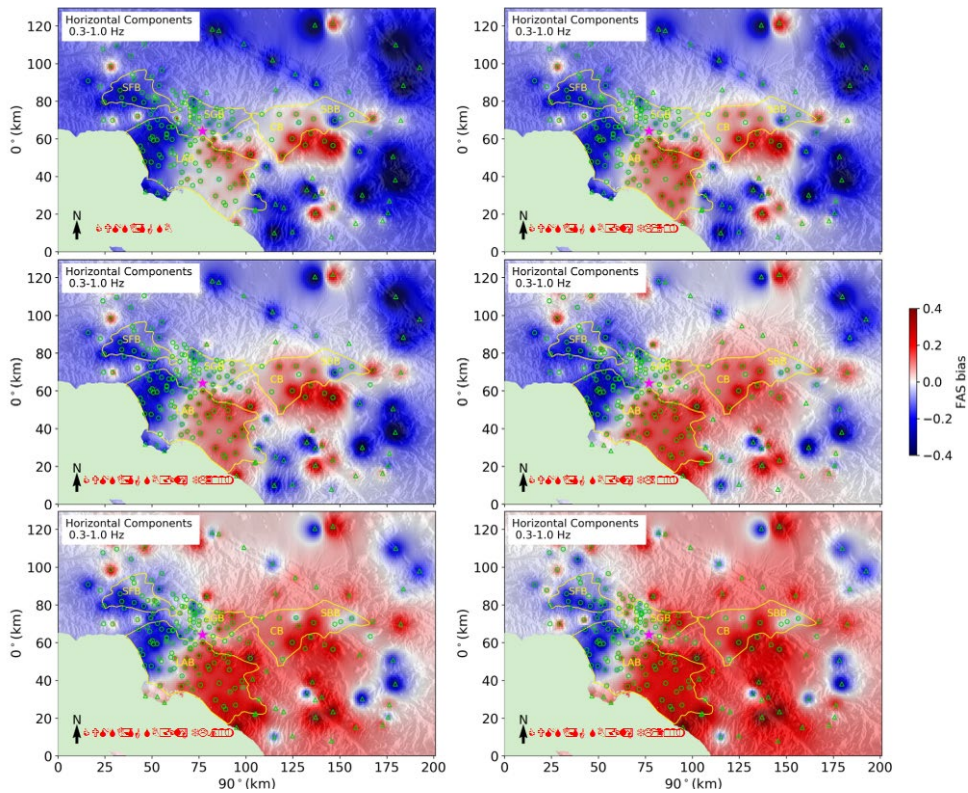
Figure 12. Same as Fig. 6, but for the 2020 M_w4.5 South El Monte earthquake.
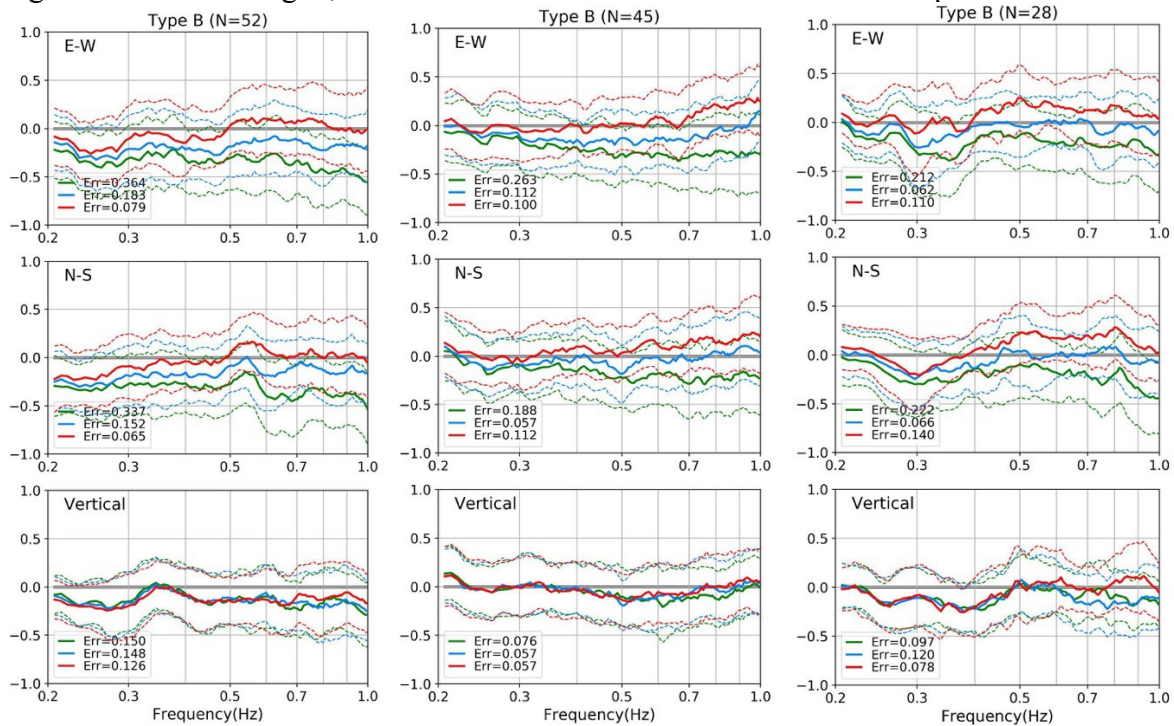
Figure 13. 0.2-1.0 Hz FAS bias at type B sites for (left to right) the 2014 M_w4.1 La Habra, the 2020 M_w4.5 South El Monte, and the 2018 M_w4.4 La Verne, CA, earthquakes with no GTL (green lines), a 600 m GTL (blue lines), and a 1200 m GTL (red lines). 'N' depicts the number of type B sites.
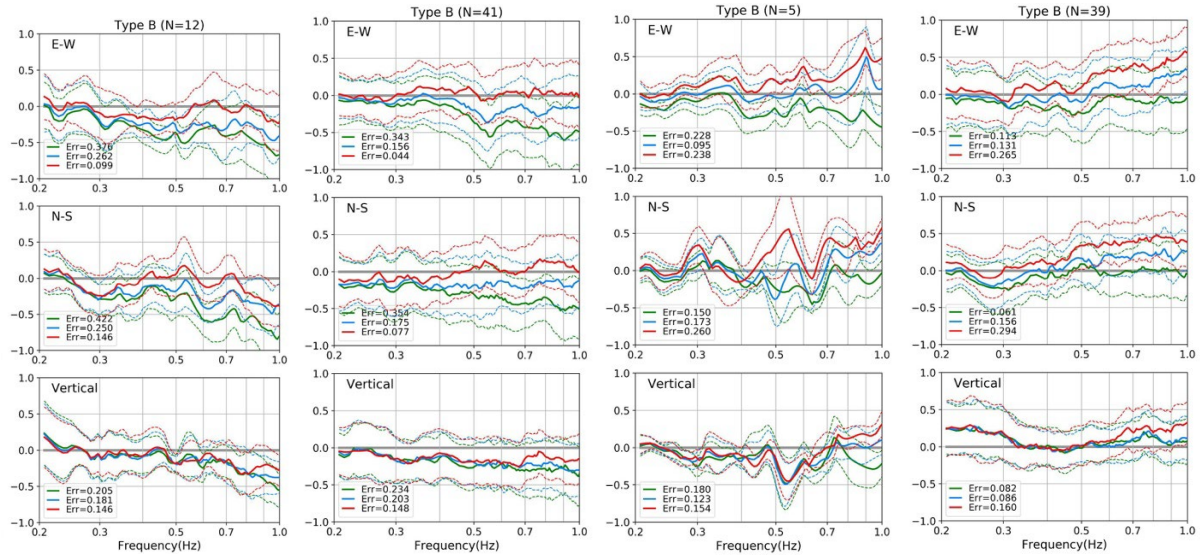
Figure 14. Same as Figure 13, but for (left to right) the 2009 M$_w$4.7 Inglewood, the 2009 M$_w$4.5 San Bernardino, the 2014 M$_w$4.4 Encino, and the 2008 M$_w$5.4 Chino Hills earthquake, CA, earthquakes.
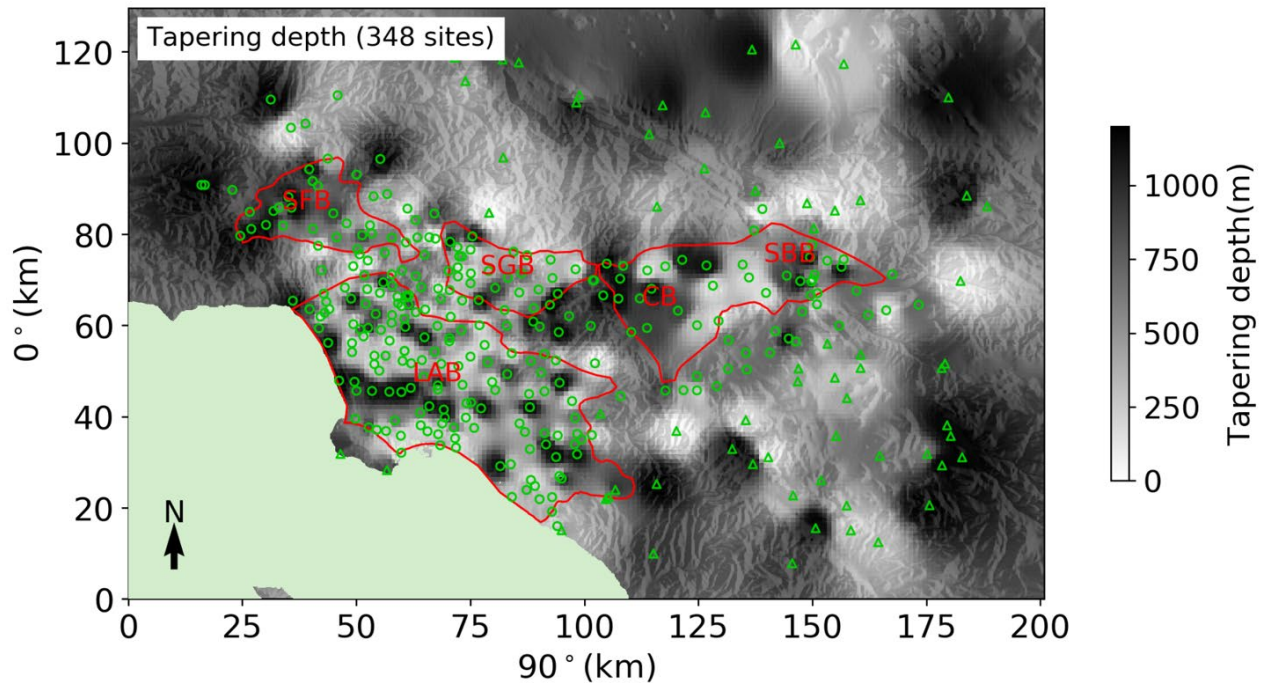
Figure 15. Average optimal tapering depth of the GTL, inferred from the maps of average 0.3-1.0 Hz FAS bias for the 7 events shown in Figure 1. The red lines depict approximate outlines of the San Fernando basin (SFB), Los Angeles basin (LAB), San Gabriel basin (SGB), Chino basin (CB), and San Bernardino basin (SBB).

Discussion and conclusions

We have shown that incorporating a new model of the San Gabriel, Chino and San Bernardino basins obtained from ambient noise tomography into the SCEC CVM-S decreases the FAS bias between 3D physics-based simulations and strong motion data by 38% for 7 M_w4.4-5.4 earthquakes at sites directly above the model. We then use the updated CVM to estimate the depth distribution of a near-surface GTL that minimizes the average 0.3-1.0 Hz FAS bias between the simulations and strong motion data in the greater Los Angeles area, CA. For sites with shear-wave velocity larger than 1,000 m in the CVM, the optimal tapering depth shows strong spatial variation. In general, the optimal tapering depths appear to increase from near 0 m at the edges of the sedimentary basins to values of 1,000 m or larger at distances of 10-50 km from the basins, in particular toward the northeast, east and southeast. Future simulations should verify that the estimated distribution of the GTL depths provides an improved fit between synthetics and data.

Hu et al. (2022) applied their GTL modifications only where existing Vs values were larger than the proposed taper, arguing that the SCEC CVM-S is already well-constrained by well data, V_{s30} values, etc, inside the basins. However, while this study focused on estimating the optimal GTL thickness at sites outside the sedimentary basins, our simulations also applied the GTL taper at sites inside the basins (see Figure 15). The basin sites generally favor small to no (additional) GTL in the SCEC CVM-S, while some sites show a rapid spatial variation between 0 m and 1,200 m, many aligned along pseudo-linear trends. We recommend further scrutiny on the Vs profiles at the basin sites in the SCEC CVM-S in order to improve the fit between seismic synthetics and data.

Acknowledgements

References

Ajala, R., and P. Persaud (2021). Effect of merging multiscale models on seismic wavefield predictions near the southern San Andreas Fault. *J. Geophys. Res.* **126**, no. 10, e2021JB021915, doi: 10.1029/2021JB021915.

Cui, Y., Poyraz, E., Olsen, K. B., Zhou, J., Withers, K., Callaghan, S., Larkin, J., Guest, C., Choi, D, Chourasia, A., et al. (2013). Physics-based seismic hazard analysis on petascale heterogeneous supercomputers. Page 70 of: Proceedings of SC13: International Conference for High Performance Computing, Networking, Storage and Analysis. ACM.

Boore, D. M., and W. B. Joyner (1997). Site amplifications for generic rock sites. *Bull. Seismol. Soc. Am.* **87**, no. 2, 327–341, doi: 10.1785/BSSA0870020327.

Brocher, T. M. (2005) Empirical Relations between Elastic Wave speeds and Density in the Earth's Crust. *Bull. Seismol. Soc. Am*. **95**, no. 6, 2081–2092, doi: 10.1785/0120050077.

Ely, G. P., Jordan, T., Small, P., and Maechling, P. J. (2010). A Vs30-derived near-surface seismic velocity model. AGU Fall Meet., San Francisco, California, 13–17 December, Abstract.

Hu, Z., K.B. Olsen, and S.M. Day (2022). Calibration of the Near-surface Seismic Structure in the SCEC Community Velocity Model Version 4. *Geophys. Jour. Int.* **230**, 2183-2198.

Konno, K., and T. Ohmachi (1998). Ground-motion characteristics estimated from spectral ratio between horizontal and vertical components of microtremor. *Bull. Seismol. Soc. Am.* **88**, no. 1, 228–241, doi: 10.1785/BSSA0880010228.

Li, Y., V. Villa, R.W. Clayton, and P. Persaud (2023). Shear wave velocities in the San Gabriel and San Bernardino Basins, California. *Jour. Geophys. Res., Solid Earth* **128(7)**.

Nie, S., Wang, Y., Olsen, K. B., and Day, S. M. (2017). Fourth Order Staggered Grid Finite Difference Seismic Wavefield Estimation Using a Discontinuous Mesh Interface (WEDMI). *Bull. Seism. Soc. Am.* **107(5)**, 2183-2193.

Olsen, K.B. (2000). Site Amplification in the Los Angeles Basin from 3D Modeling of Ground Motion. *Bull. Seis. Soc. Am.* **90**, S77-S94.

Olsen, K.B., Day, S.M., and C.R. Bradley (2003). Estimation of Q for long-period (>2 s) waves in the Los Angeles Basin. *Bull. Seis. Soc. Am.* **93**, 627-638.

O'Reilly, O., T.-Y. Yeh, K.B. Olsen, Z. Hu, A. Breuer, D. Roten, and C. Goulet (2022). A high-order finite difference method on staggered curvilinear grids for seismic wave propagation applications with topography. *Bull. Seis. Soc. Am.* **112 (1),** 3-22, https://doi.org/10.1785/0120210096.

Shao, G., C. Ji and E. Hauksson (2012). Rupture process and energy budget of the 29 July 2008 Mw 5.4 Chino Hills, California, earthquake, *J. geophys.,Res. Solid Earth,* **117**(B7), doi:10.1029/2011JB008856.

Small, P., D. Gill, P. Maechling, R. Taborda, S. Callaghan, T.H. Jordan, et al. (2017). The SCEC Unified Community Velocity Model Software Framework. *Seismol. Res. Lett.,* **88(6),** 1539-1552. https://doi.org/10.1785/0220170082

Thompson, E. M. (2018). An Updated Vs30 Map for California with Geologic and Topographic Constraints, US Geol. Surv. Data Release, doi: 10.5066/F7JQ108S.

COMPARISON OF GROUND MOTIONS FROM CSN INSTRUMENTS AND PROXIMATE SENSORS FROM OTHER NETWORKS

Jonathan P. Stewart[1], Shako Mohammad[1], Chukwuebuka C. Nweke[2], Rashid Shams[2], Tristan E. Buckreis[1], Monica D. Kohler[3], and Yousef Bozorgnia[1]

[1] UCLA Samueli Engineering
[2] USC Civil & Environmental Engineering
[3] California Institute of Technology

Abstract

The Community Seismic Network (CSN) is a low-cost, MEMS-sensor seismic network with smaller average station-to-station spacing than stations for other networks. We have downloaded and processed CSN data for 29 earthquakes with $M > 4$ from 2012 to 2023 using NGA procedures. Visual checks of data useability were applied to distinguish rejected records form records with clear seismic signals. We compare recordings from proximate (within 3 km) CSN and non-CSN (generally SCSN or CSMIP) stations with usable signals. Results show no systematic differences for peak acceleration and similar spectra when the CSN motions have large usable bandwidths.

Introduction

The Community Seismic Network (CSN) is a network currently with over 800 three-component seismic stations, mainly in southern California (Clayton et al. 2011, 2020; http://csn.caltech.edu/), which are operated as a collaborative research effort between Caltech and UCLA. The network is expected to grow to 1200 three-component stations by the end of 2023. In terms of its layout and configuration, CSN differs from other seismic networks in two principal respects. First, the sensors are spatially concentrated in certain parts of southern California, and as a consequence, as currently configured they are relatively ineffective for some classical applications like earthquake location or recording motions over a wide distance range, but they are effective at capturing ground motion characteristics over relatively short length scales. Second, the instruments have relatively high noise levels compared to broadband seismometers or modern accelerometers.

We have recently completed a project that evaluated the effective noise threshold of CSN data based on the currently available recordings, to validate the recordings against those from higher-resolution sensors, and to make available in a public database CSN data that is judged to be reliable along with its associated metadata. Results of this study are presented in a project report (Stewart et al. 2023). This paper presents a portion of the research results related to comparisons of CSN data to data from proximate sensors from alternate networks (mainly CSMIP and Southern California Seismic Network).

Following this introduction, we provide background information on the CSN, describe the data produced by the network, describe the data processing and assignment of classes that indicate record quality, and compare CSN data to data from other networks.

CSN Instruments and Housing

Over the duration of the current project, the Community Seismic Network (CSN) comprised 769 seismic station locations, most of which are in southern California (Clayton et al., 2020). In addition, there are 339 previously active but now decommissioned station locations, some of which produced data that is evaluated. Figure 1 shows the locations of CSN stations overlaid on a regional map that also shows stations from other regional networks (CSMIP, USGS, SCSN). As indicated in Figure 1, the locations of CSN stations include the San Fernando Valley, Pasadena, San Gabriel Valley, downtown Los Angeles, Hollywood, and South Los Angeles; many of these areas have high densities of population or industrial activity and hence are culturally noisy.
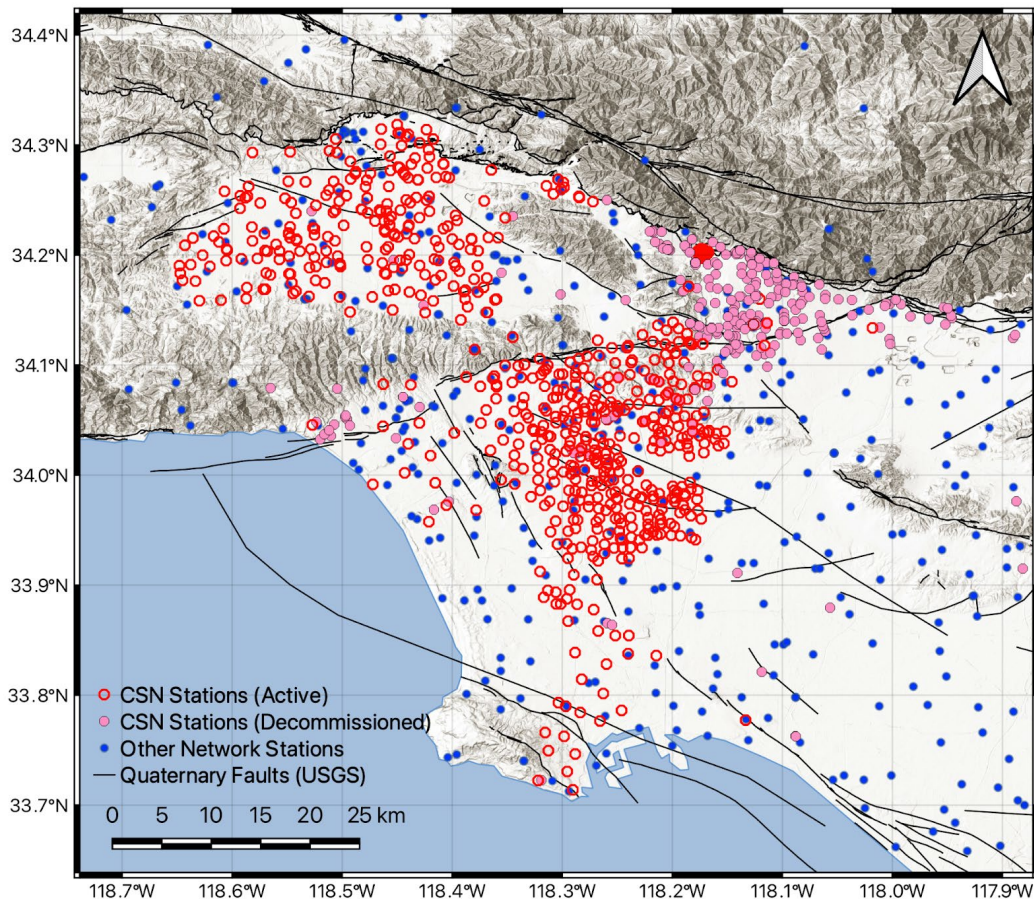
Figure 1. Map of southern California showing locations of ground motion stations considered in prior work (NGA-West2, Bozorgnia et al. 2014 & basin study, Nweke et al. 2022) (CSMIP, USGS, SCSN) and CSN stations (active and decommissioned) considered in this project.

CSN utilizes low-cost, three-component, MEMS accelerometers. The primary product of the network is measurements of shaking of the ground as well as upper floors in buildings, in the seconds during and following a major earthquake. Each sensor uses a small, dedicated ARM processor computer running Linux, and analyzes time series data in real time at 250 samples per second (sps), which is then downsampled to 50 sps. Innovations in cloud computing for data processing, coupled with sensor developments for the video-gaming and automotive air bag industries, have helped form the technological basis of this network. Prior to ~2014, most CSN stations consisted of plug-in sensors that were attached to community hosts' laptops and desktop computers; the hosts determined the deployment location and coupling. Data from these deployments went into the early earthquake database, but this deployment type no longer exists. After 2014, all CSN sensors are stand-alone devices deployed by a CSN field engineer who determines location and physical coupling with the floor.

Some CSN station locations have multiple instruments. This occurs because of multiple instruments (referred to here as a "station") within a structure at different heights, and in some cases, different locations in plan at a given height. The number of three-component instruments is 1868, which includes 1250 ground stations, 27 basement stations, and 463 stations on floors of buildings above the ground line. The instrumented buildings have between 1 and 3 triaxial sensors deployed per floor. The sensing hardware and parameters are the same as for the free-field. There are no sensors on lifelines infrastructure at the present time.

We focused on ground and basement stations and do not consider above-ground stations. Each of the ground-level and basement stations has been assigned an instrument housing code using guidelines from COSMOS (COSMOS 2001). This information is provided as metadata accompanying the CSN sites in the ground motion database (Buckreis et al. 2023). The applicable codes that were applied to CSN stations are as follows:

1. "04" - ground-floor in a 1-2 story building without a basement (1250 CSN stations)
2. "05" - ground-floor in a larger structure (118 CSN stations)
3. "09" - basement or underground in a large vault (27 CSN stations)
4. "10" - upper levels of a structure (463 CSN stations)

Stations in group 04 can be considered "free-field." Stations in 05 and 09 might be approximated as free-field depending on the depth of embedment (for 09) and plan size of the structure (for 05). The difference between the 769 figure mentioned at the start of this section and the sum of 04, 05, and 09 is caused by the occurrence of multiple stations at a given site at the ground level or basement level.

Database

Events Considered

Figure 2 shows the locations of 29 events considered in this study. We include all events recorded by the network with $M > 4$. Per NGA protocols (e.g., Contreras et al. 2022), seismic moment is taken from the global centroid moment tensor catalog (Ekström et al. 2012;

https://www.globalcmt.org/) as are other moment tensor attributes with the exception of hypocenter location, which is taken from USGS (https://www.usgs.gov/programs/earthquake-hazards/earthquakes).
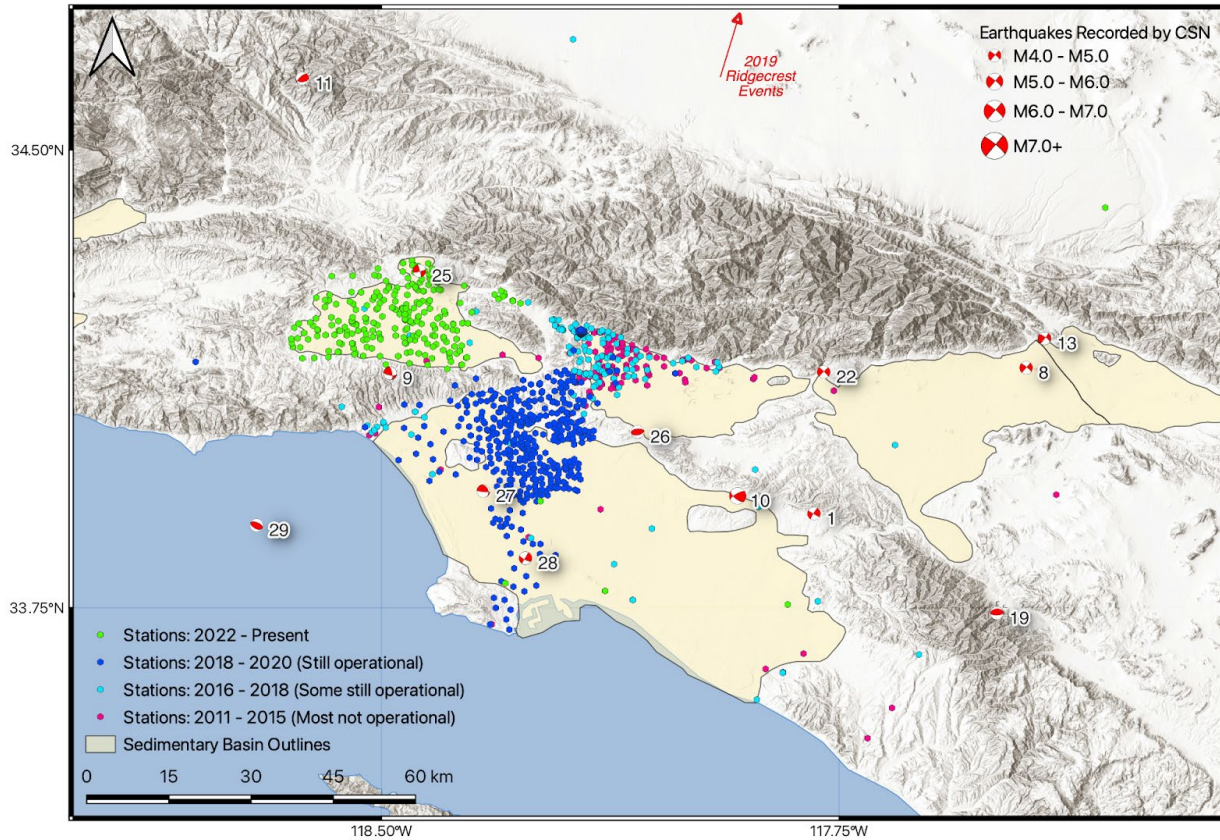

Figure 2. Map of CSN stations and the events they recorded.

CSN Data Processing

The Next Generation Attenuation (NGA; e.g., Bozorgnia et al 2014) program has developed standard steps that are used to process earthquake ground motions. The aim of the steps is to minimize the effects of noise on recorded ground motions, while optimizing the dynamic range for which a given recording can be considered to accurately represent the ground shaking at the site. The most recent procedures are described by Goulet et al. (2021) and Kishida et al. (2020), although the main elements of the procedure were presented earlier by Boore (2005), Boore and Bommer (2005), and Douglas and Boore (2011). The steps included the following, and are illustrated by Stewart et al. (2023) for their application to the CSN data:

1. Screening to identify noise-dominated records or records with spurious features
2. Identification of noise and signal windows
3. Compute Fourier Amplitude Spectra (FAS) of both windows and normalization of the FAS to account for potentially different window durations.

4. Apply high- and low-pass filters to minimize effects of noise at low and high frequencies, respectively.
5. Baseline correction

These procedures were applied using a modified version of the gmprocess code (Hearne et al., 2019). As described in Ramos-Sepulveda et al. (2023), the modifications improve the high-pass corner frequency selection to minimize displacement wobble and facilitate human review and modification of corner frequencies.

Some of the events shown in Figure 2 were not present in the working version of the relational ground motion database being used in the NGA-West3 project (Buckreis et al. 2023). For those events, non-CSN data was also processed using similar procedures so that more complete datasets for each event are available. All of the data is incorporated into the current working version of the database, which is publicly available.

Data Classification

In our evaluations of the CSN data, we observed three general categories of records. The "best" records (BroadBand Records; BBR) clearly reflect earthquake shaking, having waveforms where the different wave arrivals are evident and modest effects of noise. Records deemed unusable (REJected records; REJ) appear to be noise dominated, generally based on visual inspection of time series, but sometimes also from similar levels of signal and noise FAS. The intermediate case (Narrow-Band Records; NBR) consists of records that have the visual appearance of earthquakes, but the signal is of modest strength in comparison to noise and the record bandwidths are relatively limited.

Figure 3 shows data distributions in magnitude-distance space for BBR (green), NBR (yellow), and REJ (red) records. In the upper-left portion of the plot (large magnitude or close distances for $\mathbf{M} < 5$ events), most records are BBR, whereas the lower-right portions ($\mathbf{M} < 5$ event and distances > 50-100 km) are REJ. Clearly the level of ground shaking strongly affects the classifications. This is also reflected in summary statistics for the data set. Among events since 2018, large-magnitude events and events generally closer than 70-80 km from the network (Malibu, Carson, Lennox, El Monte, Pacoima, Searles Valley, Ridgecrest, La Verne) have the following aggregate component record classifications:

*   Usable records (BBR and NBR): 5470 (56.7%) (1122 BBR, 4358 NBR)
*   Rejected records: 4176 (43.2%)

The database as a whole, which includes many events with small magnitude and large distances, breaks down as

*   Usable records (BBR and NBR): 9286 (46.4%) (1187 BBR, 8009 NBR)
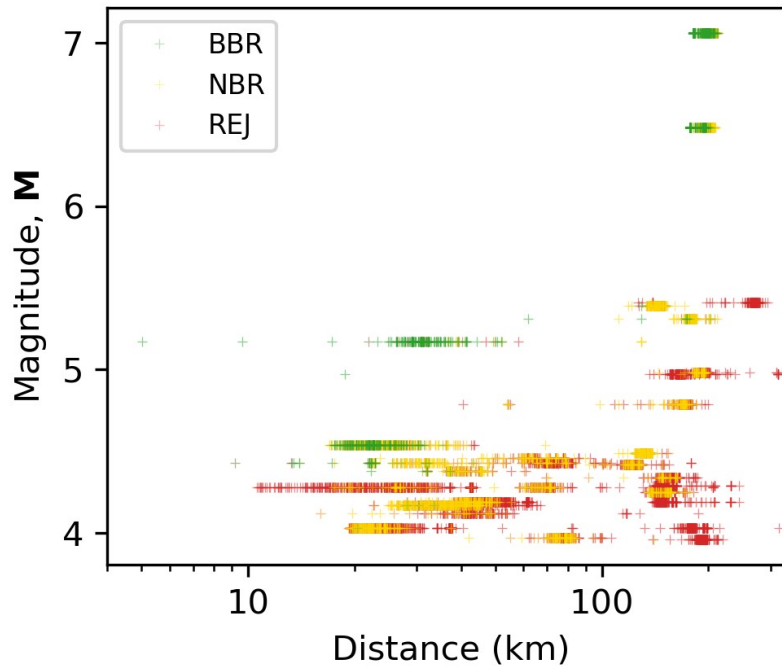*   Rejected records: 10,612 (53.6%)

Figure 3. Record classification as function of distance and magnitude.

Data Comparisons

An important step in the evaluation of the usability of ground motions recorded by CSN stations is to compare with ground motions recorded by non-CSN/traditional network sensors that have been used in previous studies (i.e., NGA projects). Such comparisons are most robust when sensors from both networks share the same location and both record a given event. Three such co-located sensor pairs exist in the network. The analysis of these sensors (Stewart et al. 2023) is inconclusive due to the small size of the data set and some differences in the sizes of structures housing the different instruments. Here, we instead focus on proximate sensors, which meet two criteria: (1) the stations are separated by ≤ 3 km and (2) the stations have the same surface geology, based on the statewide map by Wills et al. (2015). Station pairs that meet these criteria are mapped in Figure 4 (arrows are drawn between paired stations).
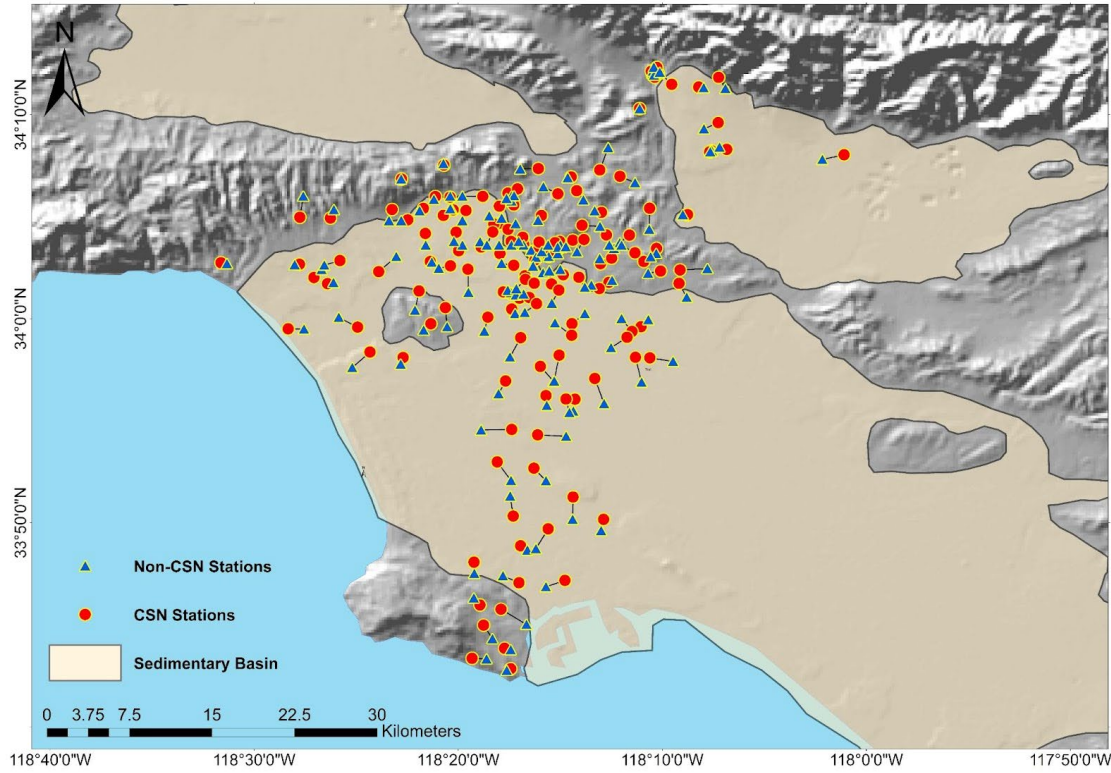
Figure 4. Map showing proximate CSN and non-CSN stations (160 pairs), defined by separation distances ≤ 3 km and matching surface geologies as provided by Wills et al. (2015).

For each station pair, a differential ground motion IM is computed as:

$$\delta(lnIM) = ln(IM_{csn}) - ln(IM_{net}) \tag{1}$$

where the 'csn' subscript indicates the IM is from the CSN station and the 'net' subscript indicates the IM is from the non-CSN station. Both IMs are taken from individual as-recorded components of ground motion (generally north-south and east-west). The average value of $\delta(lnIM)$ is denoted μ_δ.

Figure 5 plots $\delta(lnIM)$ vs separation distance for cases in which the CSN records are BBR and the IM is PGA. The mean difference in this case is μ_δ = -0.017 with a standard error of the mean of 0.071. These results show that the CSN PGAs are on average slightly smaller than the non-CSN PGAs, but that the differences are small and within the margin of error. Figure 6 shows the variation of $\delta(lnIM)$ with period for Sa over the period range of 0.01 to 10 sec. Data are only considered in the calculation of the binned means when both the CSN and non-CSN Sa values are within their usable ranges given the data filtering (i.e., the oscillator period T < 0.8/f_{cHP} for both instruments). The results in Figure 6 show a negative bias (CSN lower) for periods near 1.0 sec (~0.6 < T < 2.0 sec) and for T > ~5 sec, but otherwise the two sets of IMs essentially match. The bias near 1.0 sec is about 10-15% (-0.1 to -0.15 ln units).
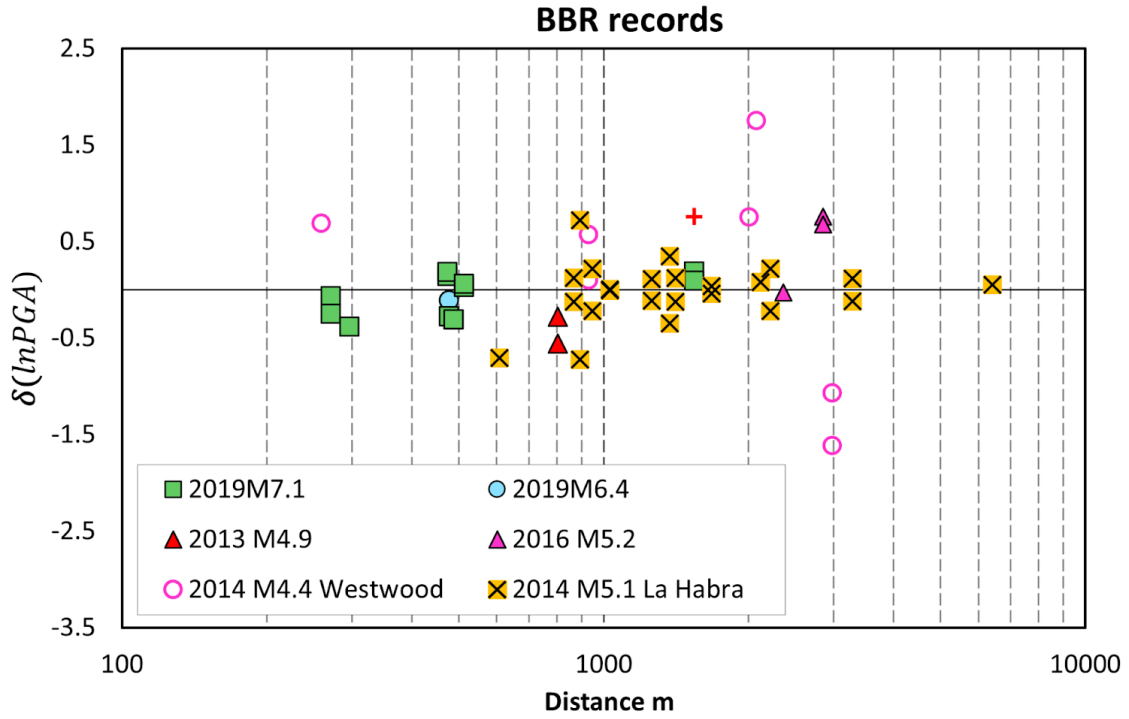
Figure 5. Variation of differential PGA with station separation distance for BBR CSN recordings. The mean and standard deviation of the data are μ_δ = -0.017± 0.071
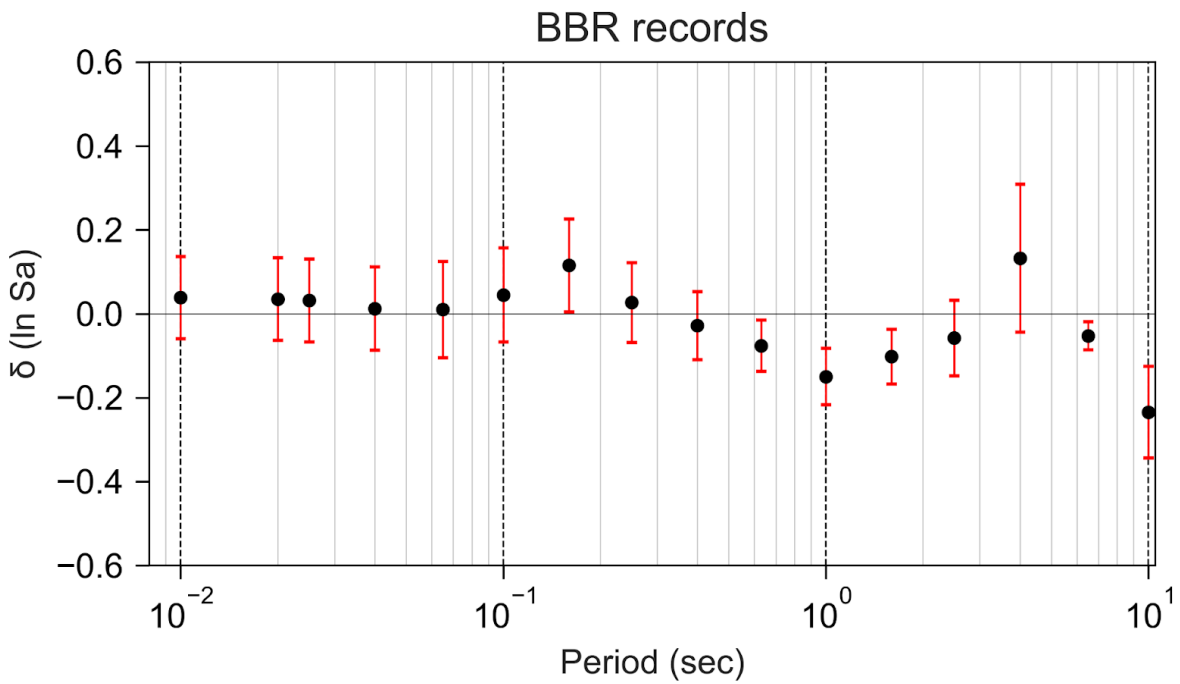

Figure 6. Variation of mean differential Sa with period for BBR CSN recordings

Figure 7 plots $\delta(lnIM)$ vs separation distance for cases in which the CSN records are NBR and the IM is PGA. The mean difference in this case is μ_δ = -0.023 with a standard error of the mean of 0.056. These results show that the CSN PGAs are on average smaller than the non-CSN PGAs, but as with BBR data, the differences are small enough that the bias can be considered to be statistically insignificant. Figure 8 shows the variation of $\delta(lnIM)$ with period for Sa over the period range of 0.01 to 10 sec. The results in Figure 8 show a negative bias (CSN lower) over multiple period intervals including 0.05-0.1 sec, 0.4-1.0 sec, and > 3 sec. Within these period intervals, the levels of bias are small (~ -0.1 ln units) but are repeatable and statistically significant.
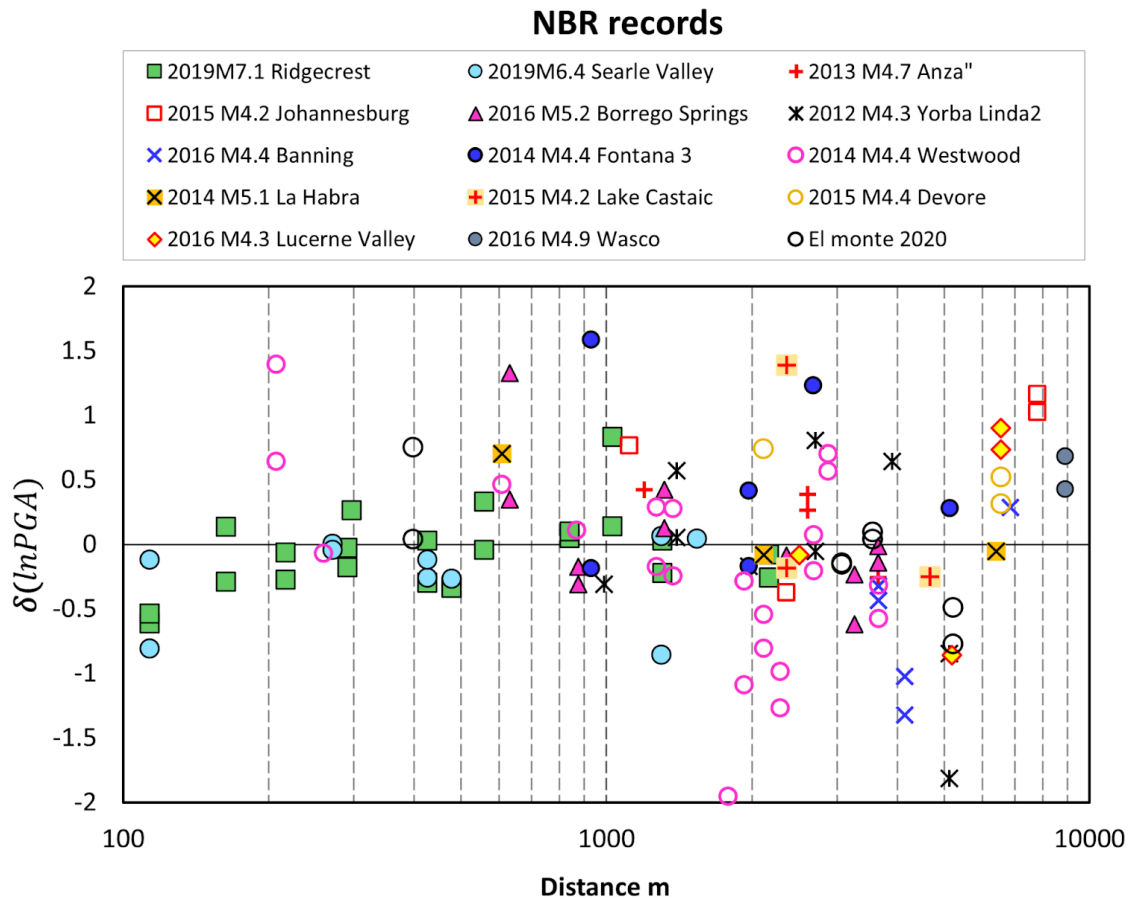

Figure 7. Variation of differential PGA with station separation distance for NBR CSN recordings. The mean and standard deviation of the data are μ_δ = -0.023± 0.056
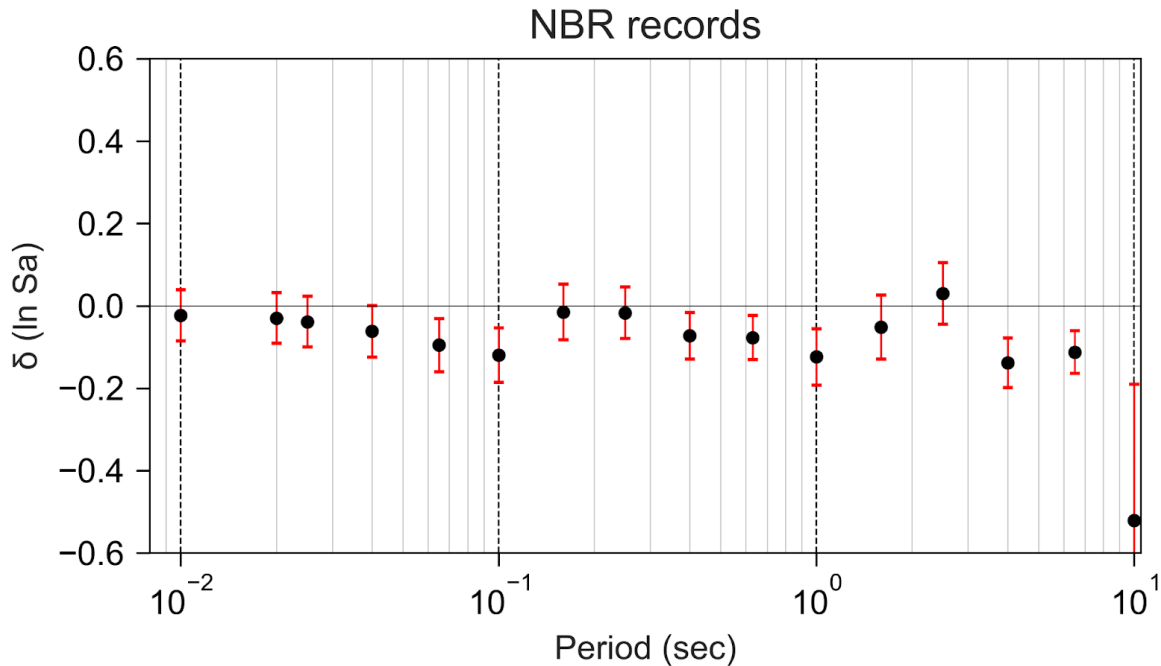
Figure 8. Variation of mean differential Sa with period for NBR CSN recordings.

The results presented above show that BBR CSN and non-CSN records are similar within the typical usable period range of PGA to ~5 sec, with the exception of low CSN ground motions near 1.0 sec. The CSN NBR records are also unbiased for PGA, but these records have lower ground motions than the non-CSN records over a range of periods, which is expected because by definition these records have a relatively limited frequency range and hence are missing significant portions of the seismic signal at low and high frequencies. As a result, we suggest that the criteria used to define BBR recordings be used to identify usable CSN data for ground motion applications.

Conclusions

This broader study from which the Stewart et al. (2023) report was produced has undertaken a series of tasks that collectively aim to provide insight into the performance of CSN ground-level sensors during southern California earthquakes, provide processed data in an accessible form for users, and provide recommendations on the range of conditions for which the data can be used with confidence in ground motion modeling projects.

CSN data from 29 earthquakes was uniformly processed using NGA-type procedures. For events where data from other networks was already available, the CSN data has been added to a national database for ground motion research applications (Buckreis et al. 2023) to supplement the previously available data. For events not previously in the database, CSN and non-CSN data

has been processed and added to the database. Relevant site and event metadata has been compiled and added so that this data is available for public use.

Among the events considered, approximately 50% of the recordings were judged to be not usable because they are noise-dominated based on visual inspection or have unusual features. These are referred to as REJ records in this report. However, this rate is potentially misleading as an indicator of network performance, because 27 of the 29 events are small magnitude (< 5.5) and often occurred at considerable distances from the network. Two large events (2019 Searles Valley and 2019 Ridgecrest) were successfully recorded by over 95% of sensor horizontal components, despite being located at distances > 150 km. This rate of data recovery is considered more representative of the performance that can be expected in future impactful earthquakes in the greater Los Angeles area.

Among the remaining (non-REJ) recordings, we distinguished records with relatively broad bandwidth (usable Fourier frequency range of at least 0.5 - 10 Hz) (denoted BBR) from those with relatively limited bandwidth (narrower than that for BBR at one or both ends of the frequency range; denoted NBR). Comparisons of BBR and NBR signals with signals from non-CSN proximate sensors (separation distance < 3 km and same geology) shows that PGA levels are not statistically distinguishable. Spectral accelerations from BBR CSN data appear to be unbiased over the oscillator period range of 0.01 to 5 sec based on these comparisons with the exception of lower CSN motions near 1.0 sec, whereas NBR CSN data have lower spectral accelerations for multiple period intervals < 5 sec (amount of the bias is generally < 10-15%). This is not surprising given the limited bandwidth of NBR signals.

These results show that CSN data is useful for research and engineering applications, but its range of applicability is more limited than data from more sensitive instruments. Within its application range, the CSN data have advantageous features, including relatively small between-sensor spacings that facilitate site response or ground motion variability studies at short length scales, as well as its continuous recording of ground motions. We strongly encourage continued operation and explanation of the CSN network to facilitate these and other research applications.

Acknowledgments

References

Boore DM, 2005. On pads and filters: processing strong-motion data, *Bull. Seism. Soc. Am.*, 95, 745-750.

Boore DM and Bommer JJ, 2005. Processing of strong-motion accelerograms: Needs, options and consequences, *Soil Dynamics & Earthquake Engineering*, 25, 93-115

Bozorgnia Y, Abrahamson NA, Al Atik L, Ancheta TD, Atkinson GM, Baker JW, Baltay A, Boore DM, Campbell KW, Chiou BS-J, Darragh RB, Day S, Donahue JL, Graves RW, Gregor N, Hanks T, Idriss IM, Kamai R, Kishida T, Kottke AR, Mahin SA, Rezaeian S, Rowshandel B, Seyhan E, Shahi S, Shantz T, Silva WJ, Spudich P, Stewart JP, Watson-Lamprey J, Wooddell KE and Youngs RR. 2014. NGA-West2 Research Project. *Earthquake Spectra* 30: 973–987.

Buckreis, TE, Nweke CC, Wang P, Brandenberg SJ, Mazzoni S, Stewart JP, 2023. Relational database for California strong ground motions, Geo-Congress 2023: Geotechnical Data Analysis and Computation, Los Angeles, CA, March 2023, *Geotechnical Special Publication No. 342*, EM Rathje, B Montoya, and MH Wayne (Eds.), 461-470, ASCE Geo-Institute

Clayton R, Heaton T, Chandy M, Krause A, Kohler M, Bunn J, Guy R, Olson M, Faulkner M, Cheng MH, Strand L, Chandy R, Obenshain D, Liu A, and Aivazis M, 2011. Community Seismic Network, *Annals of Geophysics*, 54 (6), doi: 10.4401/ag-5269.

Clayton R, Kohler M, Guy R, Bunn J, Heaton T, and Chandy M, 2020. CSN/LAUSD network: A dense accelerometer network in Los Angeles schools, *Seis. Res. Lett.*, 91(2A), 622-630, doi:10.1785/0220190200.

Contreras V, Stewart JP, Kishida T, Darragh RB, Chiou BSJ, Mazzoni S, Youngs RR, Kuehn NM, Ahdi SK, Wooddell K, Boroschek R, Rojas F, Ordenes J, 2022. NGA-Sub source and path database, *Earthquake Spectra*, 38(2), 799-840.

Consortium of Organizations for Strong-Motion Observation Systems (COSMOS), 2001 COSMOS strong motion data format. https://www.strongmotioncenter.org/vdc/cosmos_format_1_20.pdf (last accessed 9/15/2023).

Douglas J and Boore DM, 2011. High-frequency filtering of strong-motion records, *Bull. Eqk. Eng.*, 9, 395–409.

Ekström G, Nettles M, Dziewonski AM, 2012. The global CMT project 2004–2010: Centroid-moment tensors for 13,017 earthquakes. *Physics the Earth and Planetary Interiors* 200–201: 1–9.

Goulet, CA, Kishida T, Ancheta TD, Cramer CH, Darragh RB, Silva WJ, Hashash YMA, Harmon J, Parker GA, Stewart JP, Youngs RR, 2021. PEER NGA-East database, *Earthquake Spectra*, 37(S1), 1331-1353

Hearne M, Thompson EM, Schovanec H, Rekoske J, Aagaard BT and Worden CB, 2019. USGS automated ground-motion processing software, USGS Software Release, doi:10.5066/P9ANQXN3.

Kishida T, Darragh RB, Chiou BSJ, Bozorgnia Y, Mazzoni S, Contreras V, Boroschek R, Rojas F, Stewart JP, 2020. *Chapter 3: Ground motions and intensity measures (Data resources for NGA-subduction project)* (ed JP Stewart). PEER report 2020/02. Berkeley, CA: Pacific Earthquake Engineering Research Center, UC Berkeley.

Nweke CC, Stewart JP, Wang P, Brandenberg SJ, 2022. Site response of sedimentary basins and other geomorphic provinces in southern California, *Earthquake Spectra*, 38(4), 2341-2370.

Ramos-Sepulveda ME, Parker GA, Thompson EM, Brandenberg SJ, Li M, Ilhan O, Hashash YMA, Rathje EM and Stewart JP, 2023. High-pass corner frequency selection for implementation in the USGS

automated ground-motion processing tool, Geo-Congress 2023: Geotechnical Data Analysis and Computation, Los Angeles, CA, March 2023, Geotechnical Special Publication No. 342, EM Rathje, B Montoya, and MH Wayne (Eds.), 327-335, ASCE Geo-Institute

Stewart, JP, Mohammad S, Nweke CC, Shams R, Buckreis TE, Kohler MD, Bozorgnia Y (2023). Usability of ground motions recorded by Community Seismic Network, Garrick Institute for Risk Sciences, UCLA Samueli Engineering.

Wills CJ, Gutierrez CI, Perez FG, Branum DM, 2015. A next generation VS30 map for California based on geology and topography, *Bulletin of the Seismological Society of America* 105(6): 3083–3091.

FEBRUARY 2023 EARTHQUAKES IN TURKEY AND SYRIA: OBSERVATIONS FROM THE FIELD AND THE STRUCTURAL ENGINEERING OFFICE

Ayse Hortacsu

Applied Technology Council

Abstract

The Learning From Earthquakes (LFE) program of the Earthquake Engineering Research Institute (EERI) deployed several teams to conduct reconnaissance activities in Turkey following the February 6, 2023 earthquakes. The findings from the teams, along with the observations from the GEER Association field teams are summarized in the report available here: https://learningfromearthquakes.org/2023-02-06-nurdagi-turkey/images/2023_02_06_nurdagi_turkey/GEER_2023_Turkey_Earthquake_FullReport_ReducedSize.pdf .

This presentation brings forward highlights from the field observations with a focus on typical damage to reinforced concrete frame structures, and the impact of this damage to property and to the community functions. The presentation also reports on the post-earthquake functionality of two hospitals serving the same community, along with data collected from additional healthcare facilities in the region. Although the code requirements pertaining to structural engineering in the last two decades are on par with the requirements in the U.S., the observations from the field indicate that lack of code enforcement during the design and construction phase may have an impact on the performance of the buildings.

2023 TÜRKIYE EARTHQUAKE SEQUENCE: STRONG MOTION DATA

Tristan E. Buckreis

Department of Civil and Environmental Engineering, University of California, Los Angeles

Abstract

The 2023 Türkiye earthquake sequence includes the February 6 **M**7.8 mainshock followed approximately nine hours later by a **M**7.7 aftershock, and many smaller aftershocks including **M**6.8 and **M**6.3 events on February 6 and 20, respectively. These events occurred in a region near the plate boundary on the East Anatolian Fault, in the proximity of which numerous strong motion recording stations had been installed north of the Türkiye-Syria border. Within hours of these significant events, strong motion data became available through the Earthquake Data Center System of Türkiye (TDVMS) and the Incorporated Research Institutions for Seismology (IRIS) from over 700 seismic stations operating in the region. Early releases of some data through TDVMS were found to contain baseline-correction and instrument metadata errors, which have been corrected over time. Additionally, records at a few number of stations which had be identified to terminate prematurely (i.e., the record ends while the site is experiencing significant shaking), have been properly windowed in subsequent releases.

Raw time-series have been screened manually to remove noise-dominated and spurious records, and the remaining records were processed using standard procedures developed during Next Generation Attenuation (NGA) projects. A total of 310, 351, 291, and 229 usable three-component recordings were processed from the **M**7.8, **M**7.7, **M**6.8, and **M**6.3 events, respectively, with maximum peak ground accelerations at several stations exceeding 1.0 g. Source, path, and site metadata were compiled according to uniform protocols, which benefited greatly from extensive site characterization performed at seismic stations by the Disaster and Emergency Management Authority (AFAD). The strong motion data and associated metadata are publicly available at https://doi.org/10.17603/ds2-t115-bk16[1], and will be incorporated into the NGA-West3 database.

Comparisons to ground motion models (GMMs) for active tectonic regions demonstrate the existence of complex path effects that result in relatively poor fits between the GMMs and observed data at large distances (R_{JB} > 200 km). Residual maps produced from these analyses demonstrate that ground motions generally over-predicted on the Anatolian block and under-predicted on the Arabian block. The repercussions of these events will have a lasting effect on the region, and their scientific and engineering impacts will prove to be influential for future ground motion related studies and efforts.

[1]Buckreis, T., B. Güryuva, A. İçen, O. Okcu, A. Altindal, M. Aydin, R. Pretell, A. Sandikkaya, Ö. Kale, A. Askan, S. Brandenberg, T. Kishida, S. Akkar, Y. Bozorgnia, and J. Stewart (2023) Ground Motion Data from the 2023 Türkiye-Syria Earthquake Sequence. DesignSafe-CI. https://doi.org/10.17603/ds2-t115-bk16